POLITECNICO
MILANO 1863

SCUOLA DI INGEGNERIA INDUSTRIALE
E DELL'INFORMAZIONE

EXECUTIVE SUMMARY OF THE THESIS

Analysis of Multi-Static Spaceborne SAR Formations for High-Resolution Imaging at P-Band

TESI MAGISTRALE IN SPACE ENGINEERING – INGEGNERIA SPAZIALE

AUTHOR: MARTINA STASI

ADVISOR: STEFANO TEBALDINI

ACADEMIC YEAR: 2020-2021

Abstract

The aim of the submitted thesis is to present the developed theoretical and computer tools needed to perform the preliminary design of a feasible space mission for a multi-static Synthetic Aperture RADAR (SAR) campaign working at P-Band. The ultimate goal of the design is to use the data coming from different satellites to overcome the fundamental resolution limit of P-Band spaceborne RADARs, which results from the $6\,MHz$ bandwidth restriction imposed by the International Telecommunication Union (ITU). Indeed, by implementing a multi-static solution, leveraging the principle of Multi-static Wavenumber Tessellation (MWT), it is possible to remarkably enhance the SAR systems imaging capabilities without increasing the transmitted bandwidth. As result, two promising and feasible multi-static SAR fleet solutions are proposed, featuring a range resolution three times finer with respect to a conventional monostatic P-Band SAR and a Noise Equivalent Sigma Zero of around $-30\,dB$ within a ground swath of more than $50\,km$.

1. Introduction

Today the climate change is a very pressing problem to be tackled. The main cause of this issue can be found in the build-up of carbon dioxide in the atmosphere that acts like a heat sink, producing the well-known greenhouse effect. Hence the necessity of monitoring with good accuracy the global carbon cycle and reducing the uncertainties in the calculations of carbon stocks and fluxes, associated with the terrestrial biosphere, appears to be very urgent. Indeed, the atmosphere-terrestrial biosphere carbon flux is not even explicitly measured at present, but it is obtained indirectly by subtracting from the atmospheric carbon increase the contributions of fossil fuel combustion and those of the ocean, leading to an extremely high uncertainty level [1]. This is due to the fact that, even if one central parameter in the terrestrial carbon budget is the forest biomass, in most parts of the world it is very poorly quantified owing to the difficulties in taking measurements from the ground and to the lack in consistency when aggregating measurements across scales.
Nevertheless, exploiting the unique sensitivity of the P-band, the SAR systems could be able to

deliver completely new information on the world's forests. In particular, they would be able to measure forest above-ground biomass, trees and vegetation height and disturbance patterns across the entire biomass range, with frequency and accuracy compatible with the needs of international reporting on carbon stocks and terrestrial carbon models [2] [3].

To give a concrete help in this challenging climate change scenario, in 2013 ESA selected the Earth Explorer Biomass mission to study with a P-Band SAR the status and the dynamics of forests, as represented by the distribution of biomass and how it is changing [3].

Moreover, the long P-Band wavelength is also a precious resource to study the near-subsurface region not only of the Earth, but also of planetary bodies including the Moon, Mars, Mercury, Venus, comets, icy moons and asteroids, which is an investigation that nowadays is of high interest for future human or robotic explorers. For this reason, NASA JPL is carrying on the P-Band Space Exploration Synthetic Aperture RADAR (SESAR) project, illustrated in [4].

Nonetheless, despite the clear benefits, the P-Band SARs are not exploited yet (Biomass is set to be launched in 2023) due to their great drawback, namely the very coarse range resolution (ρ_r) of $24.98\,m$, that also affects Biomass and SESAR. Therefore, in this work, it is proposed a multi-static solution to greatly enhance the SAR systems imaging capabilities without increasing the transmitted bandwidth, which is constrained by the ITU regulations.

2. Multi-static Wavenumber Tessellation

Consider a generic (i.e.: RADAR, Sonar, Seismic) experiment, where a point-like object (or target, in RADAR jargon) at coordinates $\boldsymbol{r}_t = [x_t \;\; y_t \;\; z_t]^T$ is illuminated by a monochromatic wave emitted by a transmitter and then the reflected wave is recorded by a receiver. Supposing that this receiver is far from the object (so that the scattered wave from the target can be treated as a plane wave at the receiving point) and assuming weak scattering (i.e., Born approximation), it is possible to derive the Fundamental Equation of Diffraction Tomography (FEDT) following the procedure presented in [5].

Thus, the FEDT, regulating the relation between the scattered field and the object spectrum, can be written as:

$$S_{planar}(\hat{\boldsymbol{\imath}}, \hat{\boldsymbol{r}}) = -k^2 \mathcal{O}\big(k(\hat{\boldsymbol{r}} - \hat{\boldsymbol{\imath}})\big) \tag{1}$$

where S_{planar} is the scattered field, $\mathcal{O}$ indicates the 3D Fourier transform and it is possible to define the global wavenumber vector as:

$$\boldsymbol{K} = k(\hat{\boldsymbol{r}} - \hat{\boldsymbol{\imath}}) \tag{2}$$

where k in the is the wavenumber defined as:

$$k = 2\pi \frac{f}{c_0} \tag{3}$$

in which f is the frequency and c_0 is the supposed constant and homogeneous propagation velocity of the hosting medium (for spaceborne SARs is the speed of light in vacuum c). On the other hand, $\hat{\boldsymbol{\imath}}$ and $\hat{\boldsymbol{r}}$ are the unitary vector denoting the direction of propagation of the incident wave and the direction of propagation of the scattered wave, respectively, with reference to the bistatic SAR geometry (transmitter TX and receiver RX are separate) presented in Figure 1.

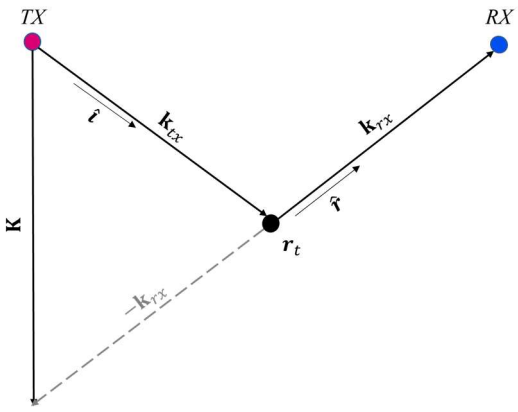

Figure 1: Wavenumber vectors for a point target in a bistatic SAR scenario

By referring to the geometry presented in Figure 1 it is possible to define:

$$\mathbf{k}_{tx} = \frac{2\pi}{\lambda}\hat{\boldsymbol{\imath}} = k\hat{\boldsymbol{\imath}} \tag{4}$$

$$\mathbf{k}_{rx} = \frac{2\pi}{\lambda}\hat{\boldsymbol{r}} = k\hat{\boldsymbol{r}} \tag{5}$$

where the vectors $\mathbf{k}_{tx}$ and $\mathbf{k}_{rx}$ represent the wavenumber vectors of plane waves traveling from the transmitter to the target at $\boldsymbol{r}_t$ and from the

target to the receiving satellite, respectively, therefore the global wavenumber vector $\boldsymbol{K}$ can be expressed also as $\boldsymbol{K} = \mathbf{k}_{tx} - \mathbf{k}_{rx}$. At this point, $\boldsymbol{K}$ can be decomposed in the fundamental SAR directions, namely azimuth x, ground and slant range (y and r, respectively) and elevation z, as presented in Figure 2.

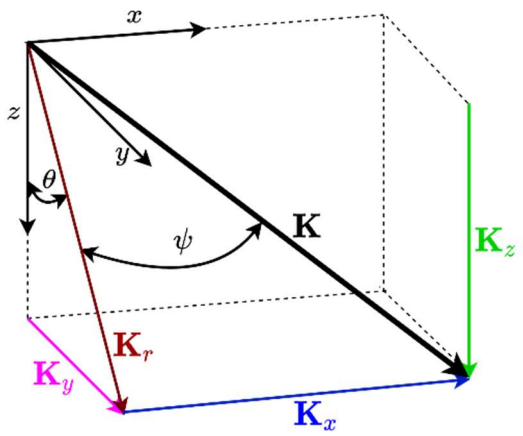

Figure 2: Decomposition of the global wavenumber vector

By referring to the geometry presented in Figure 2 (in which ψ and θ are the azimuth and elevation angle, respectively), the K_r and K_x components expressed in $[rad/m]$, for the bistatic SAR scenario, are defined according to the following mathematical expressions:

$$K_r = \frac{2\pi}{\lambda}[\cos(\psi_{tx}) + \cos(\psi_{rx})] \quad (6)$$

$$K_x = \frac{2\pi}{\lambda}[\sin(\psi_{tx}) + \sin(\psi_{rx})] \quad (7)$$

where λ is the wavelength. From these last equations, it is evident that with the basic knowledge of the target position in terms of ψ, it is possible to know exactly which wavenumber region will covered. Indeed, the wavenumber coverage performance of a SAR system, can be illustrated trough the wavenumber coverage diagrams, representing the vectorial components of **K** observed by the remote sensing system being evaluated.
For instance, in Figure 3, it is presented the wavenumber coverage map, computed for a P-Band bistatic SAR, at frequency of 435 MHz, in the case of a point target.

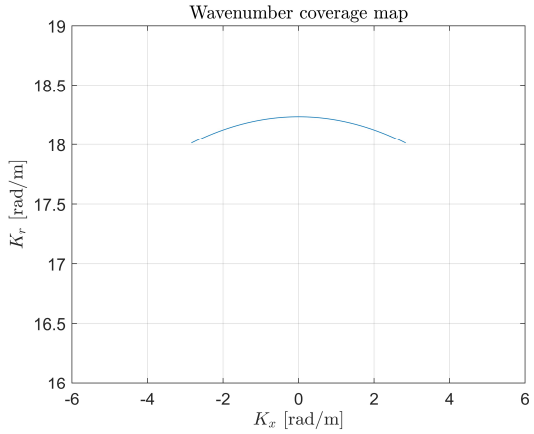

Figure 3: Wavenumber coverage map with one bistatic couple and no bandwidth

However, systems like the one presented in this last image are unfeasible since they do not provide any range resolution due to the fact that ρ_r is directly related to the employed bandwidth B ($\rho_r = \frac{c}{2B}$). Thus, an addition to Equations (6) and (7) has to be done, leading to:

$$K_r = \frac{2\pi}{c}\left(f_0 \pm \frac{B}{2}\right)[\cos(\psi_{tx}) + \cos(\psi_{rx})] \quad (8)$$

$$K_x = \frac{2\pi}{c}\left(f_0 \pm \frac{B}{2}\right)[\sin(\psi_{tx}) + \sin(\psi_{rx})] \quad (9)$$

where f_0 indicates the carrier frequency employed by the SAR systems. Considering the same situation presented in Figure 3 but adding the typical P-Band bandwidth of 6 MHz, leads to the coverage diagram reported in Figure 4.

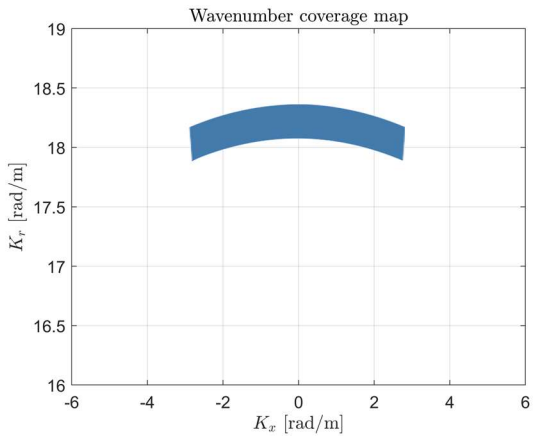

Figure 4: Wavenumber coverage map with B

The line presented in Figure 3 has now become a "tile", thanks to the addition of bandwidth term which only increments the range wavenumber coverage. Therefore, it is clear that the latter is determined by the bandwidth amplitude, thus it is

also true that, by finding a solution to obtain the greatest wavenumber coverage in the range direction, it is possible to virtually enlarge the system bandwidth.
This equivalent larger bandwidth, that is extremely interesting in the case of P-Band SARs, can be obtained by exploiting the Multi-static Wavenumber Tessellation principle [6]. Indeed, the latter is aimed to extend the range wavenumber coverage by means of multiple bistatic couples. Therefore, the multi-static nature of this project, denoting systems which use multiple bistatic couples to perform observations of the same target. Indeed, each acquisition gives rise to a different tile, and it is possible to regulate the tiles' positioning in the coverage map by properly setting the relative positions of transmitters and receivers along the orbit. If these separations are properly chosen, the tiles appear to be perfectly adjacent one to the other, as it is shown in Figure 5 in the case of 3 bistatic couples.

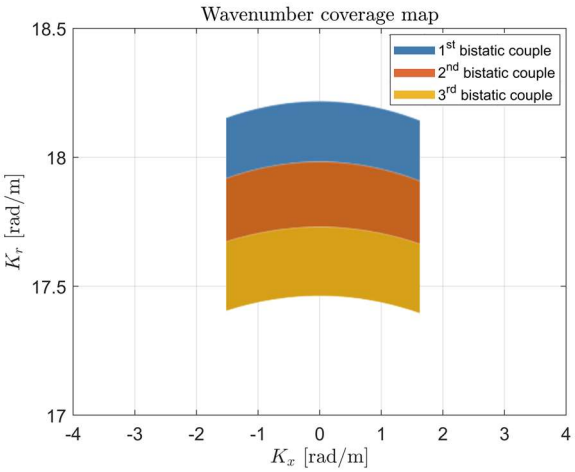

Figure 5: Wavenumber coverage map with 3 bistatic couples

It is better to point out that this last plot results from simulating a SAR fleet in which one receiver, positioned as head of the formation, is followed by 3 transmitters (properly spaced), which is exactly the situation of the two fleet designs illustrated in Section 3.
The fundamental result of a properly performed "tessellation", like the one illustrated in Figure 5, is that this extended coverage in the K_r direction results in a phenomenon which can be defined as equivalent bandwidth extension of the SAR system. The latter, is obtained by enriching the observed wavenumbers though a proper combination of the observations coming from different bistatic couples, thus from different ψ angles.
This can represent the solution to the main problem of P-Band missions, in fact, by exploiting the MWT virtual bandwidth extension it is possible to achieve a significant range resolution enhancement, despite the imposed real bandwidth of just 6 MHz. Moreover, this obtained resolution improvement can be appreciated by looking at Figure 6, in which the approximated Impulse Response Function (IRF) of the Biomass mission is compared with the IRF resulting from the tessellation presented in Figure 5.

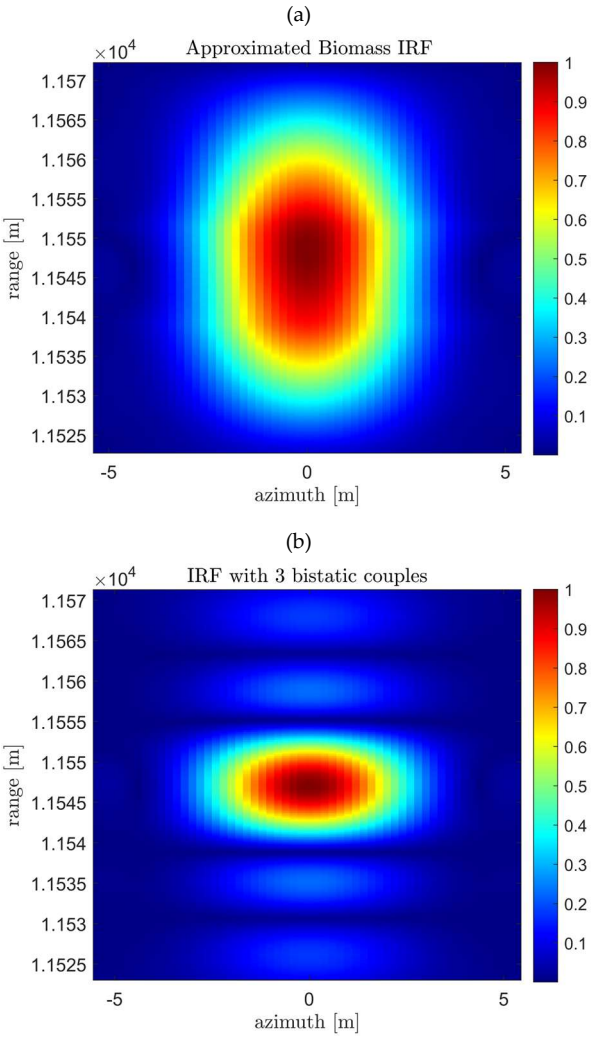

Figure 6: Approximated Biomass IRF and IRF with 3 bistatic couples

Biomass is a monostatic P-Band SAR mission, thus its range resolution is 24.98 m, as it can noticed also by looking at Figure 6 (a). On the other hand, by inspecting Figure 6 (b), it can be noticed that by employing 3 bistatic couples the obtained effect is equivalent to have a three times larger available bandwidth. Indeed, the same result as the one

presented in Figure 6 (b) can be obtained by simulating a system with the same specifications of Biomass except for a larger bandwidth of 18 MHz.
At this point it is worth mentioning that the plots in this section result from simulations which have been carried out by means of a proper *MATLAB* code; a simulator specifically written with the aim of carrying on Multi-static Wavenumber Tessellation experiments and analysing the obtained improvements in terms of range resolution, by computing the IRFs via Time Domain Back Projection (TDBP). Moreover it has to be remarked that all the presented coverage maps are referred to SAR couples for which the ψ_{tx} and ψ_{rx} are symmetric (thus $\psi_{tx} = -\psi_{rx}$), in order to obtain tiles which are always centred around the 0 of the K_x axis and only displaced along the K_r direction, leading to the very easy to read plots of this section.

3. SAR fleets design

The intent of the presented thesis, is to develop specific theoretical and computer tools aimed to deal with the multi-static SAR (MultiSAR) fleet design and the exploitation of the just mentioned MWT concept. In particular, these computer tools, built on *MATLAB*, are intended to assess the performance of preliminary multi-static SAR fleet designs, extending the existing analytical tools for the monostatic SAR system performance analysis to the multi-static SAR case. By means of these instruments, two feasible and promising MultiSAR constellations, differing for the receiving antenna dimensions, have been designed, featuring one receiver and three transmitters, flown on the same orbit (approximated as a straight line and) with a different true anomaly.
These two fleet configurations, with the separations L among the receiver and each transmitter illustrated in Table 1, result into the perfect tessellation shown in Figure 5, thus to the remarkable range resolution enhancement depicted in Figure 6 (b).

Transmitter	1	2	3
L	250 km	360 km	450 km

Table 1: Distances needed to perform the MWT

A sketch of these SAR constellations is shown in Figure 7.

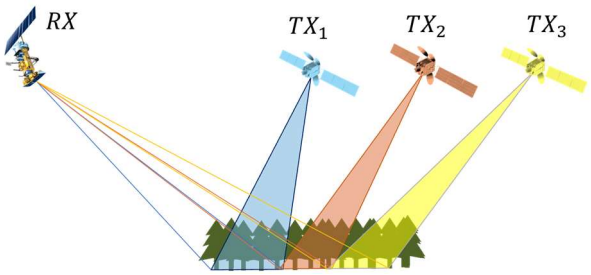

Figure 7: Constellation sketch

The basic fixed design parameters, which are in common to both the configurations and to transmitters and receiver, are shown in Table 2.

f_0	435 MHz	Center frequency
B	6 MHz	Bandwidth
λ	0.689 m	Wavelength
H	600 km	Orbital height

Table 2: Fixed parameters

It is also very important to highlight that the two designs have been carried out taking into account one of the main requirements coming from the Biomass mission, namely the necessity to guarantee a NESZ of at least -27 dB within all the ground swath. Moreover, to be consistent with the ESA mission, the proposed fleets have been designed to feature a ground swath almost equal to the one of Biomass [7]. Of course, to fulfil this NESZ constraint, the transmitted power has been regulated differently in the two configurations.
Furthermore, in both the proposed constellations the receiving satellite has been designed to use an antenna-array composed by different panels, that in turn are made of different patch antennas, as it is done in [4], in which every panel has the form presented in Figure 8.

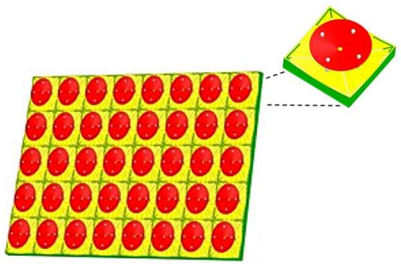

Figure 8: Array panel and patch antenna magnification *@NASA Goddard Flight Center*

What changes between the two configurations is the number of panels employed in the receiving array. The reason behind the choice of using an array in reception is that, with a phased array, it is possible to electronically steer its radiation pattern towards the desired transmitting satellite at each time, thus allowing as many pointing directions as are the illuminators (RADAR jargon to indicate the transmitters). To mimic this electronic beam steering, a proper combination of the radiation patterns of transmitters and receiver has been performed for each pointing condition. To visualize the effect of this procedure, the received signals resulting from the first fleet design are shown in the plots in Figure 9.

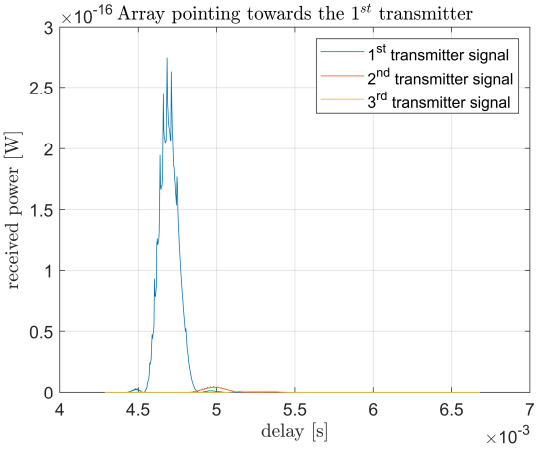

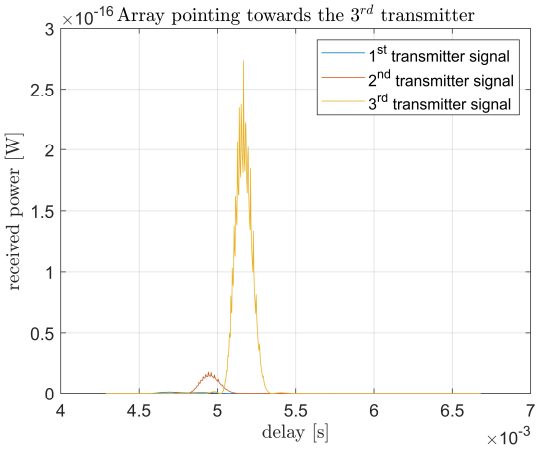

Figure 9: Received power Vs time delay

3.1. Transmitters

The SAR systems in transmission employ a parabolic antenna to mimic as much as possible the Large Deployable Reflector of Biomass. The main features of the illuminators, supposed to be all alike among them and in both the configurations, are explored in Table 3.

W	55 km	Ground swath
$\Delta\theta$	3.94°	Elevation beamwidth
$\Delta\psi$	3.94°	Azimuthal beamwidth
D	12.23 m	Parabolic antenna diameter
A_s	48.60 km	Maximum synthetic aperture
ρ_x	5.01 m	Azimuthal resolution
PRI	6.56×10^{-4} s	Pulse repetition interval
PRF	1.52×10^{3} Hz	Pulse repetition frequency
G	32.70 dB	Antenna gain
A_e	70.34 m^2	Antenna effective area
δ	15%	Duty cycle
T	9.84×10^{-5} s	Transmitted pulse duration

Table 3: Transmitters' parameters

3.2. Time Division Multiple Access

In these SAR formations, the transmitters are assumed to operate under the principle of Time Division Multiple Access (TDMA). In this way the signals associated with the individual transmissions can safely reach the receiver with the smaller possible temporal overlap, still fitting within one transmitters' PRI duration to avoid range ambiguities. For this reason, the transmission scheme has been implemented by enforcing a proper synchronization plan among the illuminators. As said, the separations between the satellites must be set as shown in Table 1 to achieve the desired range resolution enhancement, but with those distances it is impossible to implement a correct TDMA scheme because the signals would reach the receiver with a huge overlap among them. Nevertheless, this problem can be easily solved by letting the illuminators transmit the signals with some delay one with respect to the other. Having evaluated the delay with which each signal has to reach the receiving array to optimize the TDMA, the transmission scheme can be regulated according to these delays that are shown in Table 4.

Transmitter	2	3
Delay w.r.t. the previous received signal - 1st fleet	$2.78 \times 10^{-4} s$	$1.82 \times 10^{-4} s$
Delay w.r.t. the previous received signal - 2nd fleet	$2.49 \times 10^{-4} s$	$2.28 \times 10^{-4} s$

Table 4: Delays needed to implement the TDMA

For instance, in Table 4, it can be read that, in the first configuration, the signal emitted by the second transmitter must reach the receiver after $2.78 \times 10^{-4} s$ from the reception of the first one, while the signal from the third illuminator has to reach the array after $1.82 \times 10^{-4} s$ from the reception of the signal from the second transmitter. Even if enforcing a proper synchronization plan among the illuminators, based on the delays shown in Table 4, leads to avoid an excessive overlap between subsequent signals, a situation of null temporal overlap is impossible. For this reason, at a certain point, the received signals have been cut to avoid destructive interference.

The adopted principle behind the signal cut is the following: the main signal is cut $20\,dB$ above the interference from the other beams. This means that, as soon as the difference between the main signal power and the power of the unwanted echoes reaches $20\,dB$, the signal has been cut. The main signal, for each one of the three array pointing directions, is the one emitted by the illuminator towards which the array is oriented, while the other two signals, emitted by the other two transmitters, are read by the array as an interference, therefore as noise. The latter is for sure a strict requirement, since it implies that from the moment the main signal intensity becomes less than 100 times greater than the intensity of the interfering signals, the main signal is cut, nevertheless this criterion guarantees high performance in terms of interference rejection.
Moreover, it has to be pointed out that to take into account the fact that all the received signals have to fit in one PRI duration, also the signal from the third transmitter, belonging to the previous PRI, and the first signal belonging to the next PRI have been considered as interference in the first and third signal cutting, respectively.

3.3. First fleet configuration

The power transmitted in this first configuration has been set as $P_{tx} = 100\,W$ and in Table 5 the features of the array employed in this first design are listed.

Lx_{patch}	$0.3\,m$	Azimuthal length of the patch antenna
Lz_{patch}	$0.3\,m$	Elevation length of the patch antenna
N_{patch_x}	8	Number of patch antennas along x
N_{patch_z}	8	Number of patch antennas along z
N_{panel_x}	4	Number of panels along x
N_{panel_z}	2	Number of panels along z
Lx_{array}	$9.6\,m$	Azimuthal length of the array
Lz_{array}	$4.8\,m$	Elevation length of the array
$\Delta\theta_{array}$	8.22°	Array elevation beamwidth

$\Delta\psi_{array}$	4.11°	Array azimuthal beamwidth
ρ_x	4.8 m	Array azimuthal resolution
G	29.31 dB	Array gain
A_e	32.26 m^2	Antenna effective area

Table 5: Array parameters – 1st fleet configuration

It has to be clarified that, since the array is formed by combining multiple patch antennas, its radiation pattern is influenced by the individual radiation patterns of all these small antennas. To take into account this detail, the receiver radiation pattern has been always accurately simulated also considering the pattern of the patch antennas. This further accuracy in the computations plays a significant role in the final results, bringing the designs closer to a real scenario, besides the fact that it also represents an additional degree of freedom for the designs. For this configuration the resulting received signals, for each bistatic couple after the illustrated cutting procedure, are presented in Figure 10.

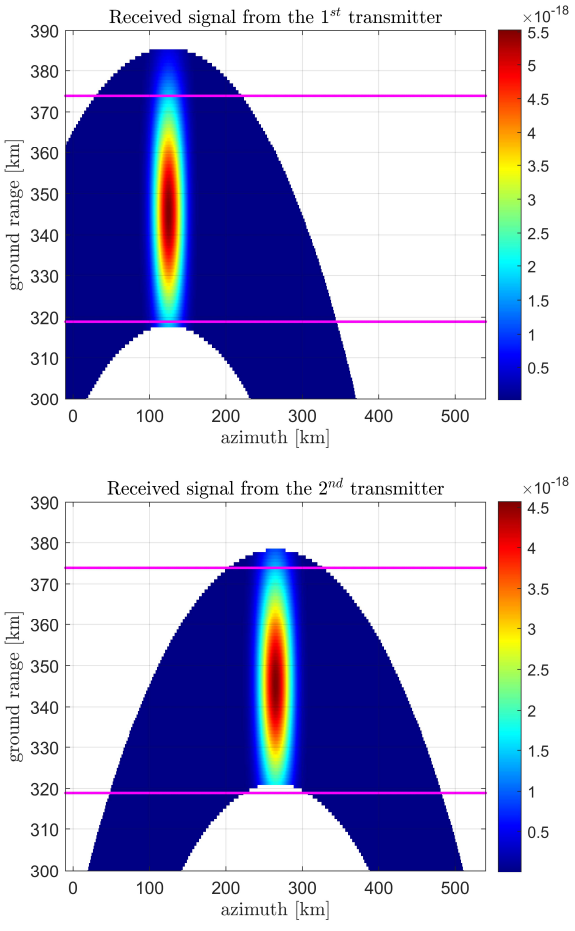

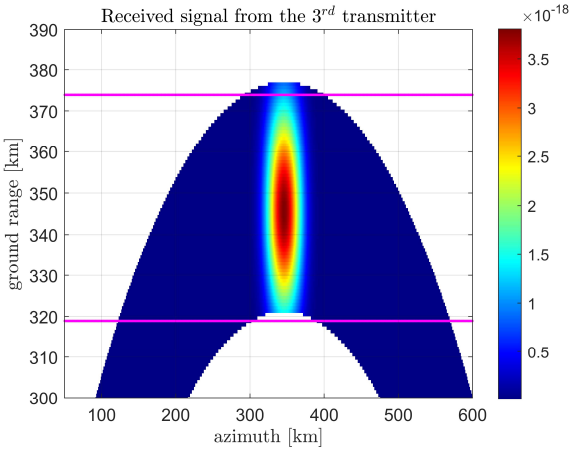

Figure 10: Cut received signals magnification – 1st fleet configuration

In these last plots the magenta lines represent the 55 km swath width, coming from the transmitters' parameters (see Table 3). Moreover, these plots are magnified in order to better check the swath loss caused by the cuts and its magnitude. Indeed, it can be noticed that obviously the ground range coverage results to be reduced after the cutting procedure and in particular, by looking at the signals received from the second and third transmitters, it is clear that the system is not capable of illuminating all the all the 55 km ground swath. Nevertheless, the design has been optimized in terms of signals' overlap, in fact the swath loss is of just 2 km in these two cases, while the signal from the first transmitter is not affected at all by this issue.

Thus, by looking at Figure 10, it is possible to establish that the presented MultiSAR fleet is capable of imaging a ground swath of 53 km. Concluding this discussion about the ground range coverage, it has to be underlined that this swath loss could have been avoided by setting a less strict requirement for the cutting procedure (e.g., if the main signal had been cut 17 dB above the interference from other beams, instead of 20 dB). In any case, also with this less strict constraint, it is clear that, the addition of another illuminator with the TDMA scheme would have been impossible, without an unacceptable reduction in the ground swath coverage.

Moreover, the obtained results of the Noise Equivalent Sigma Zero evaluation, for each bistatic couple of the presented fleet design, are presented in Figure 11.

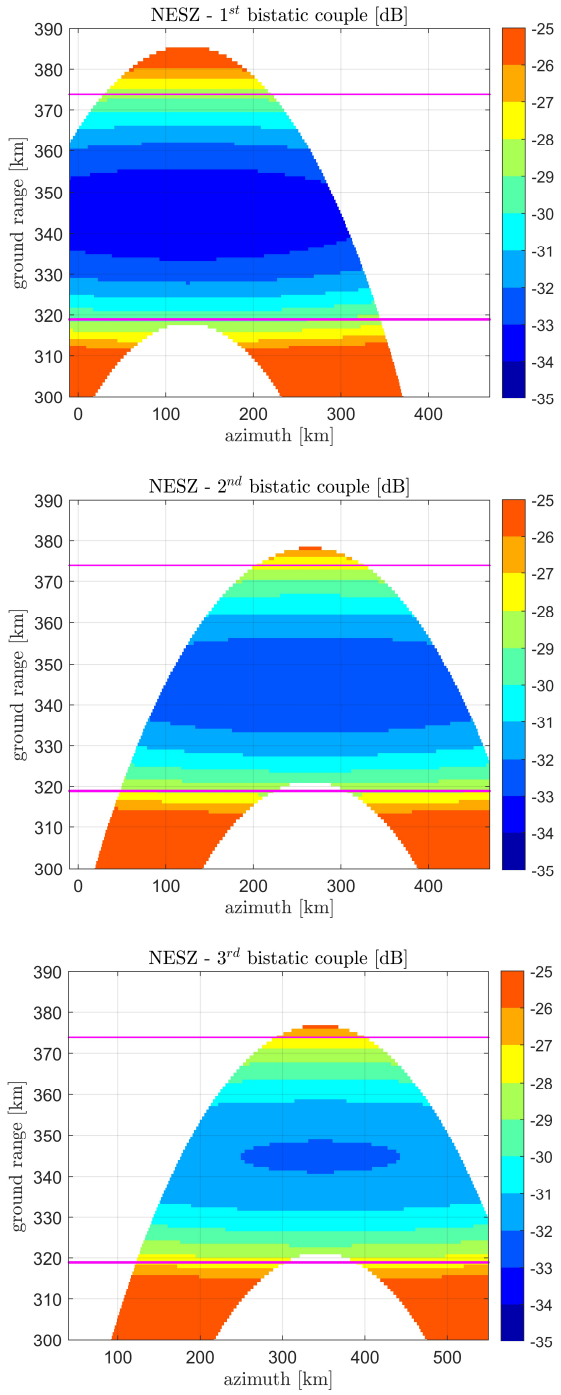

Figure 11: NESZ – 1st fleet configuration

As it is evident the Biomass mission threshold of $-27\ dB$ is not only perfectly respected but it is also surpassed, since in almost all the swath the NESZ has a value of around $-30\ dB$ or even better.

3.4. Second fleet configuration

The power transmitted in this second configuration has been set as $P_{tx} = 180\ W$ and in Table 6 the features of the designed array are listed.

Lx_{patch}	0.3 m	Azimuthal length of the patch antenna
Lz_{patch}	0.3 m	Elevation length of the patch antenna
N_{patch_x}	8	Number of patch antennas along x
N_{patch_z}	8	Number of patch antennas along z
N_{panel_x}	4	Number of panels along x
N_{panel_z}	1	Number of panels along z
Lx_{array}	9.6 m	Azimuthal length of the array
Lz_{array}	2.4 m	Elevation length of the array
$\Delta\theta_{array}$	16.45°	Array elevation beamwidth
$\Delta\psi_{array}$	4.11°	Array azimuthal beamwidth
ρ_x	4.8 m	Array azimuthal resolution
G	26.30 dB	Array gain
A_e	16.13 m^2	Antenna effective area

Table 6: Array parameters – 2nd fleet configuration

In this case the resulting received signals, after the cutting procedure, are the ones presented in Figure 12.

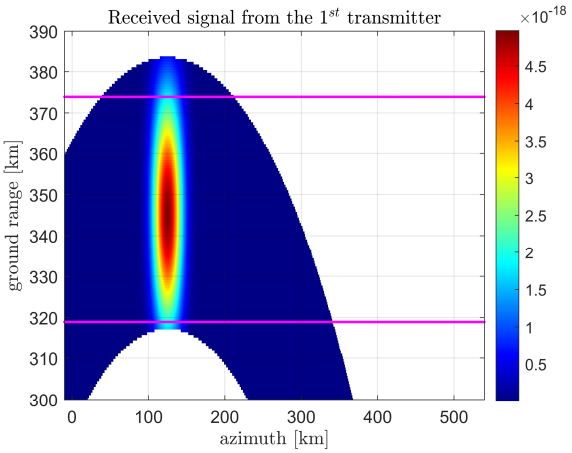

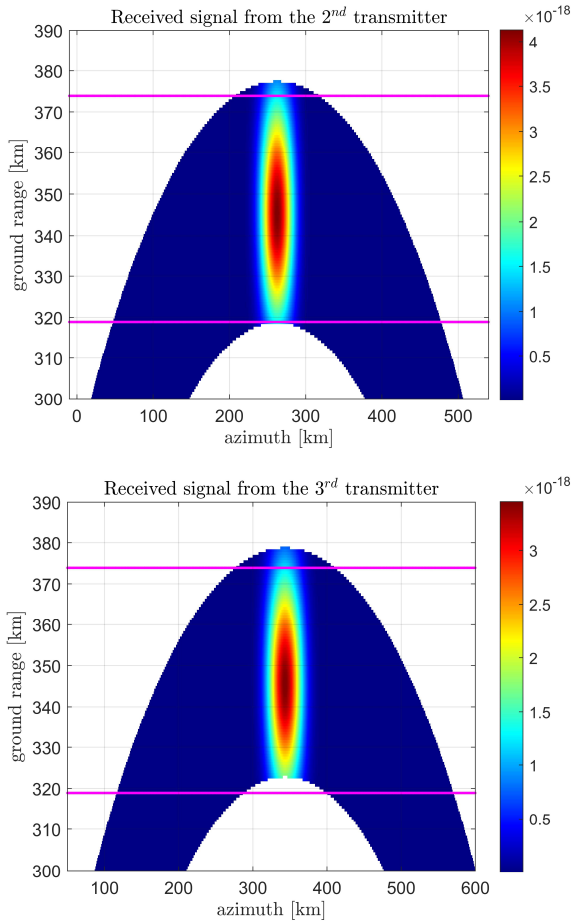

Figure 12: Cut received signals magnification – 2nd fleet configuration

It can be noticed that also in this configuration the ground swath of the illuminators results to be not fully covered after the cutting procedure. In particular, the signal received from the third transmitter exhibits a swath loss of 4 km, thus the presented MultiSAR configuration is capable of imaging a ground swath of 51 km. Also in this case it is evident that the addition of another illuminator would have been impossible. Moreover, the results of the Noise Equivalent Sigma Zero evaluation are shown in Figure 13.

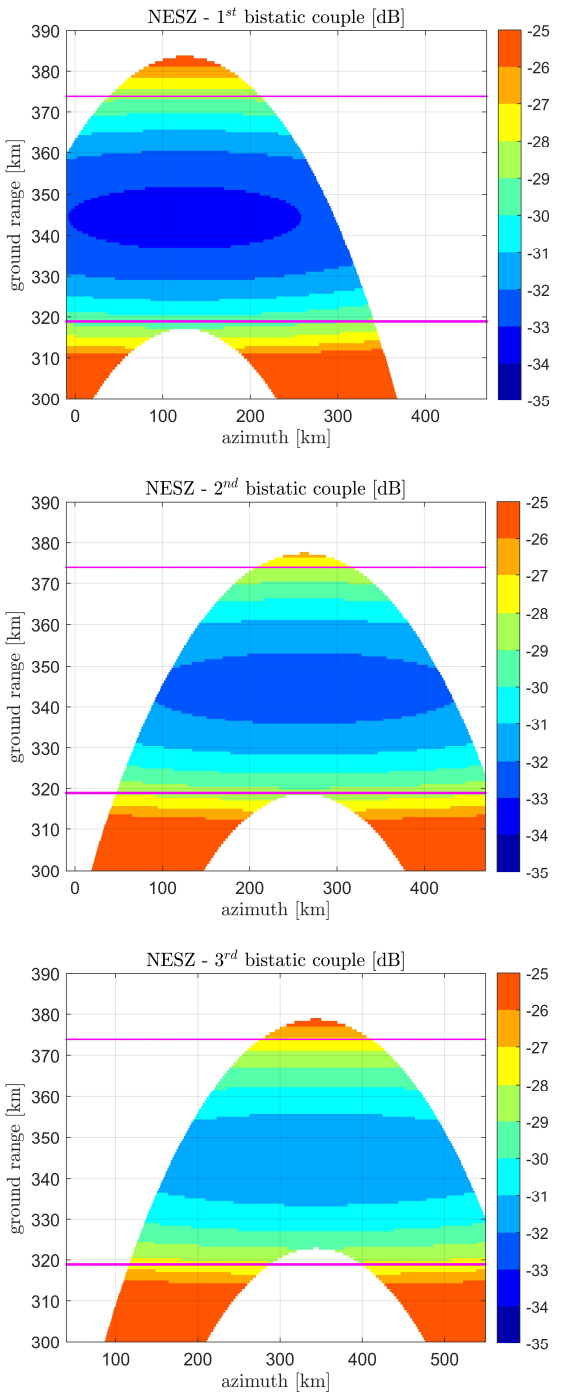

Figure 13: NESZ – 2nd fleet configuration

Also in this configuration it is evident that the NESZ never goes below the threshold value of $-27\ dB$, indeed, in the vast majority of the ground swath, it is around $-30\ dB$. It has to be remarked that, as expected, due to the smaller G and A_e, the NESZ appears to be lower than in the previous case, even if a higher transmitted power has been employed.

In conclusion, this configuration is for sure lighter and smaller than the first one presented, because the array dimension is halved in the elevation

direction, but this MultiSAR design requires almost twice the power in transmission and it also presents worst results in terms of NESZ (still fulfilling the Biomass requirement) and swath coverage.

3.5. Earth coverage

At this point it is also interesting to look at the results coming from an approximated evaluation of the MultiSAR fleets Earth coverage performance that has been carried on.
In Table 7 they are shown the days needed to image both the Amazon Forest and the equatorial belt with the 3 different ground swath values (the one from the transmitters' parameters and the achievable ones with the two designed fleets).

W	$coverage_{AMAZON}$	$coverage_{EQUATOR}$
55 km	37 days	49 days
53 km	38 $days$	51 days
51 km	40 days	53 days

Table 7: Earth coverage simulations' results

In this way it has been quantified how the swath loss, presented in the previous subsections, impacts on the time required to achieve the desired Earth coverage.

4. Discussion and conclusions

As it is evident by looking at the just presented results, the developed tools have allowed to design two feasible and promising P-Band multi-static SAR fleets, featuring a relevant range resolution enhancement, high performance in terms of NESZ and good results also with respect to the ground swath coverage, still operating with the prescribed 6 MHz bandwidth. Furthermore, another strength of the presented fleets is that, while still providing a remarkable NESZ of around $-30\,dB$ in all the imaged swath of more than 50 km, they require very low power in transmission (namely 100 W and 180 W), even employing a quite small receiving array in reception.
Moreover, it is worth highlighting that the *MATLAB* tools giving the presented results can be adapted to test a huge variety of constellation designs, with different number of transmitters, bandwidth, center frequency, swath, etc… in other words, all the parameters just shown in Table 3, 5 and 6 can be changed to evaluate the performance and the tessellation results of completely different fleets still using the same codes.
The limit of this work dwells in the non-trivial assumption of weak scattering, which has been made to derive the Multi-static Wavenumber Tessellation principle and may not hold for scenarios of interest at P-Band, namely forests, ice, desert sands [7]. Indeed, it needs to be tested through specific studies, concerning both forward modeling and propaedeutic SAR campaign data analysis. Nonetheless, several P-Band SAR campaigns have already been carried out, specifically in the field of bistatic SAR, for instance, encouraging findings have been reported in [8]. Furthermore, even if it is undeniable that the Born approximation does not hold for every scenario, concerning the usage of SAR for biomass investigation, also the results observed in bistatic SAR surveying of forested areas in Northern Europe are promising, as illustrated in [9] and [8].
In addition, further iterations of the proposed designs should definitely look into the effects produced both by Earth's rotation and curvature. Luckily, substantial literature already exists on the subject, in fact a relevant example of assessment and compensation of the effects of Earth's curvature and rotation can be found in [10]. Moreover, also the orbital perturbations should be considered in further developments, to evaluate exactly the satellites ground tracks and their time evolution. In this way it would be possible to deliver a much more precise estimation of the time required by the fleets to cover the Amazon Forest or any other area of interest.
Furthermore, it may be worth to perform a quantitative comparison, in terms of NESZ, between the results obtained in this thesis and the ones achievable by employing the approach based on the simultaneous transmission of all the satellites, proposed in [11].
To conclude, the just described enhanced definition of the imaging products, could also be applied in the SAR tomography field, by adding other receivers on different orbits. This technique, paired with the superior penetration capabilities of the P-Band, could bring novel insight on biomass estimation.

5. Bibliography

[1] ESA Earth Observation Portal, "Biomass (Biomass monitoring mission for Carbon Assessment)," [Online]. Available: https://directory.eoportal.org/web/eoportal/satellite-missions/b/biomass. [Accessed 2021 October 9].

[2] International Union for Conservation of Nature, *Forests and climate change,* Gland, 2021.

[3] European Space Agency, *Report for Mission Selection: Biomass (SP-1324/1),* 2012.

[4] NASA Goddard Flight Center and University of Arizona, "Space Exploration Synthetic Aperture RADAR (SESAR)," in *52nd Lunar and Planetary Science Conference (LPI Contrib. No. 2548)*, 2021.

[5] Ru-Shan Wu and M. Nafi Töksoz, "Diffraction tomography and multisource holography applied to seismic imaging," *Geophysicists,* vol. 52, no. 1, pp. 11-25, January 1987.

[6] S. Tebaldini and F. Rocca, "Multistatic Wavenumber Tessellation: ideas for high resolution P-Band SAR missions," in *IEEE International Geoscience and Remote Sensing Symposium (IGARSS)*, 2017.

[7] European Space Agency, *Report for Mission Selection: Biomass (SP-1324/1),* May 2012.

[8] L. M. H. Ulander, P. Frölind, A. Gustavsson and G. Stenström, "Bistatic P-band SAR signatures of forests and vehicles," in *2012 IEEE International Geoscience and Remote Sensing Symposium*, 2012.

[9] L.M.H. Ulander, A. Barmettler, B. Flood, P.-O. Frölind, A. Gustavsson, T. Jonsson, E. Meier, J. Rasmusson, G. Stenström, "Signal-to-clutter ratio enhancement in bistatic very high frequency (VHF)-band SAR images of truck vehicles in forested and urban terrain," *IET Radar, Sonar & Navigation,* vol. 4, no. 3, p. 438–448, June 2010.

[10] J. Mohr and S. Madsen, "The impact of curved satellite tracks on SAR focusing," *IGARSS 2000. IEEE 2000 International Geoscience and Remote Sensing Symposium. Taking the Pulse of the Planet: The Role of Remote Sensing in Managing the Environment. Proceedings (Cat. No.00CH37120),* vol. 1, pp. 87-79, 2000.

[11] L. Flora, *MSc thesis: A Multi-Static Spaceborne SAR Formation for High-Resolution Imaging at Longer Wavelengths,* Milano, 2020.

POLITECNICO
MILANO 1863

School of Industrial and Information Engineering
Department of Aerospace Science and Technology

MASTER OF SCIENCE
IN SPACE ENGINEERING

Analysis of Multi-Static Spaceborne SAR Formations for High-Resolution Imaging at P-Band

ADVISOR:
Stefano Tebaldini

CANDIDATE:
Martina Stasi
(ID: 925217)

A.Y. 2020-2021

"I could either watch it happen

or be a part of it."

-E. Musk

Abstract

The aim of this thesis is to present the developed theoretical and computer tools needed to perform the preliminary design of a feasible space mission for a multi-static Synthetic Aperture RADAR (SAR) campaign working at P-Band. The ultimate goal of the design is to use the data coming from different satellites to overcome the fundamental resolution limit of P-Band spaceborne RADARs, which results from the $6\ MHz$ bandwidth restriction imposed by the International Telecommunication Union.

To face this small frequency range availability, which is the major drawback of the P-Band scenario, this dissertation leverages the principle of Multi-static Wavenumber Tessellation (MWT) in the peculiar case of multiple satellites equipped with a transmitting SAR and only one receiving spacecraft. Indeed, by exploiting this technique, derived from the Fundamental Equation of Diffraction Tomography, it is possible to significantly enhance the system spatial resolution by properly setting the relative positions of transmitters and receiver along the orbit.

To allow the correct implementation of this concept much effort has been spent on the preliminary design of antennas and transmission scheme. The antennas have been discussed by considering solutions present in literature like the parabolic reflector of the ESA Biomass mission and the planar array proposed by NASA JPL in the SESAR project.

The transmitters are assumed to operate under the principle of Time Division Multiple Access (TDMA), so that the signals associated with the individual transmissions can safely reach the receiver with no temporal overlap. For this reason, the transmission scheme has been implemented by enforcing a proper synchronization plan among the transmitters.

The design of antennas, orbital positioning and TDMA scheme has been carried out by developing proper computer tools to assess the performance of preliminary multi-static SAR fleet designs. These tools, specifically drawn up for this thesis, are aimed to extend the existing analytical tools for the monostatic SAR system performance analysis to the multi-static SAR case.

As result, two promising and feasible multi-static SAR fleet solutions are proposed, featuring a range resolution three times finer with respect to a conventional monostatic P-Band SAR and a Noise Equivalent Sigma Zero of around $-30\ dB$ within a ground swath of more than $50\ km$.

Key-words: remote sensing, multi-static SAR, P-Band, Time Division Multiple Access, Diffraction Tomography, Multi-static Wavenumber Tessellation.

Abstract

Italian version

Lo scopo di questa tesi è presentare gli strumenti teorici ed informatici che sono stati sviluppati al fine di poter creare il design preliminare di una missione basata sull'utilizzo di una costellazione di RADAR ad apertura sintetica (SAR) multi-statici operanti in P-Band. Il fine ultimo di questo progetto è usare i dati provenienti da diversi satelliti per risolvere il problema della scarsa risoluzione spaziale, causato dalla limitatezza della banda disponibile che è di appena $6\,MHz$ a causa delle restrizioni imposte dall'Unione Internazionale delle Comunicazioni.

Per supplire a tale vincolo, che è la maggiore criticità riscontrabile nel lavorare in P-Band, questo studio sfrutta il concetto di Multi-static Wavenumber Tessellation (MWT) applicato al caso peculiare di molteplici SAR trasmittenti ed un solo ricevitore. Infatti, avvalendosi del suddetto principio, derivante dall' Equazione Fondamentale della Tomografia Diffrattiva, è possibile migliorare significativamente la risoluzione spaziale mediante un'opportuna scelta delle posizioni relative dei trasmettitori e del ricevitore lungo l'orbita.

Per assicurare una corretta implementazione del concetto di MWT, una notevole attenzione è stata posta sul design preliminare delle antenne e dello schema di trasmissione. Le antenne sono state trattate considerando alcune soluzioni presenti in letteratura, quali: il riflettore parabolico della missione Biomass dell'ESA e l'array planare proposto dal NASA JPL nel progetto SESAR.

I trasmettitori operano sotto il principio di Time Division Multiple Access (TDMA), in modo che i segnali associati alle diverse trasmissioni possano raggiugere il ricevitore senza rischiare una sovrapposizione temporale. Per questa ragione, lo schema di trasmissione è stato implementato imponendo un'opportuna sincronizzazione tra i satelliti trasmettitori.

Il design delle antenne, del posizionamento orbitale e del suddetto schema di trasmissione è stato condotto sviluppando strumenti informatici specifici per valutare le prestazioni dei design preliminari di costellazioni di SAR multi-statici. Questi strumenti, appositamente creati per questa tesi, sono finalizzati ad estendere gli strumenti analitici esistenti per la valutazione delle performance dei SAR monostatici al caso multi-statico.

Come risultato finale, sono proposti due fattibili e promettenti design di costellazioni di SAR multi-statici, caratterizzati da una risoluzione in range tre volte più fine rispetto a quella di un tradizionale SAR monostatico e da un valore di Noise Equivalent Sigma Zero di circa $-30\,dB$ all'interno di un *ground swath* di più di $50\,km$.

Parole chiave: remote sensing, SAR multi-statico, P-Band, Time Division Multiple Access, Diffraction Tomography, Multi-static Wavenumber Tessellation.

Acknowledgements

First and foremost, I would like to express my deepest gratitude to my supervisor Stefano Tebaldini for his essential and constant support, trust and interest for the work I carried out during these last months for my thesis. His dedication and passion for the SAR systems, besides his great expertise, were so evident during his course that he made me and my fellows passionate about his subject. Indeed, it is mostly thanks to him if I got closer to this incredible field and I would never thank him enough, since this period has been one of the most intense, motivating and challenging of my academic career but, for these reasons, also the most exciting one. It was both a privilege and a great opportunity to rely on his knowledge and willingness to help me out and guide me during this amazing journey.

Furthermore, I clearly have to thank my beloved parents and my sister for their constant and reassuring presence, which has never been limited by our physical distance. They have always believed in me, guided me and supported me, when I needed it and especially when I did not know I needed it. Even if there are no words that would be sufficient to thank them, I have to say that I feel deeply blessed to be able to call them my family.

Moreover, I want to acknowledge my dear grandparents for always being so proud of my academic career to motivate me to do always better. I do wish my grandpa was still here to see me in this moment because I'm sure that this great achievement of mine would have been his greatest pride.

Last but not least, I would like to thank my dearest friends Daniele, Antonio, Nicola, Susanna and Alessio for their love and for always being by my side both in difficulties and in good times. Each one of them helped me getting where I am now: Daniele being my greatest supporter, in every possible way, for more than 6 years, Nicola and Antonio always understanding me and putting me in a good mood, even in the worst situations, and Susanna and Alessio believing in me, helping me to overcome all the difficulties I encountered in these two years and being the best teammates ever. Without them nothing would have been the same, and I am so sorry that the pandemic took us away so much precious time we could have spent together.

Contents

1 Introduction 1
1.1 Problem statement and scientific context 1
1.1.1 Climate change 3
1.1.2 P-Band 5
1.1.2 Earth Explorer Biomass mission 6
1.1.3 NASA SESAR mission 8
1.1.4 SAR formations 9
1.2 Outline 10
2 Synthetic Aperture RADAR imaging 11
2.1 SAR fundamentals 11
2.1.1 SAR resolution 17
2.1.2 Antenna gain and radiation pattern 21
2.1.3 RADAR equation 23
2.1.4 SNR and NESZ 25
2.2 SAR processing 27
2.2.1 Range compression 28
2.2.2 Azimuth compression 31
2.3.2.1 Time Domain Back Projection (TDMA) 31
2.3 Bistatic and multi-static SAR 33
3 Multi-static Wavenumber Tessellation 37
3.1 Fundamental Equation of Diffraction Tomography 37
3.2 Equivalent bandwidth extension 40
3.3 Simulations and results 46
4 SAR Fleets design 56
4.1 MultiSAR fundamentals 57
4.1.1 Time Division Multiple Access 59
4.2 Simulations and results 62
4.2.1 Transmitting SAR systems 64
4.2.2 Receiving array outline 67
4.2.3 First fleet configuration results 68
4.2.4 Second fleet configuration results 82

4.2.5 Earth coverage 92
4.3 Range resolution enhancement via MWT 95
5 Discussion and conclusions 100
6 Bibliography and Sitography 103

List of Figures

Figure 1.1: Frequency spectrum division ©ESA 3
Figure 1.2: Wavelengths' penetration capability 5
Figure 1.3: Scatterers for different wavelengths ©ESA 6
Figure 1.4: Rendering of the Biomass mission payload ©ESA 6
Figure 1.5: S-Band and P-Band images of the Mare Serenitatis on the Moon 9
Figure 2.1: Raw data matrix construction for a point target 12
Figure 2.2: Scheme of a side-looking monostatic SAR 13
Figure 2.3: SAR frontal view 15
Figure 2.4: Example of nadir echo in a SAR image 16
Figure 2.5: SAR resolutions 18
Figure 2.6: Resolution cell of a monostatic SAR 19
Figure 2.7: Resolution ring of a monostatic SAR 19
Figure 2.8: Antenna pattern example 22
Figure 2.9: Transmission-reception scheme of a bistatic couple 25
Figure 2.10: Raw data matrix example for a point target 28
Figure 2.11: Range compressed data matrix for a point target 30
Figure 2.12: Focused image of a single point target 33
Figure 2.13: Bistatic SAR scheme 34
Figure 3.1: Geometry of the basic scattering experiment 38
Figure 3.2: Wavenumber vectors for a point target in a bistatic SAR scenario 41
Figure 3.3: Decomposition of the global wavenumber vector 42
Figure 3.4: Wavenumber coverage map with one bistatic couple and no bandwidth 43
Figure 3.5: Wavenumber coverage map with one bistatic couple with bandwidth 44
Figure 3.6: Wavenumber coverage map with 4 satellites 45
Figure 3.7: Example of simulated scene 48
Figure 3.8: Wavenumber coverage map with $\Delta\psi = 10°$ 49
Figure 3.9: Wavenumber coverage map with $\Delta\psi = 20°$ 49
Figure 3.10: Wavenumber coverage map with $B = 6\ MHz$ and $\Delta\psi = 10°$ 50
Figure 3.11: Wavenumber coverage map of 2 satellites with $B = 0\ MHz$ and $L = 3.9\ km$ 51
Figure 3.12: Wavenumber coverage map of 2 satellites with $B = 6\ MHz$ and $L = 3.9\ km$ 52
Figure 3.13: Monostatic IRF and 2-satellites configuration IRF 54
Figure 4.1: Constellation sketch 58
Figure 4.2: Fleet transmission scheme 61
Figure 4.3: Array panel and patch antenna magnification *@NASA Goddard Flight Center* 67
Figure 4.4: Radiation patterns – 1st fleet configuration 71
Figure 4.5: Received power – 1st fleet configuration 73
Figure 4.6: Received power and isochronous line 74
Figure 4.7: Received power Vs time delay – 1st fleet configuration 75

Figure 4.8: Signals' cutting – 1st fleet configuration 77
Figure 4.9: Cut received signals magnification – 1st fleet configuration 78
Figure 4.10: Received signals cut at 17 dB 79
Figure 4.11: NESZ – 1st fleet configuration 80
Figure 4.12: Radiation patterns as a function only of θ – 1st fleet configuration 81
Figure 4.13: Radiation patterns – 2nd fleet configuration 84
Figure 4.14: Received power – 2nd fleet configuration 85
Figure 4.15: Received power Vs time delay – 2nd fleet configuration 86
Figure 4.16: Signals' cutting – 2nd fleet configuration 88
Figure 4.17: Cut received signals magnification – 2nd fleet configuration 89
Figure 4.18: NESZ – 2nd fleet configuration 90
Figure 4.19: Radiation patterns as a function only of θ – 2nd fleet configuration 91
Figure 4.20: Wavenumber coverage map for the designed fleets 96
Figure 4.21: Approximated Biomass IRF and IRF of the designed fleets 98
Figure 4.22: Real Biomass IRF @ESA 99

List of Tables

Table 3.1: Simulations' fixed parameters 46
Table 4.1: Simulations' fixed parameters 63
Table 4.2: Transmitters' parameters 65
Table 4.3: Array parameters – 1st fleet configuration 69
Table 4.4: Distances between each transmitter and the receiver - 1st fleet configuration 70
Table 4.5: Array parameters – 2nd fleet configuration 82
Table 4.6: Distances between each transmitter and the receiver – 2nd fleet configuration 83
Table 4.7: Simulation's parameters for Earth coverage computation 92
Table 4.8: Earth coverage simulations' results 95
Table 4.9: Delays needed to implement the TDMA scheme 95
Table 4.10: Distances needed to perform the MWT 96

Acronyms

CDMA	Code Division Multiple Access
DFT	Discrete Fourier Transform
DLR	German Aerospace Center
ESA	European Space Agency
FEDT	Fundamental Equation of Diffraction Tomography
IRF	Impulse Response Function
ITU	International Telecommunication Union
ITU-R	ITU Radiocommunication section
JPL	Jet Propulsion Laboratory
LDR	Large Deployable Reflector
LEO	Low Earth Orbit
MultiSAR	Multi-static SAR
MWT	Multi-static Wavenumber Tessellation
NASA	National Aeronautics and Space Administration

NESZ	Noise Equivalent Sigma Zero
OFDMA	Orthogonal Frequency Division Multiple Access
PolInSAR	Polarimetric Interferometric SAR
PolSAR	Polarimetric SAR
PRF	Pulse Repetition Frequency
PRI	Pulse Repetition Interval
RADAR	Radio Detection And Ranging
RCS	RADAR Cross Section
SAR	Synthetic Aperture RADAR
SESAR	Space Exploration Synthetic Aperture RADAR
SNR	Signal-to-Noise Ratio
TDBP	Time Domain Back Projection
TDMA	Time Division Multiple Access

Chapter 1
Introduction

In this introductory chapter, the main problem tackled in this thesis is presented together with a detailed explanation of the scientific context in which the solution proposed in this dissertation takes its roots. Therefore, the reasons which have led to the necessity to develop the design of a P-Band SAR technology are detailed together with its main drawback and some examples of existing projects and missions.

1.1 Problem statement and scientific context

Today the climate change is a very pressing problem to be tackled, not only for the scientific community but also for all the Earth's inhabitants. The main cause of this issue can be found in the build-up of carbon dioxide in the atmosphere that acts like a heat sink, producing the well-known greenhouse effect. Hence, the necessity of monitoring with good accuracy the global carbon cycle appears to be very urgent.

The Synthetic Aperture RADAR (SAR) technology responds perfectly to the increasing demand for accurate Earth observations, in fact it is the best geophysical tool to provide the meter-scale resolutions needed for comparison with other remote sensing techniques (optical imaging, IR spectroscopy), as well as providing data independently of lighting or weather conditions. This is because, the RADAR, and therefore also the SAR, is a technology aimed to detect and study far off targets by transmitting electromagnetic pulses at radiofrequency and observing the backscattered echoes.

Unfortunately, monitoring the global carbon cycle is a complex task, even for SAR systems, since the major natural sink for the carbon are vegetation and forests, which take the carbon dioxide from air. Indeed, forests are an issue because, to analyse what is inside and below the trees' canopies from space, it is necessary to use longer wavelengths than the usual ones employed by spaceborne RADARs, therefore the P-Band frequencies seem to be perfect.

The same problem arises when it is necessary is to study the near-subsurface region not only of the Earth, but also of planetary bodies including the Moon, Mars, Mercury, Venus, comets, icy moons and asteroids, which is an investigation that nowadays is of high interest for future human or robotic explorers. For example, a primary goal of Mars and Moon exploration is locating habitable regions and finding water because many remarkable missions are scheduled to be launched soon towards our satellite and the Red Planet, implying that a deep knowledge of their soil will be certainly crucial. In few words, the P-Band main feature, namely the long wavelengths, is urgently needed to help answer key questions in planetary science. Nevertheless, the exploitation of the incomparable penetration capability of P-Band in turn

means to work with a very limited bandwidth, due to the International Telecommunication Union (ITU) restrictions on the frequency spectrum.

For this reason, almost all the spaceborne RADARs operate in the high frequency region because a SAR system working in P-Band is constrained by a very coarse range resolution, resulting from the just mentioned bandwidth limitations.

The latter are due to the fact that the frequency spectrum is clearly shared between multiple usages, thus the frequency band allocated by the ITU to satellite operation is just a part of it. In this regard, it is worth mentioning that the International Telecommunication Union did envision a frequency allocation for present and future Earth-observation-oriented SAR missions, however ITU-R (the radiocommunication section of ITU) also set limiting boundaries for the operation of such missions. Indeed, at the time of writing, the in-force regulations constrain the SAR systems to use $6\ MHz$ of bandwidth around the center frequency $435\ MHz$, while also setting a limit in terms of Power Flux Density [1]. Going into detail, the ITU in [2] establishes[1]: a provision of up to $6\ MHz$ of frequency spectrum to the Earth active exploration-satellite service in the frequency range between 420 and $470\ MHz$ and also that this frequency interval is currently allocated to the radiolocation, fixed, amateur, space operations and mobile services. This was done out concerns of mutual interference between possible SAR P-Band satellites and pre-existing primary services operating in the same band such as the Chinese aeronautical radionavigation service and most prominently the United States Space Surveillance Network managed by the United States Air-Force.

In addition, the overall bandwidth destinated to satellite/microwave communication is also partitioned into different Bands (Ka, K, Ku, X, C, etc…) which have not equal width, in fact, as it can be visualized in Figure 1.1, the lower the frequency the narrower is the bandwidth dedicated to that specific Band.

[1] According to Resolution 727 (Rev.WRC-2000).

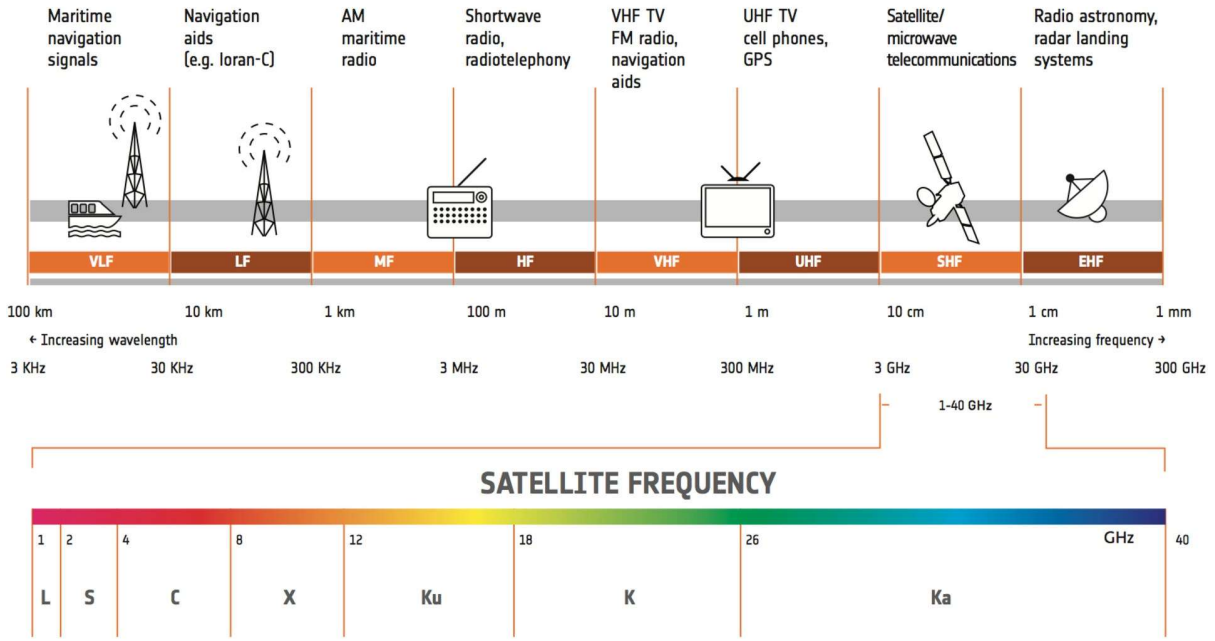

Figure 1.1: Frequency spectrum division ©ESA

As it is noticeable from this last image, the P-Band is not even present, since it should have been before the L-Band. This is because its bandwidth is remarkably smaller compared to the others and moreover, at the time of writing, the P-Band is almost unused due to this spectrum limitation. Nevertheless, in the last years, due to the necessity of monitoring the climate change and the soil of moons and other planets, the P-Band is attracting a lot of attention both from space agencies like ESA and NASA and from private companies. Furthermore, also the DLR, with the F-SAR study, is testing the low frequency region even if as an airborne system, mounted on the DLR's Dornier DO228-212 aircraft.

Staying in line with the presented context, the ultimate intent of this thesis is that of proposing a valid and feasible solution to the problem of poor resolution that arises when it is mandatory to work in the low frequency domain, as at P-band. To tackle this issue, the designed solution requires the usage of a multi-static SAR formation. Indeed, the scenario, envisioned in view of the future ESA Biomass mission and NASA SESAR mission, consists of a fleet of active satellites following a SAR receiver satellite (two promising fleet designs are presented in Chapter 4), transmitting in the P-Band using only 6 MHz as available bandwidth. As it is shown in Section 3.3 and 4.3, this multi-static SAR scenario results in a range resolution improvement proportional to the number of satellites deployed in orbit.

1.1.1 Climate change

Since the problem of climate change and environmental pollution have now become something that cannot be ignored anymore, currently a lot of attention is put on forest

preservation and environmental sustainability, in fact a growing number of factories has changed their manufacturing processes (e.g., by using partially or totally recycled materials, increasing its energetic efficiency by renewing their industrial machinery, etc…).

Forests are a stabilising force for the climate, they regulate ecosystems, protect biodiversity, play an integral part in the carbon cycle, support livelihoods, and supply goods and services that can drive sustainable growth. Forests' role in climate change is two-fold, in fact they act as both a cause and a solution for greenhouse gas emissions. It is well known that forests inhale carbon dioxide (CO2) from the atmosphere and exhale oxygen (O2) and, as trees and vegetation grow, they store the carbon which makes up about half of their total biomass. Indeed, there is strong evidence that approximately 2.6 billion tonnes of carbon dioxide, one-third of the CO2 released from burning fossil fuels, is absorbed by forests every year. In fact, the forests are responsible for up to the 90% of the terrestrial above-surface carbon pool and moreover, around half of forest biomass is composed of carbon. For this reason, the importance of the carbon absorption from the atmosphere by the forests has been recognized under the Kyoto Protocol as a critical mechanism for mitigating climate change. [3]

On the other hand, when threes die or forests are converted to other land uses, so when are cleared or burnt, they release their carbon as carbon dioxide, an important greenhouse gas. Indeed, it has been estimated that around 25% of global emissions come from the land sector, the second largest source of greenhouse gas emissions after the energy sector [4]. Averaged over the years from 2015 to 2017, the global loss of tropical forests contributed about 4.8 billion tonnes of carbon dioxide per year (or about 8-10% of annual human emissions of carbon dioxide) [5]. Furthermore the 2021 has been exceptional, since the Copernicus Atmosphere Monitoring Service of the EU found that burning forests released 1.3 gigatons of carbon dioxide only in the month of August, mostly in North America and Siberia, which have to be added to the tons produced few months before by Australian wildfires. Of course, burning fossil fuels, in combination with destruction of carbon sinks because of deforestation and other activities, has contributed to more and more carbon dioxide building up in the atmosphere, more than can be absorbed from the existing forests.

The build-up of carbon dioxide in the atmosphere (whose levels are now at their highest in human history) is driving global warming, as it traps heat in the lower atmosphere, resulting to be the major driver in the global climate change. Moreover, the carbon dioxide, stored in forests and other natural carbon sinks, will become increasingly unstable as climate change progresses. In fact, droughts, tropical storms, heatwaves and fire weather are growing in severity and frequency because of climate change. This in turn will result in additional forest losses, contributing to more and more carbon dioxide being released into the atmosphere.

Looking at this situation it is perfectly clear the necessity not only of increasing and maintaining forests in the best conditions possible, but also of monitoring with good accuracy the carbon cycles in the forests.

1.1.2 P-Band

Nowadays, regardless the high level of innovation reached in the technological and scientific field, the terrestrial ecosystems are the largest source of uncertainty in the global carbon budget and, in particular, these uncertainties lie in the spatial distribution of carbon stocks and carbon exchange as well as in the estimates of carbon emissions resulting from human activity and natural processes. In fact, even if one central parameter in the terrestrial carbon budget is the forest biomass, in most parts of the world it is poorly quantified owing to the difficulties in taking measurements from the ground and to the lack in consistency when aggregating measurements across scales [6].

Indeed, exploiting the unique sensitivity of P-band, the SAR systems could be able to deliver completely new information on the world's forests. In particular, they would be able to measure the forest above-ground biomass, trees and vegetation height and disturbance patterns across the entire biomass range, with rates and accuracy compatible with the needs of international reporting on carbon stocks and terrestrial carbon models.

The great advantage of the P-Band SAR missions lay in the fact that, thanks to the long wavelength of around 70 cm, that is peculiar of P-Band, the RADAR signal can penetrate all the forest layers. This P-Band penetration capability, shown in Figure 1.2, is what would allow the estimation of the forest biomass.

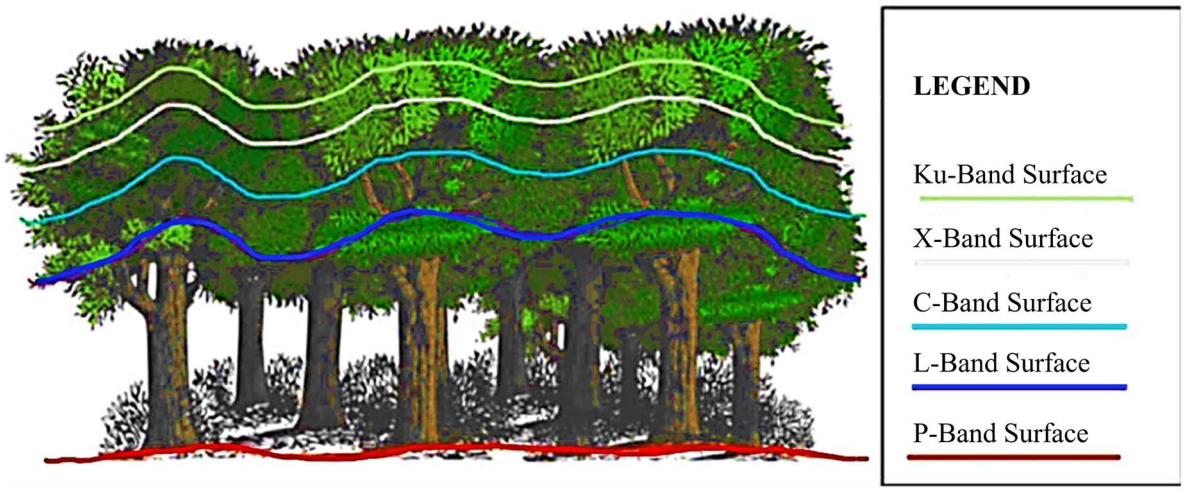

Figure 1.2: Wavelengths' penetration capability

In fact, while for SAR signals at higher frequencies (and so shorter wavelengths) the canopies of the trees act like scatterers, preventing the electromagnetic waves from reaching the soil, for P-band signals the trees' leaves are invisible.

This is due to the fact that the main scatterers for a signal are all the elements along its path having dimension in the same order of magnitude of its wavelength, concept that can be easily understood by looking at the sketch in Figure 1.3.

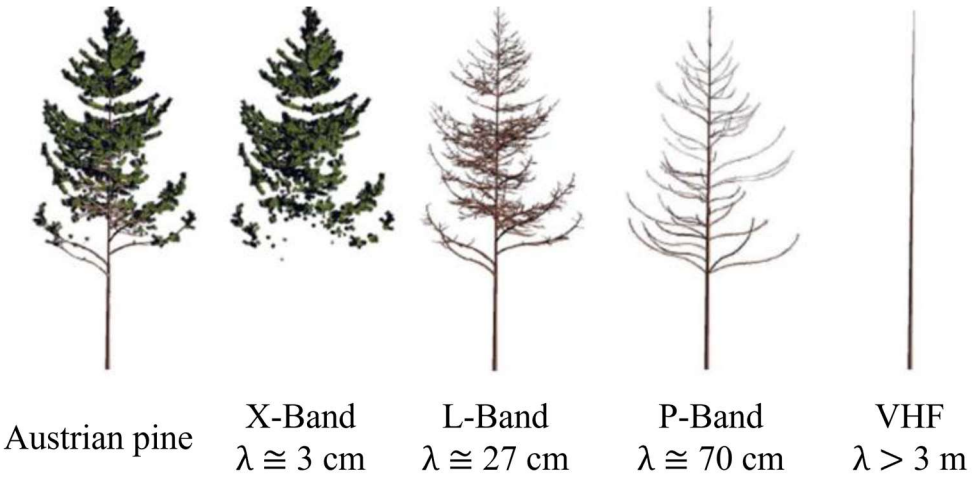

Figure 1.3: Scatterers for different wavelengths ©ESA

In addition, the P-Band signal is also resilient both to temporal decorrelation, since big branches and stems do not change as much as foliage does between the measurements, and to the motion of its scatterers, as lower frequencies have a tendency to do.

1.1.2 Earth Explorer Biomass mission

To give a concrete help in this challenging climate change scenario, in 2013 ESA selected the Earth Explorer Biomass mission[2], whose space segment is shown in Figure 1.4, to be the 7th Earth Explorer Core Mission.

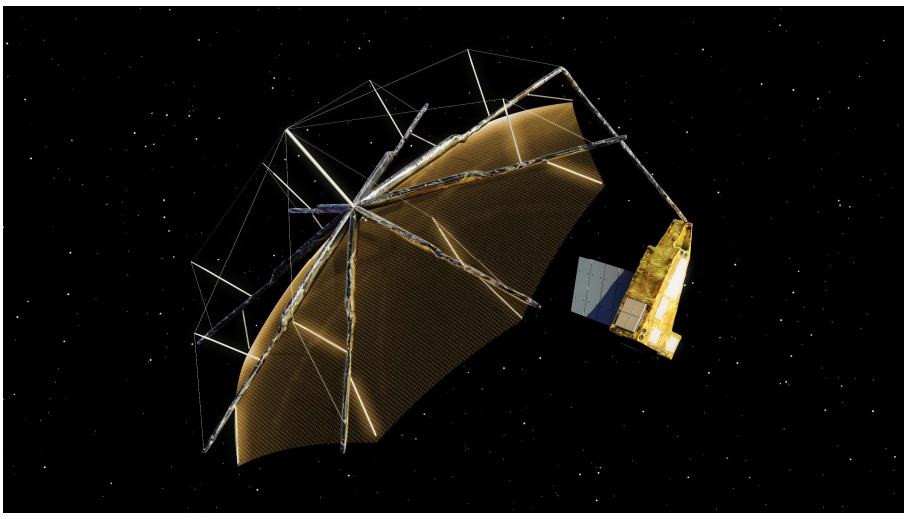

Figure 1.4: Rendering of the Biomass mission payload ©ESA

[2] At the time of writing, Biomass is scheduled for launch starting from August 2023 on a Vega launcher from Kourou, French Guiana.

The Biomass space segment will comprise a single monostatic SAR system, equipped with the huge deployable reflector clearly visible in Figure 1.4, that will be flown in a near-polar, Sun-synchronous orbit at an altitude of 637-666 km [6] and, according to the aforementioned reasons, the this mission will have the peculiarity of working in the P-band.

To pave the way for Biomass, preliminary and propaedeutic SAR campaigns have been carried out since 2004, providing results for the P-band surveying of forest biomass and height. Indeed, the data obtained comes from fully polarimetric SAR (PolSAR), polarimetric interferometric SAR (PolInSAR) and tomographic SAR and, coupled with the supporting reference measurement performed on-location, constitutes a solid scientific baseline for the upcoming Biomass mission.

The latter will be the first P-band SAR in space and it will provide the scientific community with the first ever accurate maps of tropical, temperate and boreal forest biomass. This information is urgently needed not only to improve the understanding of the global carbon cycle but also to reduce the uncertainties in the calculations of carbon stocks and fluxes associated with the terrestrial biosphere. Indeed, the atmosphere-terrestrial biosphere carbon flux is not explicitly measured at present, but it is obtained indirectly by subtracting from the atmospheric carbon increase the contributions of fossil fuel combustion and those of the ocean. This leads to an uncertainty propagation that renders the terrestrial biosphere-atmospheric flux the one with the highest level of uncertainty, even is comparable with its own order of magnitude.

Biomass will address one of the most fundamental questions in our knowledge of the land component in the Earth system, namely the status and the dynamics of forests, as represented by the distribution of biomass and how it is changing. Gaining accurate and frequent information about forest properties, at scales that allow changes to be observed, will equip the scientific community to deal with a range of critical issues with far-reaching benefits for science and society. In fact, the mission responds to the pressing need for biomass observations in support of global treaties such as the United Nations Framework Convention on climate change initiative for the reduction of emissions due to deforestation and forest degradation.

These mission objectives answer directly to the specific scientific challenges in ESA's Living Planet Programme. The latter will equip the scientific community with the instruments needed for predicting the effects the changing climate may bring in multiple fields. In fact, as the quest for knowledge continues to grow, so does our demand for accurate satellite data to be used for numerous practical applications for protecting and securing the environment. Responding to these needs, ESA's Living Planet Programme comprises a science and research element, which includes the Earth Explorer missions (like Biomass), and an Earth Watch element, that is designed to facilitate the delivery of Earth observation data for use in operational services [7].

Furthermore, exploiting the P-Band potential, Biomass data are also expected to be used for monitoring glacier and ice sheet velocities, mapping subsurface geology in deserts and mapping the topography of forest floors. Additional products and applications are likely to emerge and be evaluated during the life of the mission, but for sure the latter will also be able to provide insight on the regrowth of forests, a topic particularly interesting for tropical forests, which are

responsible for more than 70% of the world's biomass. In any case, being a monostatic system at P-Band, the Biomass SAR will be inevitably affected by the aforementioned problem of poor range resolution. Nevertheless, this issue could be solved by means of the multi-static SAR solution proposed in this thesis, which will be deeply explained and validated, through two feasible fleet designs, in Chapter 3 and 4.

1.1.3 NASA SESAR mission

Nonetheless, the ESA is not the only space agency interested in the low frequency potential, indeed, also the NASA, since the first decade of the 2000s, has shown commitment to the design of P-Band SAR systems. In fact, starting from March 2014, NASA Goddard Space Flight Center has successfully flown the P-Band airborne SAR called EcoSAR [8] which has laid the foundations for the brand new spaceborne SESAR project.

The Space Exploration Synthetic Aperture RADAR (SESAR) is a next generation P-band beamforming RADAR instrument concept, with capabilities beyond current planetary instruments, capable of providing unprecedented planetary surface and near-subsurface measurements, that will enable a new class of observations suitable to meet Decadal Survey science goals for planetary exploration [9]. In fact, as mentioned before, the P-Band features are not only needed for forests and carbon cycle investigation but also for many important planetary science and human exploration goals, which require measurements of the subsurface therefore the use of the longer wavelength possible.

This is because, the upper tens of meters of the subsurface contain stratigraphic evidence of climate change (buried fluvial channels, ice), volcanic history and evolution (lava flows, channels and tubes) and regolith development (including pyroclastic deposits and volatiles). SESAR is being specifically designed to meet science goals and strategic knowledge gaps for the Moon and Mars, but its modular design and low power compared to other SAR systems make it a candidate for other objects as well, including Venus, Earth, asteroids, and comets. Indeed, the RADAR is based on a low power, lightweight design approach conceived to meet the stringent planetary instrument requirements.

For example, on the Moon SESAR would be able to image through meters of surface-covered regolith and to provide information to characterize the near-surface stratigraphy and geology, crucial in the understanding of lunar processes and in the identification of landing sites for future lunar missions. SESAR mapping and polarimetry would also provide details about the volcanic processes that built the lunar mare and to locate and track lava tubes, important for both science and future exploration purposes. [10]

To make clearer the P-Band advantages for the planetary subsurface studies, in Figure 1.5 it is possible to appreciate the Moon's Mare Serenitatis as captured both by S- and P-Band systems.

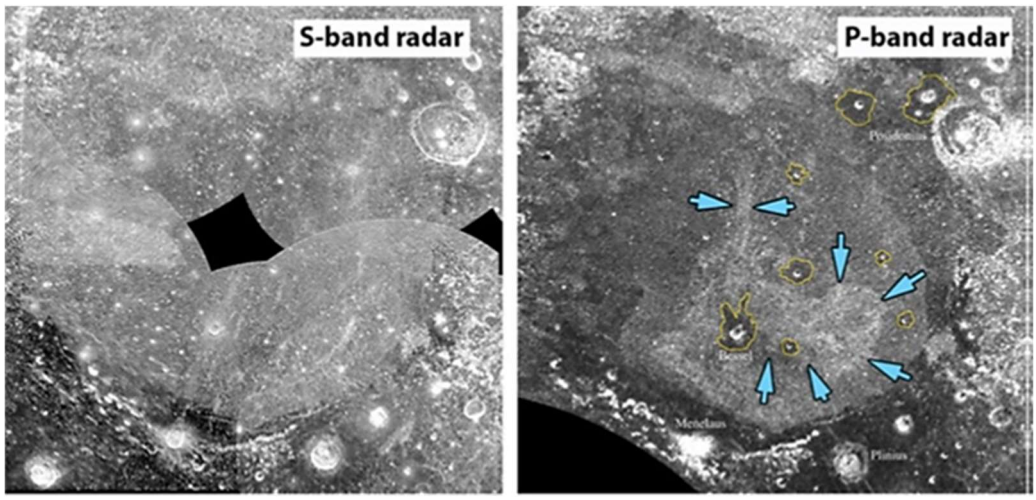

Figure 1.5: S-Band and P-Band images of the Mare Serenitatis on the Moon

The data acquired with Arecibo Observatory at P-Band, shown on the right side of Figure 1.5, reveal the existence of lava flows (indicated with cyan arrows) beneath meters of regolith, in Mare Serenitatis. On the other hand, by inspecting the left side image, it is evident that with an S-band system, whose data show primarily bright crater ejecta, these lava flows information would have been lost.

1.1.4 SAR formations

In recent years, there has been a growing market request also for spaceborne SAR constellations, supported by the progress of electronics miniaturization and cost reduction of space launches. The advantages over legacy standalone SAR satellites include the intrinsic scalability of constellations together with feasible lower costs and the diversity in geometrical configurations that can be achieved, allowing for numerous imaging products. Some examples of SAR fleets include UrtheCast's OptiSar, which offers X-Band and L-Band high resolution imaging, or the 4 satellite X-Band SAR constellation envisioned by XpressSAR.

Another very interesting SAR fleet is the one of Iceye, which plans to arrive up to 50 SAR satellites in orbit, providing remarkable imaging revisit rates on a global scale. Iceye's SAR satellite constellation already provides different angle imaging multiple times a day for specified areas of interest and, being constantly growing, it will provide very advanced imaging capabilities and access, allowing quick tactical acquisitions as well as very frequent global revisit rates. Indeed, Iceye continues to feed its SAR satellite constellation each year (it has contracted launches for several new units over the next years) even if the company successfully delivers currently data to customers worldwide from its commercial constellation of satellites [11] [12].

Very recently, on June 2020, also the U.S. owned and controlled company PredaSAR, has announced that it will launch a constellation of 48 commercial Synthetic Aperture RADAR

satellites across multiple orbits. This constellation will provide government and commercial clients with high image quality, very good global persistence and rapid data delivery [13] [14].

Broadly speaking, the popularity of constellations of small satellites is increasing even outside of the SAR imaging sphere: OneWeb Satellites, a joint venture between Airbus and OneWeb, has already put 74 small satellites in orbit to provide broadband Internet coverage and towards the same end, Spacex's Starlink counts about 1800 satellites already orbiting at the moment of writing, with a final goal of around 12.000 for the 2026 [15].

1.2 Outline

This dissertation is divided into five chapters.

In Chapter 1, a deep explanation of the scientific context in which this thesis is born as well as of the ongoing and critical issues for which it could offer a feasible answer it is given.

In Chapter 2, the SAR imaging fundamentals are detailed to give the solid background needed to fully appreciate the technicalities of the multi-static Synthetic Aperture RADAR campaign designs proposed in this thesis.

In Chapter 3, the fundamental concepts of Diffraction Tomography are explained and the derivation of the Multi-static Wavenumber Tessellation principle is performed. Subsequently the improvement that this concept is capable to bring to the SAR system imaging capabilities is discussed and validated through some examples. The latter come from different simulations that have been carried out by means of a versatile *MATLAB* code specifically drawn up for this thesis, with the aim of testing the effectiveness of the Multi-static Wavenumber Tessellation principle for all the desired fleet cases and configurations.

In Chapter 4, two feasible P-Band multi-static SAR fleet designs, resulting from another proper computer tool developed for this work, are presented in great details. Moreover their performance in terms of SAR relevant parameters is assessed and compared with Biomass mission performance, since the presented fleet projects have been carried out under some requirements and constraints taken from this ESA mission.

In Chapter 5, the conclusions of this thesis are presented. Indeed, the achievements obtained by means of the theoretical and computer tools developed are commented, highlighting the strengths and weaknesses of the proposed solution to face the P-Band limited resolution, as well as issuing some recommendations for future research in this field.

Chapter 2
Synthetic Aperture RADAR imaging

Since the underlying principles and the main parameters of SAR systems and antenna theory play an essential role in the development of this thesis, an adequate discussion about them is presented in this chapter. Moreover, the principal steps of SAR processing are examined and the most common technique employed to focus a SAR image is illustrated. To conclude this chapter, also a brief explanation on how to extend the monostatic[3] Synthetic Aperture RADAR theory to the multi-static SAR configuration case is given.

2.1 SAR fundamentals

Firstly, it is important to say that the SAR systems fall into the category of active devices, since, like conventional RADARs, they transmit power in the form of signals and receive back the scattered echoes (also referred to as backscattered signals). Indeed, a Synthetic Aperture RADAR is an observation system based on transmission and reception of frequency modulated microwave signals. Mounted on a moving platform, usually an aircraft or a satellite, it features the benefits of a RADAR with an antenna array, without the need of actually carrying one, allowing in this way to save weight (and thus to save money) and to avoid the problems associated to the transport of a huge array.

Another fundamental notion is that the spatial resolution of RADAR data is directly related to the ratio of the sensor wavelength to the length of the sensors' antenna, therefore for a given wavelength, the longer the antenna, the higher the spatial resolution. For instance, for a satellite in space operating at a wavelength of about 5 cm (C-band RADAR), in order to get a spatial resolution of 10 m, it would be needed a RADAR antenna longer than 4 km [16]. Obviously, an antenna of that size is not feasible, hence engineers have come up with a clever workaround: the synthetic aperture. According to this concept, a sequence of coherent acquisitions, made from subsequent trajectory positions from a real shorter antenna, are combined to simulate a dramatically larger antenna, thus providing higher resolution data.

To go into details, in a SAR system all the backscattered signals at every sample τ_n along the path are collected and, after having employed a matched filter at the receiver (see Section 2.2), each filtered signal s_{rc} is put in sequence. This is how the so-called raw data image (or raw data matrix) is generated, as it can be appreciated by looking at the scheme in Figure 2.1.

[3] The signal is transmitted and received by the same antenna.

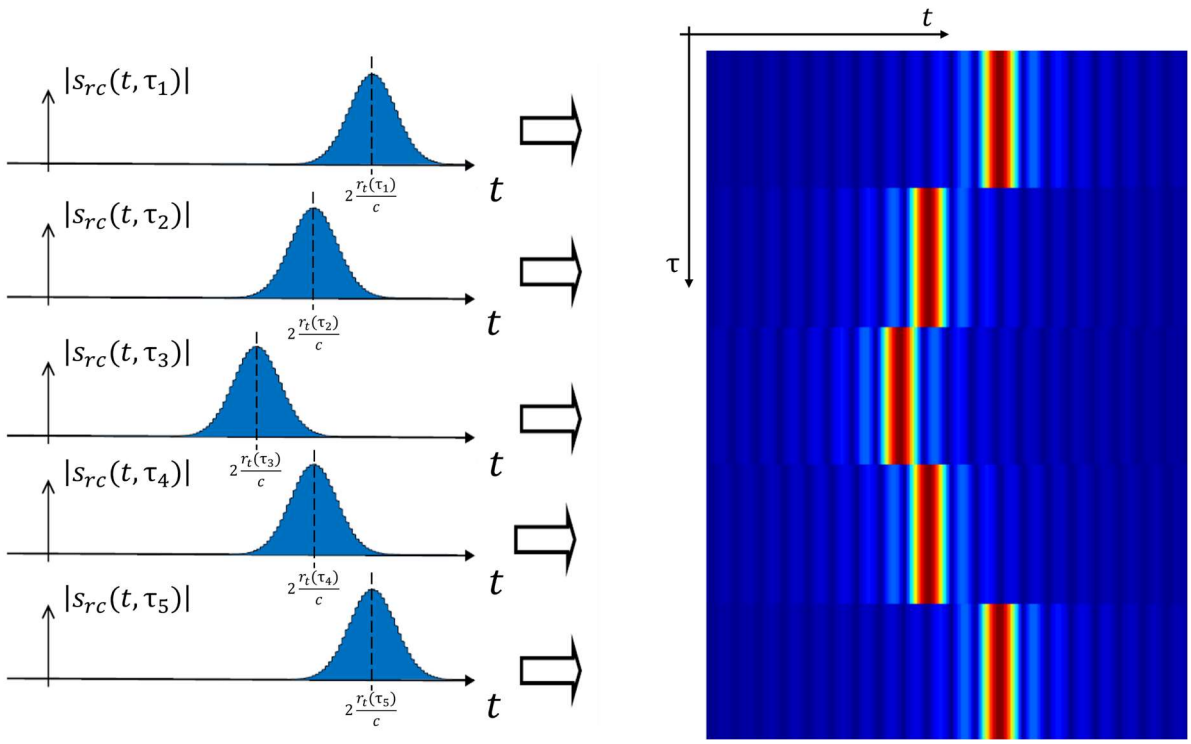

Figure 2.1: Raw data matrix construction for a point target

In this last image t stands for fast time, measured in $[s]$, which is the conventional time axis where the received pulse delay is measured, while τ, measured in samples, denotes the so-called slow time. The latter corresponds to the time at which the antenna is operated, thus, without any approximation, it can be read as the antenna position along the satellite orbit. Furthermore, it has to be noticed that in Figure 2.1 the blue picks are indicative of the target[4] position with respect to the SAR, at each time the antenna is operated. These picks appear to move on the fast time axis according to the delay at which the backscattered signals reach the SAR antenna but, at this purpose, it is better to clarify that these position differences in Figure 2.1 have been exaggerated for illustrative purposes.

With the presented technique the SAR simulate the presence of a very long antenna array deployed along the flight path, by exploiting a basic principle: each coherent acquisition of a signal along the trajectory is treated just like a signal recorded by a single element of a conventional antenna array [17]. This mechanism of collecting multiple looks of the same target from a wide range of azimuthal angles (see Figure 2.2) is what enables the SAR not only to locate the target in a 2D map but also to achieve impressively small along-track resolutions. However, nothing comes for free, in fact the price to pay for the increased spatial resolution is calculated in terms of processing burden and time.

The just mentioned collection of backscattered signals is sampled by filtering the trajectory with a moving window, so for each sample τ_n along the orbit there will be a starting and a final

[4] RADAR jargon to indicate the object which is hit by the transmitted signal.

antenna position: the distance between these two points is called synthetic aperture and it is shown in Figure 2.2, denoted with A_s.

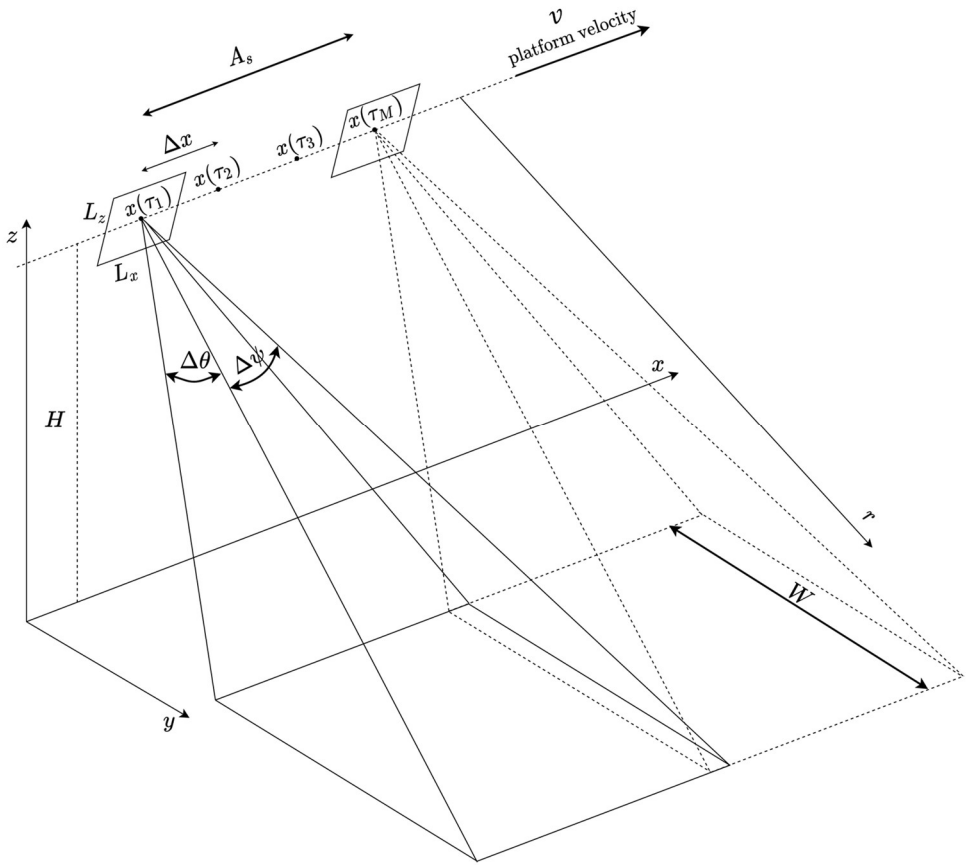

Figure 2.2: Scheme of a side-looking monostatic SAR

In this last figure it is sketched a monostatic side-looking SAR, together with some of its fundamental parameters. This system is illustrated while moving along the x direction which coincides with the satellite trajectory, indeed, in RADAR parlance, it is identified as azimuth or along-track direction since it corresponds to the direction of the platform velocity.

According to the last definition, in Figure 2.2, A_s is depicted as the distance between two different positions on the orbit (τ_1 and τ_M) thus, in the first place, the synthetic aperture can be simply expressed as:

$$A_s = x(\tau_M) - x(\tau_1) \tag{2.1}$$

where τ has been used as a numerical index for the current trajectory sample being evaluated. As it can be understood from this last equation the synthetic aperture has not a fixed length (τ_M is a generic position), in fact it can be expressed also as a function of range and azimuth beamwidth processed $\Delta\psi_{processed}$ through the following relation:

$$A_s = \Delta\psi_{processed} \cdot r \tag{2.2}$$

where $\Delta\psi_{processed}$ can be either a portion or the whole angular aperture in the azimuth direction $\Delta\psi$ (see Figure 2.2). On the other hand, in RADAR jargon, the distance r (depicted in Figure 2.2, too) is called slant range, even if it is often simply referred to as range.

Nevertheless, it is better to point out that, even if A_s does not have a fixed length, for spaceborne systems, it is usually chosen as the maximum distance the antenna can travel while still keeping in view all the targets placed at the minimum range of interest, which in SAR parlance corresponds to process the maximum synthetic aperture.

Indeed, considering the maximum synthetic aperture, A_s can be also calculated as:

$$A_{s\,max} = \frac{\lambda}{L_x} r_{max} \tag{2.3}$$

where L_x is the antenna dimension in the along-track direction (as it can be appreciated in Figure 2.2), r_{max} is the maximum slant range distance for the system and λ is the signal wavelength.

In addition, it is better to highlight that if on one hand the slow time can be read as the sensor position, it is also true that to pass from the fast time to the slant range just one simple computation is needed, namely:

$$t = 2\frac{r}{c} \tag{2.4}$$

Therefore, it is clear that expressing the SAR acquired data as in Figure 2.1 or within a r,x frame it is perfectly equivalent.

Moreover, it is necessary to point out that, in the RADAR jargon, not only the x direction has a peculiar name but also the y and z ones. In fact, the y direction is also known as ground range or across-track direction while the z one is often called elevation, and both of them are clearly depicted in Figure 2.2. From the latter it can be also appreciated that the swath along y, namely the width of the antenna footprint on the ground along y, is labelled as W. This last parameter is also called ground swath and can be easily computed as:

$$W = y_{max} - y_{min} \tag{2.5}$$

where y_{max} and y_{min} can be evaluated by means of the following straightforward relations:

$$y_{max} = \sqrt{{r_{max}}^2 - H^2} \tag{2.6}$$

$$y_{min} = \sqrt{{r_{min}}^2 - H^2} \tag{2.7}$$

in which H is the orbital height while r_{max} indicates the maximum slant range distance and r_{min} the minimum one.

To make the concept clearer in Figure 2.3 it is sketched the front view of a side-looking SAR like the one shown in Figure 2.2.

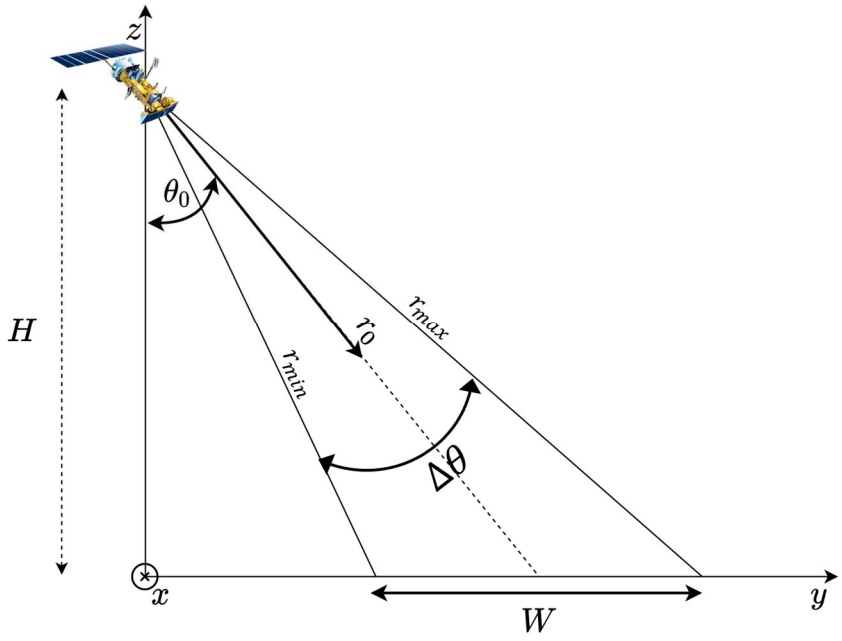

Figure 2.3: SAR frontal view

In this last image r_0 indicates the slant range correspondent to θ_0, the pointing angle in elevation, which is defined as the central angle within the elevation beamwidth $\Delta\theta$ (also illustrated in Figure 2.2).

The two antenna beamwidths illustrated in the last two figures can be computed as:

$$\Delta\psi \cong k\frac{\lambda}{L_x} \tag{2.8}$$

$$\Delta\theta \cong h\frac{\lambda}{L_z} \tag{2.9}$$

where L_z is the antenna dimension in the elevation direction. These relations arise from the antenna theory, in which a dependence between real antenna dimensions and angular beamwidth can be inferred, and k and h are positive coefficients different for each antenna type, thus have to be chosen accordingly to the shape of the employed antenna (for example $k = h = 1.22$ for parabolic antennas and $k = h = 1$ for planar ones) [18].

At this point, it is worth noticing that the choice of showing the scheme of a specific SAR configuration, namely a side-looking SAR, in Figure 2.2 and 2.3 is motivated by the fact that it is the kind of SAR system simulated in this thesis, due to its remarkable advantages. Indeed, looking towards the ground with a certain pointing angle in elevation, namely θ_0, allows the

SAR system to avoid left-or-right ambiguities that would arise if the sensor were pointed at the nadir[5]. Indeed, an inherent consequence of the pulsed operation of the SAR is that the echoes of subsequent transmitted pulses, propagating back from the nadir, come back at the RADAR simultaneously with the echoes of interest.

Although the RADAR antenna is designed to limit the energy transmitted to and received from the nadir direction, due to the smaller range and the specific characteristics of the scattering process (specular reflection), the nadir echo may be even stronger than the desired one and may therefore significantly affect the quality of the SAR image [19]. In particular, the nadir echo appears as a bright stripe in the final image as it is clearly visible in Figure 2.4.

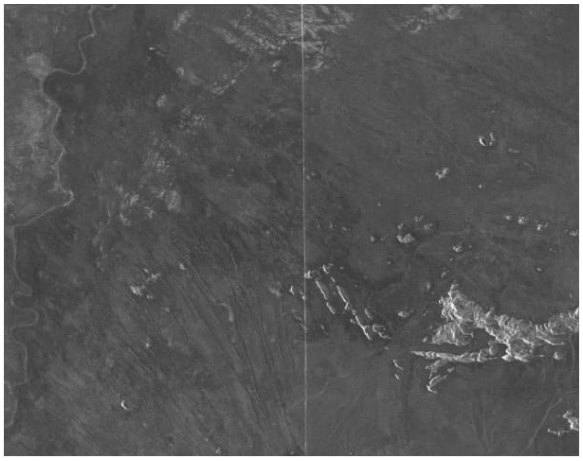

Figure 2.4: Example of nadir echo in a SAR image

In this last figure a real SAR image, acquired by the TerraSAR-X satellite over Australia, is shown and the horizontal and vertical axes represent slant range and azimuth, respectively.

Moreover, having mentioned the fact that a conventional SAR system operates by means of electromagnetic pulses, it is important to discuss the following two parameters: the sampling step and the interval between two adjacent pulses.

Having said that the SAR emits one pulse per platform station (i.e., one pulse for each τ_n), the trajectory sampling step Δx, that in a classical antenna array corresponds to the physical distance between the array elements, can be linked to the velocity of the platform through the following relation:

$$\Delta x = PRI \cdot v \tag{2.10}$$

in which PRI stands for Pulse Repetition Interval, that is measured in $[s]$ and represents the time interval between two adjacent pulses, while v is the platform speed in $[m/s]$, which changes according to the orbital altitude H. In addition, it has to be noticed that the PRI is also

[5] The point with the closest distance to the RADAR.

the inverse of another important parameter called Pulse Repetition Frequency (PRF), measured in hertz [Hz].

Having described the PRI, it is fundamental to state the SAR trade-off. Indeed, according to the latter it is not possible to achieve at the same time an arbitrary large swath and an arbitrary fine along-track resolution, which leads to the following upper and lower bounds for the PRI value selection:

$$PRI > \frac{2(r_{max} - r_{min})}{c} \tag{2.11}$$

$$PRI < \frac{\lambda}{2\, v\, \Delta\psi} \tag{2.12}$$

The just outlined limits are vital to reject the ambiguities, in particular the upper bound is needed to avoid range ambiguities while the lower bound to escape along-track ambiguities. The non-fulfilment of both these requirements leads to an incorrect imaging.

2.1.1 SAR resolution

At this point, it is fundamental to introduce the concept of resolution. The resolution is defined as the minimum distance at which two targets can be imaged separately [20]. By looking at the scheme presented in Figure 2.2 it is evident that, for a SAR system, the slant range and azimuth resolutions, indicated with ρ_r and ρ_x respectively, are the two fundamental resolutions to take into account. They can be computed as:

$$\rho_r = \frac{c}{2B} \tag{2.13}$$

$$\rho_x = \frac{\lambda}{2A_s} r_{ref} \tag{2.14}$$

in which c is the speed of the light in the vacuum, B is the signal bandwidth and r_{ref} is the reference slant range at which has been computed the synthetic aperture. Having defined the azimuth resolution, it is worth mentioning that the PRI upper bound, stated in Equation (2.12), can be simplified, if the maximum synthetic aperture is processed, by exploiting Equation (2.8) and (2.14), becoming:

$$PRI < \frac{\lambda}{2\, v\, \Delta\psi} \cong \frac{\rho_x}{v} \tag{2.15}$$

The slant range resolution, which almost always is abbreviated as range resolution, can be also projected on the across-track direction, namely y, giving as a result the ground range resolution ρ_y:

$$\rho_y = \frac{\rho_r}{\sin\theta} \tag{2.16}$$

where θ is an arbitrary elevation angle in the beamwidth and any eventual terrain slope has been neglected. To make these last definitions clearer, an illustration highlighting the SAR resolutions is presented in Figure 2.5.

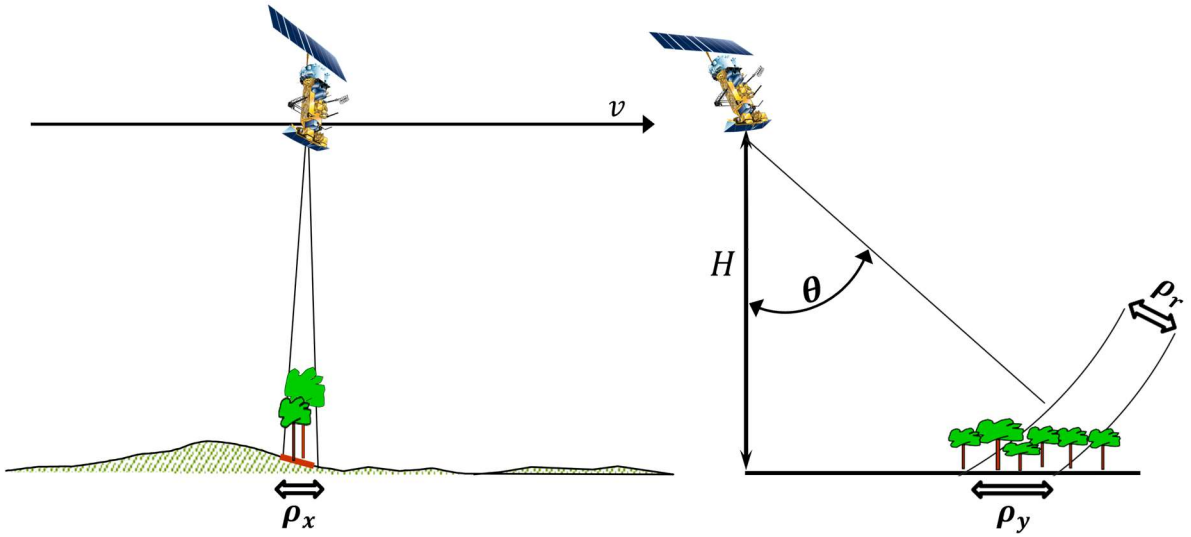

Figure 2.5: SAR resolutions

At this point the essential concept of resolution cell can be introduced: all targets contributing to the same image pixels[6] are bound to lie in the region of space belonging to the yz plane, centered on the platform trajectory and having widths given by ρ_x and ρ_r (and ρ_y consequently) as illustrated in Figure 2.6.

[6] The SAR pixel is defined as the integral of all contributions within the resolution cell.

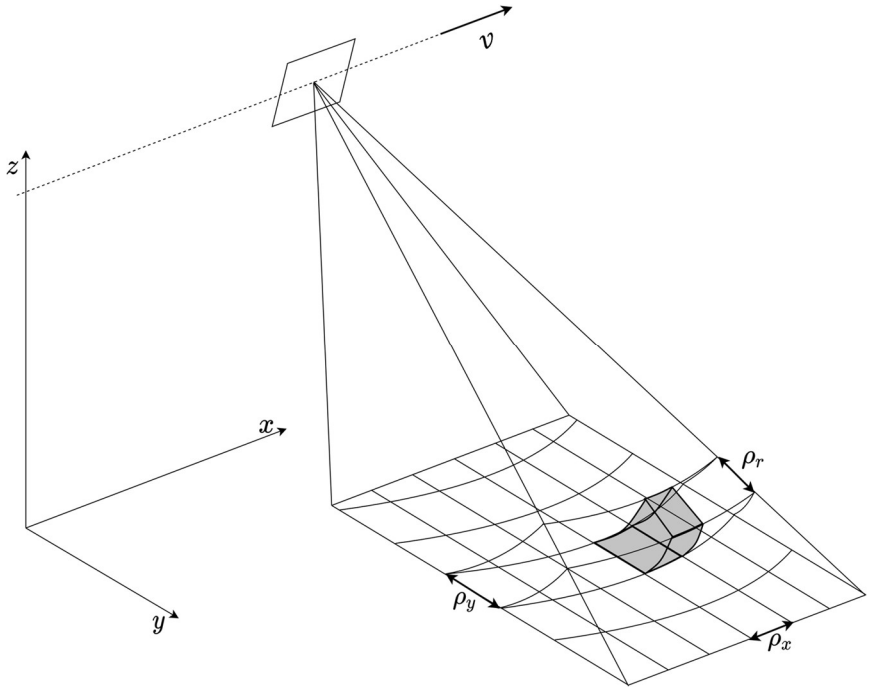

Figure 2.6: Resolution cell of a monostatic SAR

To be precise the overall resolution cell has the shape shown in Figure 2.7, but of course the beamwidth in elevation $\Delta\theta$ cuts the peculiar ring-shape, giving as a result the 3D cell shown in Figure 2.6.

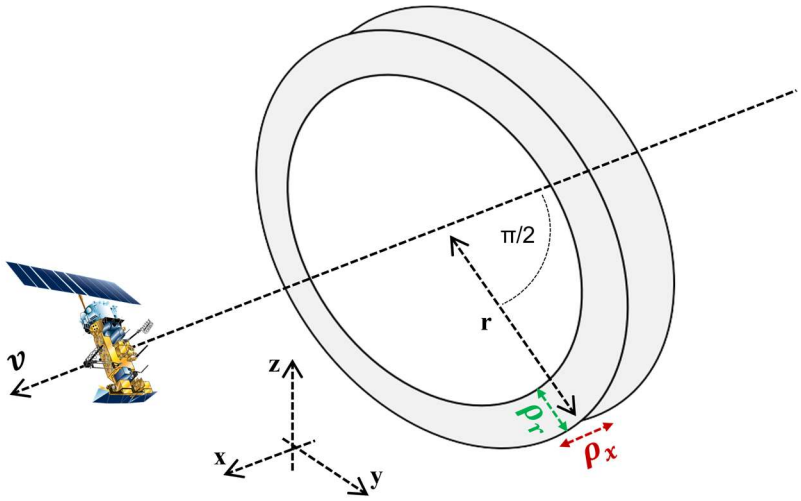

Figure 2.7: Resolution ring of a monostatic SAR

If two targets fall into two different resolution cells they are seen by the SAR system as separate, on the contrary, if they are part of the same resolution cell, the RADAR is not capable of imaging them as two different scatterers because the system resolution is too coarse to distinguish the two targets.

Moreover, it is interesting to notice that also Equation (2.14) can be simplified under the hypothesis of processing the maximum synthetic aperture allowed by the physical antenna, which is not always the case for airborne SARs but it is almost always the case for spaceborne systems. In this peculiar condition the (2.14) becomes:

$$\rho_x = \frac{L_x}{2} \tag{2.17}$$

On the other hand, it is clear that the range resolution ρ_r depends only on the system bandwidth B and it has to be pointed out that Equation (2.13) originates from the range compression of the received signal, i.e. the convolution of each acquisition along the flight path with the matched filter (which is explained in Section 2.2). From Equation (2.13), it is also easy to see that the wider the bandwidth of the signal the finer ρ_r results to be.

In light of what is discussed in Chapter 1 and by looking at Equation (2.13), it is clear why P-Band spaceborne SAR systems have not been employed in past missions, despite their evident advantages. However, over in the next chapters of this thesis, it is proven that, even when the bandwidth is as small as in P-Band, there is still a technique that can be exploited to improve range resolution.

Furthermore, again from Equation (2.13), it can be understood why the chirp signal, defined through the following mathematical expression, is so popular among the SAR systems.

$$g(t) = rect\left(\frac{t}{T}\right) exp(j\pi\alpha t^2) \tag{2.18}$$

Where α is called chirp rate and T is the chirp duration, while the wording $rect$ represents the rectangular function. Nevertheless, from the SAR point of view, the most important characteristic is that this signal is characterized by a bandwidth that varies linearly with its duration according to:

$$B = \alpha\, T \tag{2.19}$$

From the last equation it can be noticed that, if the α is not given as a constraint, the use of the chirp allows to compute T and B independently one from the other, thus each one from a different requirement, which is an important additional degree of freedom in a SAR design. As an example, it is possible that a RADAR engineer has the range resolution and the duty cycle as constraints, so from ρ_r it is possible to compute the bandwidth (just inverting the Equation (2.13)), while from the knowledge of the duty cycle δ and the proper choice of the PRI it is easy to evaluate the signal duration as:

$$T = \delta\, PRI \tag{2.20}$$

where the duty cycle, usually expressed as a percentage, is another important parameter which expresses the percentage of time a digital signal is on over a PRI.

Furthermore, having a long T allows the system to collect a good amount of energy by receiving lower power for more time, which is far better than receiving higher power for a short amount of time, since a too high pick power can damage the electronic components. For these reasons the chirp is the most used signal in SAR applications: it allows to have a long signal without renouncing to a wide bandwidth, thus to a fine range resolution (see Equation 2.13).

2.1.2 Antenna gain and radiation pattern

Other two very important features, not only for SAR systems but for all the devices equipped with antennas, are the gain G and the antenna pattern f. The first, usually expressed in $[dB]$, can be computed as:

$$G = \eta \frac{4\pi}{\Delta\theta \, \Delta\psi} \tag{2.21}$$

where η is the antenna efficiency. For the sake of completeness, it is worth mentioning also another parameter which is possible to evaluate once having computed the gain: the antenna effective or equivalent area A_e.

The latter is measured in $[m^2]$ and is evaluated as:

$$A_e = G \frac{\lambda^2}{4\pi} \tag{2.22}$$

This equivalent area, also known as effective antenna aperture, is defined as the ratio of the received power available at the terminals of an antenna to the power per unit area in the incident wave [20].

On the other hand, the antenna gain indicates the extent to which the field is focused along a specific direction, that is the direction of pointing. In fact, it shows how the antenna is capable of radiating more in a specific direction, compared to a theoretical isotropic antenna, assuming that both antennas are fed with the same power [18]. It is a theoretical value because an isotropic antenna does not exist, since an antenna which radiates the same power in all the directions cannot be constructed. Thus, the gain value can be calculated or expressed in theoretical terms only, nevertheless it is extremely useful to quickly compare the directivity of two antennas.

Rigorously, as it can be understood by the above definition, an antenna has not just one gain, indeed it can be computed a gain for each direction, but, most of the times and also in this dissertation, when discussing about antenna gain it refers to the gain evaluated along the boresight direction. The latter is the axis of maximum gain (or equivalently maximum radiated power) of a directional antenna and, almost always, it coincides with the axis of symmetry of

the antenna itself. Moreover, by looking at Equation (2.21) it is evident that a high gain corresponds to a very directive antenna, as it is desirable for spaceborne antennas. In fact, the narrower the beamwidths (so the smaller the product $\Delta\theta \cdot \Delta\psi$ is) the higher the antenna gain, thus it is intuitive that a spaceborne antenna needs to have a huge capability to direct the radiation in a specific direction because of its distance from the targets. Indeed, the goal of spaceborne applications is to have very directive antennas (orders of magnitude higher with respect to terrestrial ones), so that the less possible transmitted power is lost in undesired directions, being the power transmission from those distances deeply expensive.

Talking about antenna directivity, it is essential to discuss the fundamental concept of antenna radiation pattern, which is usually indicated with f. Indeed, as it can be appreciated in Chapter 4, the antenna pattern affects multiple aspects of the proposed SAR constellation designs, therefore a clarification regarding its fundamentals is necessary to fully understand the f plots and the details that are given in Chapter 4.

The antenna radiation pattern represents the antenna radiation properties as a function of space or equivalently, it describes how the antenna radiates and receive energy, as it can be appreciated by looking at Figure 2.8.

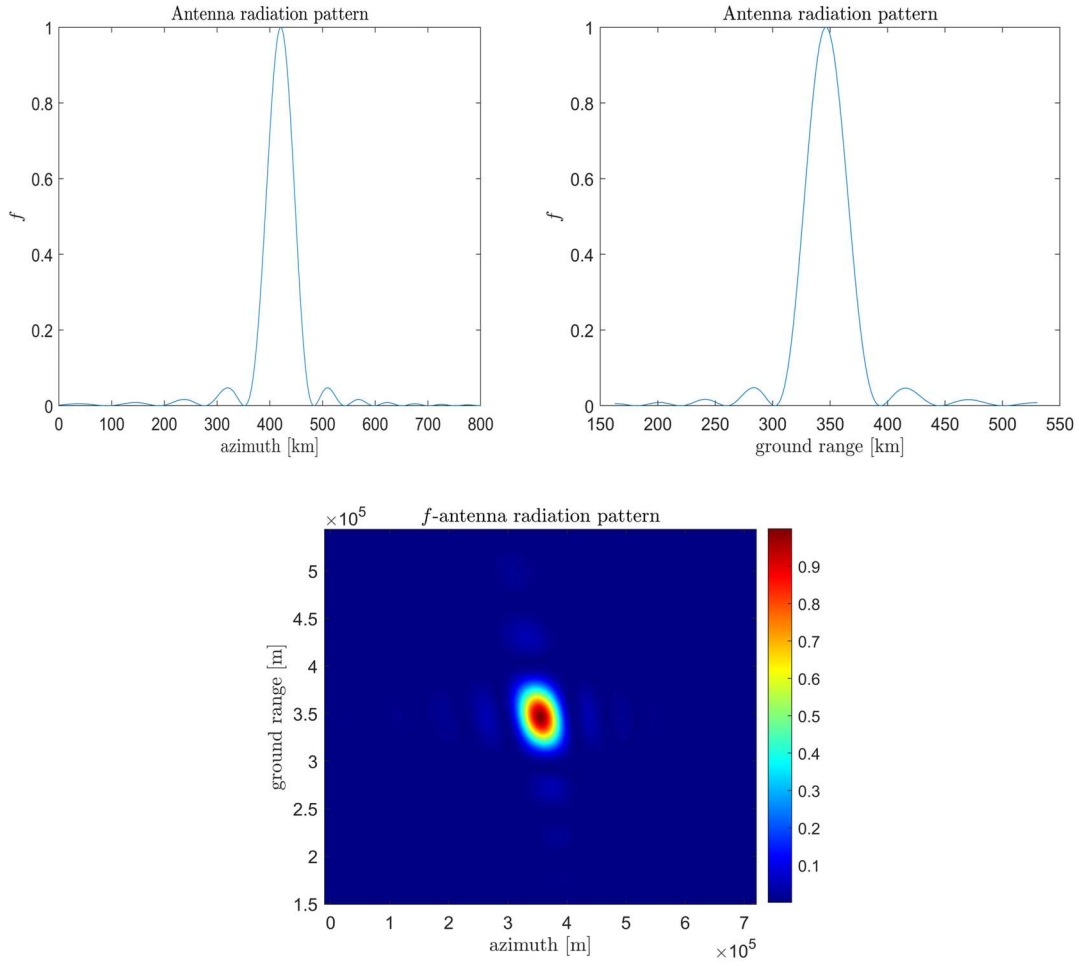

Figure 2.8: Antenna pattern example

The three plots in this last figure represent the same antenna pattern, in particular the two top plots are the 1D representation of the 2D pattern (lower plot of Figure 2.8), and they are drawn from one of the project simulations. They are presented in the x, y frame because in the SAR field, it is common to study the antenna pattern in the azimuth and ground range directions to clearly visualize the antenna footprint on ground. In this way f becomes function of the azimuth angle ψ and of the elevation angle θ.

At this purpose, it has to be pointed out that an antenna pattern can be simulated through different type of functions, according to the desired shape, nevertheless the function that resembles more the real pattern of the antennas is the $sinc$ (obviously written as a particular function of ψ and θ), which in fact is the one employed for the presented fleet designs and to obtain the plots in Figure 2.8.

From the latter it is also clear that, even if by definition an antenna radiates energy in all directions, at least to some extent, the more it is directive the more the energy is addressed mostly in specific directions highlighted by the antenna pattern, whose lobes dimensions depend on the antenna gain. In fact, the higher the directivity, thus the antenna gain, the narrower the pics shown in the previous plots are, because the beamwidths $\Delta\theta$ and $\Delta\psi$ become smaller. Furthermore, from Figure 2.8 it can also be noticed that the antenna pattern is usually normalized to 1, but of course the ground range and azimuth axes values, visible in these last plots, are peculiar of the presented project simulations as well as the $sinc$ shape of the pattern.

Nevertheless, from these plots they can be identified the main lobe and also some sidelobes, which have always to be carefully considered in the antenna design. Any given antenna pattern has lobes (whose extent varies from case to case) which are any part of the pattern that is surrounded by regions of relatively weaker radiation. Therefore, any part of the pattern that "sticks out" is defined as a lobe and the names of the various types of lobes are somewhat self-explanatory. Indeed, the main lobe in Figure 2.8 is the highest one in the 1D plots, which corresponds to the high intensity region in the 2D image, and it is centred around the boresight direction. The latter coincides with the antenna pointing direction, identified by the aforementioned pointing in elevation and also by the pointing in the along-track direction (that is defined in Section 2.3).

2.1.3 RADAR equation

At this point all the elements needed to compute the received power, for a generic remote sensing instrument, have been presented. The received power P_{rx} is computed by means of the so-called RADAR equation, which is the main equation in the RADAR field, since it allows to evaluate the amount of power scattered back by the targets that actually returns to the antenna. Indeed, the power intensity at the receiver is a vital information because it makes the difference between acquisition and no acquisition and also drives the performance of the system through the Signal-to-Noise Ratio or equivalently, the Noise Equivalent Sigma Zero (discussed in the following subsection).

Moreover, it has to be noticed that the RADAR equation in this subsection is presented by considering a bistatic configuration, because, as it is clarified in Section 2.3, the SAR systems designed for this thesis work in couples, thus according to the bistatic scheme. The latter, indicates a system employing one antenna in transmission and a different one in reception. In any case, always by using the following equations, it is also possible to evaluate the received power for the monostatic configuration (which can be easily seen as a peculiar case of the bistatic one) just by referring all the parameters to the same antenna, since in that case there is no distinction between the antenna in transmission and in reception.

To obtain the RADAR equation the first step is to compute the incident power density at the target, measured in $[W/m^2]$ and usually identified with S_i, in the following way:

$$S_i = \frac{P_{tx}}{4\pi\, {r_{tx}}^2} G_{tx}\, f_{tx} \tag{2.23}$$

where P_{tx} is always the transmitted power and all the parameters with subscript tx are related to the transmitting antenna, while the ones with rx are computed for the receiving one.

Then it is necessary to calculate the RADAR Cross Section (RCS) which is needed to evaluate the scattered power density S_s. The RCS expressed in $[m^2]$ is a property of the target, in fact it is also called electromagnetic signature of the object, and it measures how detectable an object is by RADAR systems. The RCS is also defined as a quantity that can be measured through a single RADAR survey and a larger RCS indicates that an object is more easily detected. Moreover, the RCS is independent of target distance from the antenna while varies according to transmitter and receiver angular position relative to the target and with the used frequency. In fact, the RCS depends on the size of the target relative to the wavelength of the illuminating RADAR signal, because it influences the amount of power scattered by the target. Of course, each target reflects back to the source only a limited amount of transmitted energy, that also depends on the material with which it is made. Therefore, it is clear that the RCS for real targets is exactly a directional radiation pattern, like the one previously defined for antennas [18]. It is also interesting to notice that the RCS of a target, pointed towards the RADAR, is almost always much larger than the physical area of the target, with the remarkable exception of spheres in the optical regime (radius $\gg \lambda$), in which cases the RCS is equal to their geometrical area.

In the following equation it is presented the formula to compute the RADAR Cross Section of all the targets within the resolution cell at position x, y or equivalently x, y.

$$RCS = \sigma_0\, \rho_x\, \rho_y \tag{2.24}$$

Where σ^0, measured in $[dB]$, is called backscatter coefficient. The latter is a property of the pointing angle in elevation and of the observed distributed target, which is the environment the SAR is looking at.

At this point the scattered power density at the receiving antenna, indicated with S_s and measured in $[W/m^2]$, can be computed as illustrated in Equation (2.25).

$$S_s = \frac{S_i \, RCS}{4\pi \, {r_{rx}}^2} \tag{2.25}$$

Finally, assembling together all the just described parameters, it is possible to construct the RADAR equation to compute the received power in $[W]$ as follows.

$$P_{rx} = S_s \, A_{e_{rx}} \, f_{rx} = \frac{P_{tx} \, G_{tx} \, Ae_{rx} \, f_{rx} \, f_{tx} \, RCS}{(4\pi)^2 \, {r_{tx}}^2 \, {r_{rx}}^2} \tag{2.26}$$

All the just discussed concepts can be graphically visualized by looking at Figure 2.9 in which it is shown the transmission-reception scheme of a bistatic couple.

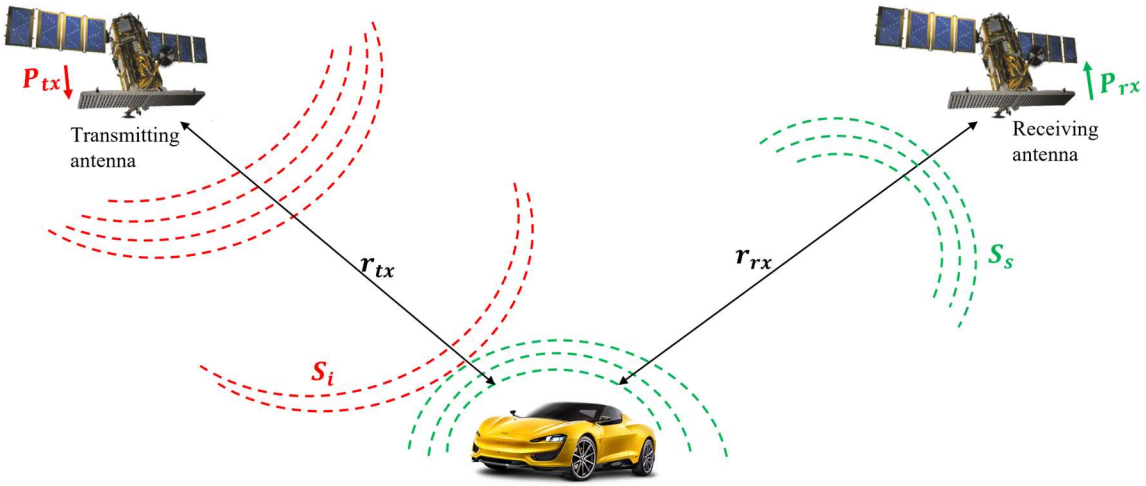

Figure 2.9: Transmission-reception scheme of a bistatic couple

2.1.4 SNR and NESZ

To conclude this section about the SAR fundamentals, it is necessary to present the aforementioned Signal-to-Noise Ratio (SNR) and the Noise Equivalent Sigma Zero (NESZ), which can be seen as two sides of the same coin and are both very used parameters to evaluate the performance of a SAR system. In fact, engineers responsible for the design of SAR systems have always to take them into account, since they are among the most important constraints that are imposed by the costumers, regarding the performance of the concerned SAR.

The SNR and NESZ are almost always expressed in $[dB]$ and they are strictly related one to the other, in particular they are inversely proportional according to the formula:

$$SNR = \frac{\sigma^0}{\sigma^{NESZ}} \tag{2.27}$$

where σ^{NESZ} is the usual way to indicate the NESZ. The SNR is a measure that compares the level of the desired signal to the level of background noise, as it is clear from the following equation:

$$SNR = \frac{P_{rx}\, N_\tau\, T_g}{N_0} \tag{2.28}$$

where P_{rx} is computed through the RADAR equation (see Subsection 2.1.3), T_g is the transmitted pulse duration (that coincides with T if a chirp signal is used), N_0 is the noise power spectral density in $[W/Hz]$ and N_τ is the effective number of pulses within the synthetic aperture. Moreover, Equation (2.28) is specific for the Signal-to-Noise Ratio computation after the focusing procedure and it is presented because it is the most meaningful and used one since it gives the total energy collected ($E_{rx} = P_{rx} \cdot T_g$) across N_τ pulses compared to the noise power. Of course, the higher the value of the SNR the higher are the performance of the SAR system, since the received signal results to be easily distinguishable from the noise floor, drastically decreasing the risk of reading the noise instead of the signal at the receiver. In fact, the signal received from a device with a high SNR can be easily cleaned. As always nothing comes for free, indeed, to reach higher Signal-to-Noise Ratio values the most immediate and easy solution is to transmit a higher power, which is both expensive and heavy to be done in space. Furthermore, since they are needed for the SNR evaluation, it is important to show how to compute the N_τ and the N_0. The first is computed by means of the following equation:

$$N_\tau = \frac{A_s}{v\, PRI} \tag{2.29}$$

while the N_0 is evaluated as:

$$N_0 = K\, T_{sys} \tag{2.30}$$

where K is the Boltzmann constant ($K = 1.3807 \times 10^{-2}\ \ [J/K]$) and T_{sys} is the system temperature. The latter is computed knowing the antenna temperature T_{ant} in $[K]$ and T_{rx}, the noise temperature of the receiver referred to the antenna terminals in $[K]$, as:

$$T_{sys} = T_{ant} + T_{rx} \tag{2.31}$$

where in turn the two addends are computed as:

$$T_{ant} = \eta\, T_{scene} + (1-\eta)\, T_{0,ant}$$
$$T_{rx} = (F_{lin} - 1)\, T_{0,ref} \tag{2.32}$$

where T_{scene} is the is brightness temperature of external thermal sources[7], η is the antenna efficiency (accounting for losses), $T_{0,ant}$ is the physical antenna temperature and F_{lin} is a parameter called noise factor, which is called noise figure F when is expressed in $[dB]$ instead of linear units. For active systems (like a SAR), it is customary to express the noise factor defined with respect to a fixed reference temperature $T_{0,ref} = 290\ K$ indeed, although the noise factor does vary with the physical temperature of the receiver, it is always referred to that reference temperature.

On the other hand, the σ^{NESZ} can be computed or from Equation (2.27) or by inverting the formula for the transmitted power, as:

$$\sigma^{NESZ} = \frac{\sin(\theta)\, N_0 (4\pi r^2)^2}{\rho_x\, \rho_r\, N_\tau\, T_g\, P_{tx}\, G\, A_e\, f^2} \tag{2.33}$$

Since the SRN and the σ^{NESZ} are usually given as project constraints, they are normally computed in the whole ground swath, so for all the θ angles within the $\Delta\theta$, to check if the designed system meets the requirements, or in some cases they are only evaluated in the boresight direction, thus for $\theta = \theta_0$. Indeed, to develop the design the SAR fleets presented in Chapter 4, a specific constraint on the NESZ, coming from the Biomass mission, has been taken into account. Moreover, in the same chapter, the plots of the NESZ within the system ground swath are shown to assess the fleets performance. In this regard, being the NESZ inversely proportional to the SNR, a good system is characterized by a low NESZ values within the swath.

2.2 SAR processing

After the data acquisition, the SAR image is formed by means of digital processing techniques, which result into a high resolution two dimensional map of the imaged scene. In the following, the case of monostatic SAR imaging is discussed, however the exact same analysis applies to bistatic scenarios, too, provided that the appropriate ranges are used (see Section 2.3).

[7] It is the source of information for passive instruments, such as radiometers, but represents noise for RADAR systems.

2.2.1 Range compression

As mentioned in Section 2.1, the immediate approach to obtain a SAR image is: to collect signals s_{rx} at every sample τ_n along the path, then to use a matched filter at the receiver to recover high peak signal to noise ratio and finally to put each filtered signal in sequence creating the raw data matrix. A real example of the latter can be appreciated in Figure 2.10.

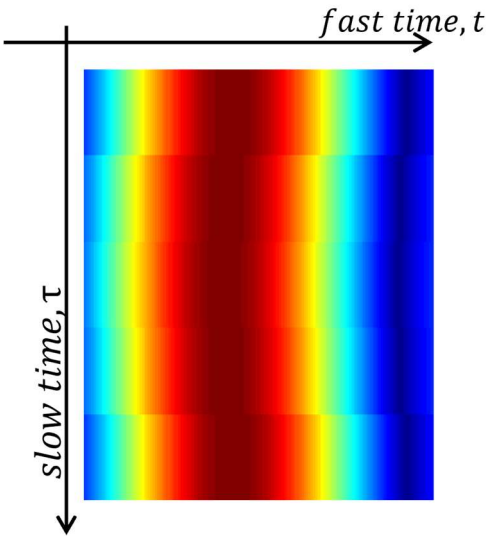

Figure 2.10: Raw data matrix example for a point target

In this last figure, the plots of each filtered signal along the fast time axis, which compose the presented raw data matrix, have not been reported like it was done for Figure 2.1. Nevertheless, by looking at Figure 2.10 it is clear that here the picks are much more aligned with each other than before, meaning that their positions' difference on the fast time axis are now far less pronounced. The picks' translation on the t axis is a physical phenomenon due to the fact that the antenna is sliding along the trajectory, continuously changing its distance from the target, thus the backscattered echoes come back to the SAR with different delays. Nevertheless, this effect, that in RADAR jargon is called range migration, becomes a real issue when its amplitude happens to be greater than the inverse of the system bandwidth, because it forces to use very time-consuming and highly computational burdened focusing algorithm (deeply explained in the following subsection). The range migration can be considered negligible only for systems which operate with small bandwidth and/or small antenna aperture, as it can be in the case of an antenna array but almost never in the case of a spaceborne SAR. For instance, in the raw data matrix presented in Figure 2.1 the range migration was huge, nonetheless that image was used just to make immediately understandable how the SAR acquisition works.

Moving forward, if the signals are expressed in their complex baseband representation, the collection of unfiltered received data consists of a 2D grid of complex values that can be written as:

$$D(t,\tau) = s_{rx}(t,\tau) \tag{2.34}$$

For a point target of complex reflectivity A_t, the $D(t,\tau)$ data matrix takes the form:

$$D(t,\tau) = A_t g\left(t - 2\frac{r_t(\tau)}{c}\right) exp\left(-j\frac{4\pi}{\lambda} r_t(\tau)\right) \tag{2.35}$$

where g denotes the transmitted waveform (often it is a chirp) and j is the imaginary unit. The dependency of the target slant range distance r_t on the slow time τ can be explicitly expressed as follows:

$$r_t(\tau) = \sqrt{(x(\tau) - x_t)^2 + (y(\tau) - y_t)^2 + (z(\tau) - z_t)^2} \tag{2.36}$$

in which x, y and z and x_t, y_t and z_t are the SAR and the point target coordinates respectively, taking into account, in this way, also the possibility of a non-linear SAR trajectory.

For multiple targets, linear superposition can be exploited, therefore the resulting image will just be the sum of all the individual contributions from each target. In the limit case of a distributed target, this sum is converted into an integral, resulting in:

$$D(t,\tau) = \int_V A_t(\boldsymbol{r}) g\left(t - 2\frac{r_t(\tau,\boldsymbol{r})}{c}\right) exp\left(-j\frac{4\pi}{\lambda} r_t(\tau,\boldsymbol{r})\right) d\boldsymbol{r} \tag{2.37}$$

in which the integration domain V is the volume of the distributed target, that can be treated as a collection of infinitesimal point targets.

Then, the matched filtering procedure can be applied to maximize the SNR and exploit the full resolution provided by the signal bandwidth B. The matched filtering, also referred to as cross-correlation or range compression, is the process of optimal filtering the signal that is coherently scattered by the targets and received by the SAR. The range-compression is achieved by convolution of each RADAR echo with the transmitted waveform, complex conjugate and time reversed. The result of the convolution can be approximated as:

$$s_{rc}(t) = g(t) * g^*(-t) \approx sinc(tB) \tag{2.38}$$

where it can be demonstrated that $g^*(-t)$, which is the complex conjugate and time reversed waveform, is the optimal filter because it makes sure that the received signal filtered in this way, produces a pick at the delay position, thus for $t = 2\frac{r_t(\tau)}{c}$.

By substituting $g(t)$ with $s_{rc}(t)$ in Equation (2.35) the approximated equation of a SAR range compressed data matrix D_{rc} is obtained as:

$$D_{rc}(t,\tau) = A_t sinc\left(\left(t - 2\frac{r_t(\tau)}{c}\right)B\right) exp\left(-j\frac{4\pi}{\lambda}r_t(\tau)\right) \tag{2.39}$$

Doing the same for Equation (2.37), leads to:

$$D_{rc}(t,\tau) = \int_V A_t(\boldsymbol{r}) sinc\left(\left(t - 2\frac{r_t(\tau,\boldsymbol{r})}{c}\right)B\right) exp\left(-j\frac{4\pi}{\lambda}r_t(\tau,\boldsymbol{r})\right) d\boldsymbol{r} \tag{2.40}$$

The absolute value of the range compressed data matrix, for a single point target (whose position in space is indicated by the white circle) has the shape presented in Figure 2.11.

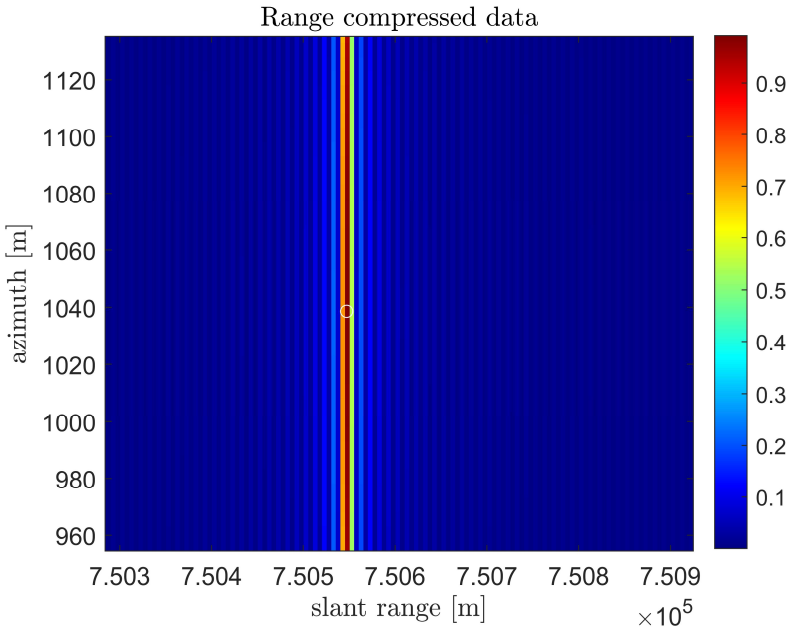

Figure 2.11: Range compressed data matrix for a point target

It this last figure the D_{rc} plot is given as a function of slant range and azimuth, instead of the fast time and the slow time. Nevertheless, as explained in Section 2.1 the fast time and the slant range are related by Equation (2.4) while the slow time coincides with the system azimuthal position along the orbit. Indeed, having the D_{rc} as a function of r and x, which is the typical SAR reference frame, makes it faster and clearer to be read with respect to the t and τ frame, since it allows to visualize the spatial position of the target.

2.2.2 Azimuth compression

Nevertheless, the range compressed image displays a scene correctly resized only in range, indeed, to transform the raw SAR signal data into a useful image it is required an additional step, known as focusing. In fact, from Figure 2.11, it is evident that also a compression along the azimuth direction is needed, since the target has been observed at a wide variety of angles, leading to the spreading of the received signal along the slow time direction.

In this regard, there is a huge variety of processing algorithms to focus the image, some work under simplifying assumptions, some are slower but achieve considerably higher resolutions, while some others can be very fast (and as such are fit for real-time applications) but sacrifice some accuracy for the sake of computational speed. Being a deep discussion on the focusing techniques not pertinent to this work, in the following subsection it is detailed only the focusing algorithm that has been employed in this thesis.

2.3.2.1 Time Domain Back Projection (TDMA)

As said the azimuth compression might be performed using several available techniques. Just to give an example, one of the simplest would be focusing by employing the Discrete Fourier Transform (DFT), but this methodology can be correctly used only under two strong assumptions, i.e. negligible range migration and plane wavefront approximation.

When these two hypotheses do not hold anymore, as in the presented study, the gold standard for high-quality imaging is to implement the Time Domain Back Projection (TDBP). This algorithm is based on three main steps:

1. interpolation of the range compressed signal:

$$s_{rc}\left(t = 2\frac{r_t(\tau)}{c}, \tau\right)$$

2. phase rotation, so the multiplication of the signal by:

$$\exp\left(j\frac{4\pi}{\lambda}r_t(\tau)\right)$$

3. sum over all antennas in the case of an array or over all the positions along the orbit for a SAR.

The interpolation step allows to avoid a double integral over fast time and antenna position, for each pixel, bringing a great reduction of computational cost and time needed. In addition to further speed-up the computations in the TDBP algorithm, which in any case remains the most time-consuming procedure, a common procedure is to evaluate only the samples within the synthetic aperture, since it is useless to consider the ones that fall outside it. In this way only the contributing samples are used to compute the back-projected signal.

Moreover, it is better to highlight that a single antenna position, does not have any angular resolution capability, indeed it is sensitive only to the range, so it is the cumulative sum over all the antenna positions which gives rise to a constructive interference at the true target position only (destructing elsewhere), resulting in the focused image.

The great advantage of this algorithm is that it is exact, indeed no approximations about sensor trajectory or transmitted bandwidth are needed, nevertheless it is very computationally expensive. In fact, it costs significantly more, in terms of operations to be performed and time needed, with respect to many other available algorithms (i.e., DFT and 1D along-track compression).

In the end the final, focused image, can be approximated as two matched filters applied in series, an operation which outputs the following result in case of a single point target:

$$I(x,y) = A_t sinc\left(\frac{x-x_t}{\rho_x}\right) sinc\left(\frac{y-y_t}{\rho_y}\right) exp\left(-j\frac{4\pi}{\lambda}r_t\right) \tag{2.41}$$

while for distributed targets it becomes:

$$I(x,y) = \int_{A_c} A_t(x_t,y_t)\, sinc\left(\frac{x-x_t}{\rho_x}\right) sinc\left(\frac{y-y_t}{\rho_y}\right) exp\left(-j\frac{4\pi}{\lambda}r(x_t,y_t)\right) dx_t dy_t \tag{2.42}$$

where the integration domain A_c is the area of the SAR resolution cell along x and y, as shown in Figure 2.6. Of course, the image can be easily converted in the x, r reference frame instead that in the previously mentioned x, y frame, since the conversion between slant range and ground range is a simple matter of trigonometry as it can be clearly seen in Figure 2.3 and in Equation (2.16).

In Figure 2.12 it is shown the result of the TDBP focusing procedure, applied on the range compressed matrix presented in Figure 2.11, and also in this case the single point target is indicated through a white circle.

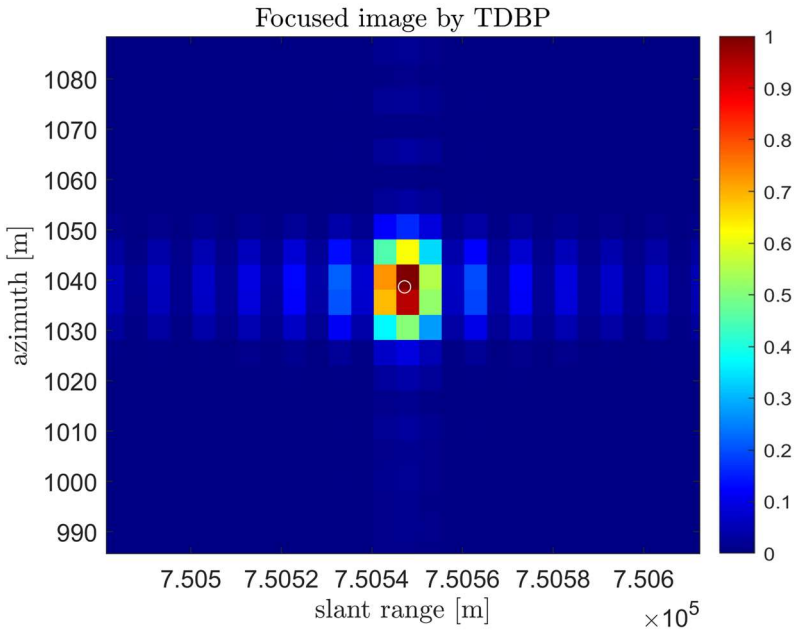

Figure 2.12: Focused image of a single point target

It has to be highlighted that the plots in Figure 2.11 and 2.12 have been obtained by simulating on *MATLAB* a monostatic SAR system flown at a realistic orbital height of $650\ km$ and working in X-Band[8] with range and azimuth resolutions of $10\ m$.

The focused image produced by a single point scatterer is also called Impulse Response Function (IRF) of the considered RADAR and it is usually presented as normalized to 1, as it is in Figure 2.12. The latter is a quite useful indicator of the imaging capabilities of a system since the width of the peak along the two axes can provide the approximated resolution along the respective axes at a glance.

2.3 Bistatic and multi-static SAR principles

To conclude this chapter, a brief explanation on how to extend the presented monostatic SAR concepts to the bistatic and multi-static cases is needed for the sake of completeness. Indeed, even if the monostatic SAR is a particular case of the bistatic one, there are some peculiarities which are worth highlighting, because they are needed to fully comprehend the SAR fleet designs illustrated in Chapter 4.

Starting from the bistatic case, in which two different antennas are used for transmission and reception, it is possible to delineate also the multi-static Synthetic Aperture RADAR configuration. This definition denotes systems which use multiple bistatic couples to perform observations of the same target. There are several ways in which a multi-static SAR

[8] Due to its very small bandwidth the P-Band has not been used to carry on this simulation, because at that height, it would have led to a very computational expensive and time-consuming procedure.

configuration can be set up. One would be to use several appropriately spaced receivers and just one transmitter emitting multiple beams, angled so that each of them impacts on a specific receiver. Alternatively, the complementary configuration could be implemented, namely multiple illuminators (RADAR jargon to indicate the transmitting systems) whose beams are received by a single antenna, like the multi-static SAR fleet designs proposed in this thesis in Chapter 4. However, the last solution gives rise to a non-trivial issue, since each beam has to be correctly identified to form the focused image. For this reason, the receiver has to be able to understand which transmitter has sent the signal which it is receiving in that moment. A possible solution to this problem consists in the implementation of a proper transmission scheme, like the one proposed in Chapter 4.

In a bistatic Synthetic Aperture RADAR, whether in its airborne or spaceborne implementation, the two different antennas can be either flown on-board separate crafts, or just the transmitting one is, while the receiver is on the ground (e.g. a ground station). The focus of this section is on the former implementation.

In Figure 2.13 it is sketched a bistatic SAR couple moving along the orbital trajectory, in the same way it has been done for the monostatic case in Figure 2.2.

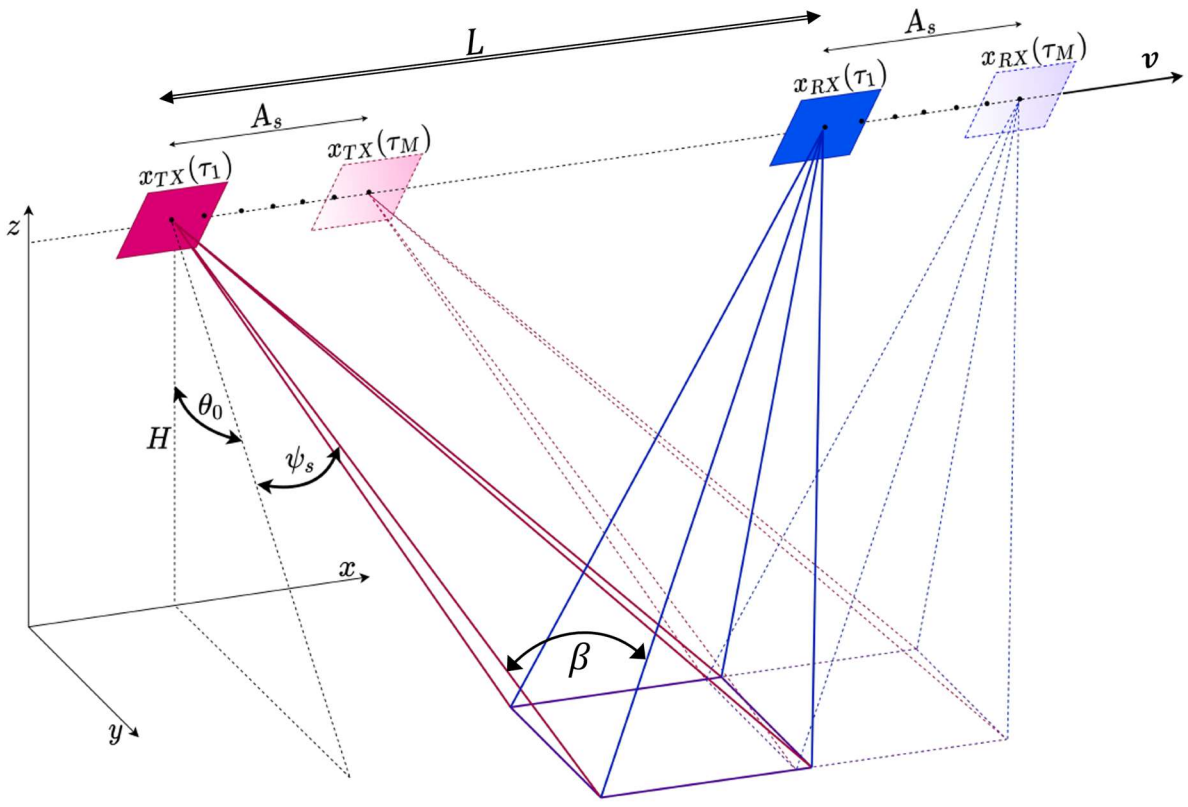

Figure 2.13: Bistatic SAR scheme

In this last image they are represented the two antennas moving as always along the x direction and the subscripts TX and RX stand for transmitter and receiver, respectively.

Along with the usual hypothesis of flat Earth, to avoid dealing with track curvatures at this preliminary design level, it has been also assumed that both the platforms are flown on the same orbit, thus that they share the same velocity v. This leads to a constant separation L between the two antennas, which only depends on the elevation angle θ, orbital altitude H and squint angle ψ_s (also called pointing angle in the azimuth direction), which are clearly depicted in Figure 2.13.

In a bistatic SAR, once the orbit and the separation between the transmitter and the receiver are established, the pointing angle comes consequently, as it can be understood by looking at the following equation.

$$\psi_s = \tan^{-1}\left(\frac{L\cos\theta_0}{2\,H}\right) \tag{2.43}$$

From this last equation it is clear that, in a monostatic SAR system, due to the fact that L is null, the pointing angle results to be equal to zero.

Another important angle to be defined is the bistatic angle β, shown also in Figure 2.13, which is defined as the double of the pointing angle, namely:

$$\beta = 2\tan^{-1}\left(\frac{L\cos\theta_0}{2\,H}\right) \tag{2.44}$$

Apart from the existence of these peculiar angles, an additional distinctive difference between a bistatic and a monostatic SAR lies on the range, or equivalently delay, computation. Indeed, to evaluate the delay in the bistatic configuration it is necessary to take into account separately the transmitter-to-target range ($r_{tx\to target}$ abbreviated as r_{tx}) and the target-to-receiver range ($r_{target\to rx}$ abbreviated as r_{rx}). This leads to the computation of the delay through the following equation:

$$d_{bis}(\tau) = \frac{r_{tx}(\tau) + r_{rx}(\tau)}{c} \tag{2.45}$$

where d is the delay, thus the time needed by the signal to reach the target and come back to the antenna, while the bis stands for bistatic. On the other hand, the delay in a monostatic SAR configuration can be easily computed as shown in Equation (2.4).

Moreover, for the sake of completeness, it is better to point out that, the range distances for a bistatic SAR, in the case of a single point target, are defined as:

$$r_{tx}(\tau, \boldsymbol{r}_t) = \sqrt{(x_{tx}(\tau) - x_t)^2 + (y_{tx}(\tau) - y_t)^2 + (z_{tx}(\tau) - z_t)^2} \tag{2.46}$$

$$r_{rx}(\tau, \boldsymbol{r}_t) = \sqrt{(x_{rx}(\tau) - x_t)^2 + (y_{rx}(\tau) - y_t)^2 + (z_{rx}(\tau) - z_t)^2} \tag{2.47}$$

in which $\boldsymbol{r}_t = [x_t \;\; y_t \;\; z_t]^T$ indicates the coordinates of the single point target.

Finally, having defined d_{bis}, it is also possible to rewrite the received signal formula, stated in Equation (2.35), as:

$$D(t,\tau) = A_t g\big(t - d_{bis}(\tau)\big) exp\left(-j\frac{2\pi}{\lambda} c\, d_{bis}(\tau)\right) \tag{2.48}$$

while the range compressed data matrix D_{rc} obtained in Equation (2.39) becomes:

$$D_{rc}(t,\tau) = A_t sinc\left(\big(t - d_{bis}(\tau)\big)B\right) exp\left(-j\frac{2\pi}{\lambda} c\, d_{bis}(\tau)\right) \tag{2.49}$$

Chapter 3
Multi-static Wavenumber Tessellation

One fundamental principle exploited in this work, which has allowed to design the presented SAR constellations, is the Multi-static Wavenumber Tessellation (MWT). Since the latter is derived from the Fundamental Equation of Diffraction Tomography (FEDT), in this chapter the derivation of the FEDT is performed. Then, this result is extended to the bistatic SAR scenario and the definition of the wavenumber vectors in the typical SAR frame is given.

In this way, the concept of Multi-static Wavenumber Tessellation to virtually increase the system bandwidth is explained and, to show the remarkable range resolution enhancement achievable by its implementation, at the end of this chapter, some relevant examples, obtained by means of proper simulations, are presented.

3.1 Fundamental Equation of Diffraction Tomography

Diffraction tomography is defined as the method of imaging based on reconstructing an object from measurements of the way in which it diffracts a probe signal, whose wavelength is the same order of magnitude as the object characteristic dimension [21]. The fundamental pillar of diffraction tomography is the so-called Fundamental Equation of Diffraction Tomography.

To introduce the latter, the starting point is the definition of the "basic scattering experiment", valid for almost all the remote sensing scenarios and systems: a signal is transmitted towards a target and the collection and analysis of the backscattered echo is used to reconstruct the scattering properties of the observed object. This formalization was first presented in the field of seismic exploration, therefore the following summary of what is proposed in [22] is consistent with geophysical sensing terminology.

Going into details, the experiment is set in an infinite medium, with a constant and homogeneous propagation velocity C_0, in which a transmitted plane wave is impinging on a distributed object embedded in the medium. Supposing that the receiver is far from the target, so that the scattered wave from it can be treated as a plane wave at the receiving point, it is possible to derive the relation between the scattered field and the object spectrum. For simplification, it is also considered the case of the acoustic wave equation with constant density, while the target is described by the velocity distribution $C(\boldsymbol{r})$, where $\boldsymbol{r}$ is the position vector.

The wave equation in the source-free region is:

$$\nabla^2 s(\boldsymbol{r}) + \frac{(2\pi f)^2}{C^2(\boldsymbol{r})} s(\boldsymbol{r}) = 0 \tag{3.1}$$

where ∇^2 is the Laplacian operator, $s(\boldsymbol{r})$ is a scalar quantity of the field (in geophysics it usually is pressure) and f is the frequency.

The scattering properties of the target itself are characterized by its object function $O(\boldsymbol{r})$ defined as:

$$O(\boldsymbol{r}) = 1 - \frac{{C_0}^2}{C^2(\boldsymbol{r})} \tag{3.2}$$

which, substituted in the (3.1), gives back the wave equation written in the following way:

$$\nabla^2 s(\boldsymbol{r}) + k^2 s(\boldsymbol{r}) = k^2 O(\boldsymbol{r}) s(\boldsymbol{r}) \tag{3.3}$$

where k is the so-called wavenumber of the field in the host medium, defined as:

$$k = 2\pi \frac{f}{C_0} \tag{3.4}$$

To make this scenario clearer, in Figure 3.1 a sketch of the experiment is reported.

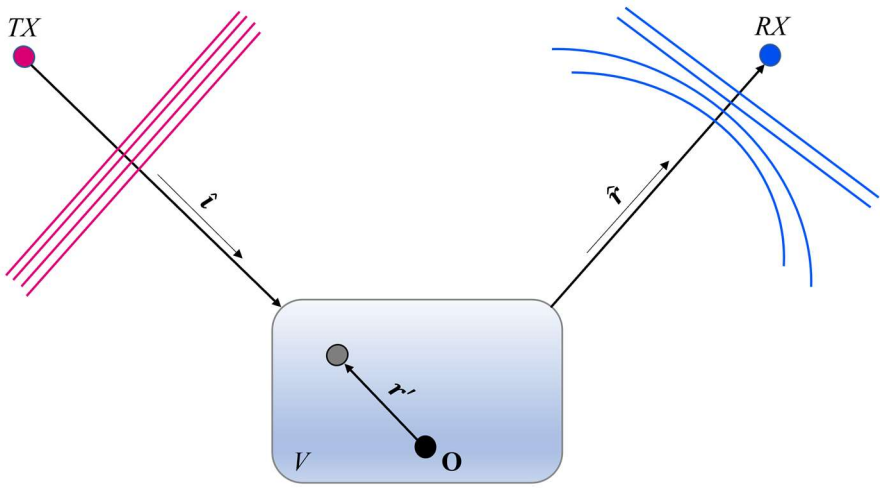

Figure 3.1: Geometry of the basic scattering experiment

At this point, assuming that $s(\boldsymbol{r})$ can be expressed as the superposition of the incident wave s_0 and the scattered wave S as:

$$s(\boldsymbol{r}) = s_0(\boldsymbol{r}) + S(\boldsymbol{r}) \tag{3.5}$$

by using Equation (3.5) inside Equation (3.3), the following new form of the wave equation is obtained.

$$\nabla^2 S(\boldsymbol{r}) + k^2 S(\boldsymbol{r}) = k^2 O(\boldsymbol{r}) s(\boldsymbol{r}) \tag{3.6}$$

Then the $S(\boldsymbol{r})$ is worked out through the exploitation of the free-space Green's function $G(|\boldsymbol{r} - \boldsymbol{r}'|)$, becoming:

$$S(\boldsymbol{r}) = -\int_V k^2\, O(\boldsymbol{r}') s(\boldsymbol{r}') G(|\boldsymbol{r} - \boldsymbol{r}'|)\, d\boldsymbol{r}' \tag{3.7}$$

where the integration is taken over the volume of the object V.

At this point, in order to proceed, a very strong assumption must be made: the object constitutes a so-called weak scatterer, i.e. the Born approximation applies. This means that the total electromagnetic field is considered to be made up by the incident field only: $s(\boldsymbol{r}) \approx s_0(\boldsymbol{r})$.

By applying this strong assumption Equation (3.7) becomes:

$$S(\boldsymbol{r}) = -\int_V k^2\, O(\boldsymbol{r}') s_0(\boldsymbol{r}') G(|\boldsymbol{r} - \boldsymbol{r}'|)\, d\boldsymbol{r}' \tag{3.8}$$

As it is discussed in Chapter 5, the validation of this hypothesis is non-trivial in the general case and thus its applicability has to be adequately assessed. The Born approximation, along with the hypothesis that the transmitted signal is in the form:

$$s_0(\boldsymbol{r}') = exp(jk\hat{\boldsymbol{\imath}} \cdot \boldsymbol{r}') \tag{3.9}$$

where $\hat{\boldsymbol{\imath}}$ denotes the direction of propagation of the incident wave (see Figure 3.1), results in the following formulation of the Green's function:

$$G(|\boldsymbol{r} - \boldsymbol{r}'|) = \frac{exp(jk|\boldsymbol{r} - \boldsymbol{r}'|)}{|\boldsymbol{r} - \boldsymbol{r}'|} \tag{3.10}$$

Additionally, since the receiver is supposed to be far from the object, it is possible to use the Fraunhofer approximation for the Green's function, leading to the following plane wave written as:

$$G(|\boldsymbol{r} - \boldsymbol{r}'|) \approx \frac{exp\left(jk(r - \boldsymbol{r}' \cdot \hat{\boldsymbol{r}})\right)}{\boldsymbol{r}} \tag{3.11}$$

where $\hat{\boldsymbol{r}}$ is the unitary vector denoting the direction of propagation of the scattered wave, as it can be seen in Figure 3.1.

Using these approximations, thus substituting Equations (3.9) and (3.11) in Equation (3.8), runs to the following simplified writing:

$$S(\boldsymbol{r}) = -\frac{exp(jkr)}{r}\int_V k^2 O(\boldsymbol{r}')\, exp(-jk(\hat{\boldsymbol{r}} - \hat{\boldsymbol{\imath}})\cdot \boldsymbol{r}')\, d\boldsymbol{r}' \tag{3.12}$$

Looking at the above equation, it is quite evident that the integral resembles a 3D Fourier transform, so that the scattered field can be rewritten as:

$$S_{planar}(\hat{\boldsymbol{\imath}}, \hat{\boldsymbol{r}}) = -k^2 \mathcal{O}\big(k(\hat{\boldsymbol{r}} - \hat{\boldsymbol{\imath}})\big) \tag{3.13}$$

where the $\mathcal{O}$ indicates the 3D Fourier transform of the object function and $S_{planar}(\boldsymbol{r})$ is the plane-wave scattering response, thus the response of a target object hit by an incident planar wave, defined as follows:

$$S_{planar}(\boldsymbol{r}) = S(\boldsymbol{r}) r\, exp(-jkr) \tag{3.14}$$

Equation (3.13) is called Fundamental Equation of Diffraction Tomography. It relates the plane-wave scattering response $S_{planar}(\hat{\boldsymbol{\imath}}, \hat{\boldsymbol{r}})$, to the 3D spectral density of the object function $\mathcal{O}(\boldsymbol{K})$ at the 3D spatial frequency $\boldsymbol{K} = k(\hat{\boldsymbol{r}} - \hat{\boldsymbol{\imath}})$, where $\boldsymbol{K}$ is also referred to as global wavenumber vector. To be precise the link is with a single point of the 3D Fourier transform of the object function, point which only depends on two vectors whose direction is completely determined by the incident and backscattering angles [23].

Moreover, it is critical to recall that the above derivation has been carried out by exploiting the Born approximation, therefore, in scenarios in which the latter cannot be applied, the FEDT is not valid.

3.2 Equivalent bandwidth extension

Under the same hypothesis, the above general principle can be applied to the case of bistatic RADAR remote sensing, where transmitting and receiving antennas are used in place of seismic sources and geophones. Indeed, it is possible to extend the definition of wavenumber vectors given in Equation (3.13) to a bistatic SAR configuration (shown in Figure 2.13), simply by considering the following geometry illustrated in Figure 3.2.

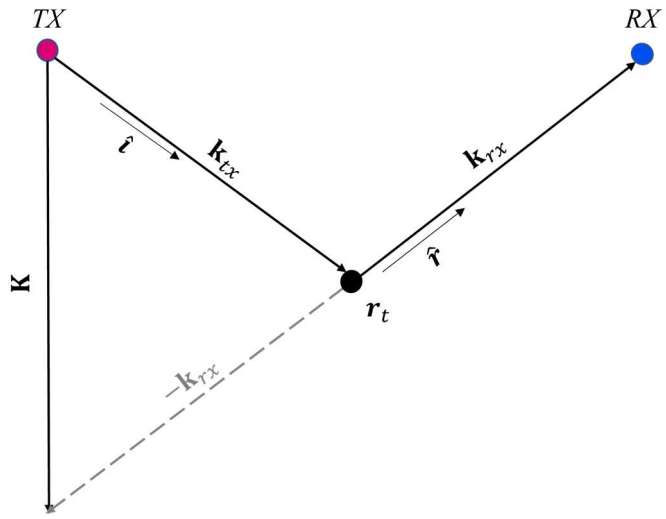

Figure 3.2: Wavenumber vectors for a point target in a bistatic SAR scenario

In this figure TX and RX always indicate the transmitter and receiver positions, while $\boldsymbol{r}_t = [x_t \;\; y_t \;\; z_t]^T$, as in Section 2.3, indicates the point target position. By referring to the geometry presented in Figure 3.2 it is possible to define:

$$\mathbf{k}_{tx} = \frac{2\pi}{\lambda}\hat{\boldsymbol{\imath}} = k\hat{\boldsymbol{\imath}} \tag{3.15}$$

$$\mathbf{k}_{rx} = \frac{2\pi}{\lambda}\hat{\boldsymbol{r}} = k\hat{\boldsymbol{r}} \tag{3.16}$$

where the vectors $\mathbf{k}_{tx}$ and $\mathbf{k}_{rx}$ represent the wavenumber vectors of plane waves traveling from the transmitter to the target at $\boldsymbol{r}_t$ and from the target to the receiving satellite, respectively. Indeed, $\mathbf{k}_{tx}$ directed in the direction of propagation of the transmitted wave while $\mathbf{k}_{rx}$ is directed towards the direction of propagation of the scattered wave (see Figure 3.2). Thus, the global wavenumber vector now becomes $\boldsymbol{K} = \mathbf{k}_{tx} - \mathbf{k}_{rx}$ and can be decomposed in the fundamental SAR directions shown in Figure 2.2, namely azimuth, ground and slant range and elevation, in the way presented in Figure 3.3.

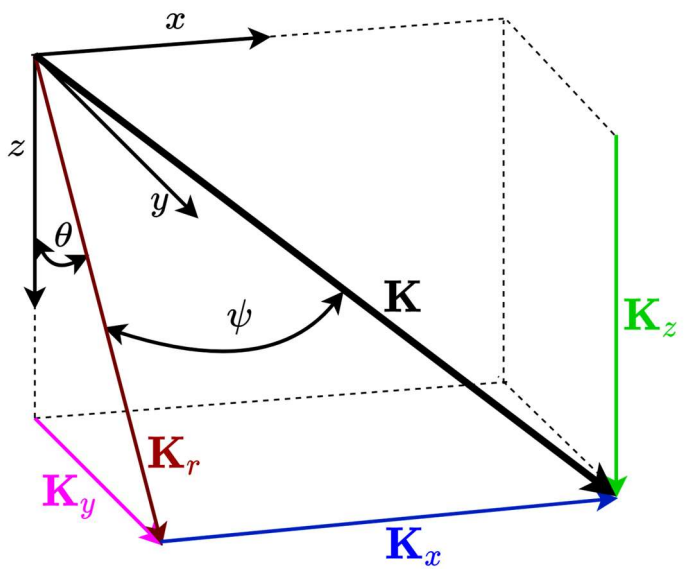

Figure 3.3: Decomposition of the global wavenumber vector

By referring to the geometry presented in Figure 3.3, the wavenumber vector components, in $[rad/m]$, for the bistatic SAR scenario, are defined according to the following mathematical expressions:

$$K_r = \frac{2\pi}{\lambda}[\cos(\psi_{tx}) + \cos(\psi_{rx})] \tag{3.17}$$

$$K_x = \frac{2\pi}{\lambda}[\sin(\psi_{tx}) + \sin(\psi_{rx})] \tag{3.18}$$

$$K_y = \frac{2\pi}{\lambda}[\cos(\psi_{tx})\sin(\theta_{tx}) + \cos(\psi_{rx})\sin(\theta_{rx})] \tag{3.19}$$

$$K_z = \frac{2\pi}{\lambda}[\cos(\psi_{tx})\cos(\theta_{tx}) + \cos(\psi_{rx})\cos(\theta_{rx})] \tag{3.20}$$

From these last equations, it has to be noticed that with the basic knowledge of the target position in terms of ψ and θ, it is possible to know exactly which wavenumber region will covered. Indeed, the wavenumber coverage performance of a SAR system, thus its performance in extracting **K** from a distributed scene, can be represented trough the so-called "eyeglass diagrams" or wavenumber coverage diagrams, which represent the vectorial components of **K** observed by the remote sensing system being evaluated.

To clarify this definition, in the following plot (right side of Figure 3.4), an example of wavenumber coverage map, computed by means of Equations (3.17) and (3.18) for the case of a point target, is presented.

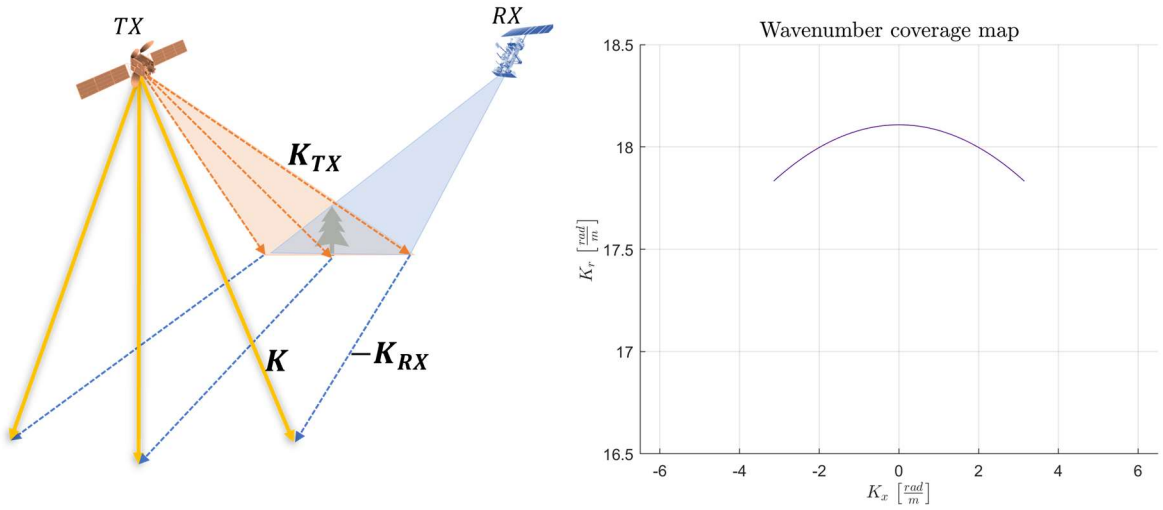

Figure 3.4: Wavenumber coverage map with one bistatic couple and no bandwidth

Of course, the sketch of the bistatic couple on the left side of this last figure, is just intended to show also graphically the provenience of the left plot.

However, systems like the one presented in this last image are unfeasible since they do not provide any range resolution due to the fact that, as it is explained in Section 2.1, ρ_r is directly related to the employed bandwidth B. Thus, an addition to Equations (3.17) and (3.18) must be done, leading to:

$$K_r = \frac{2\pi}{c}\left(f_0 \pm \frac{B}{2}\right)[\cos(\psi_{tx}) + \cos(\psi_{rx})] \tag{3.21}$$

$$K_x = \frac{2\pi}{c}\left(f_0 \pm \frac{B}{2}\right)[\sin(\psi_{tx}) + \sin(\psi_{rx})] \tag{3.22}$$

where f_0 simply indicates the carrier frequency employed by the SAR systems. Considering the same situation presented in Figure 3.4 but employing Equations (3.21) and (3.22), leads to the coverage diagram reported in Figure 3.5.

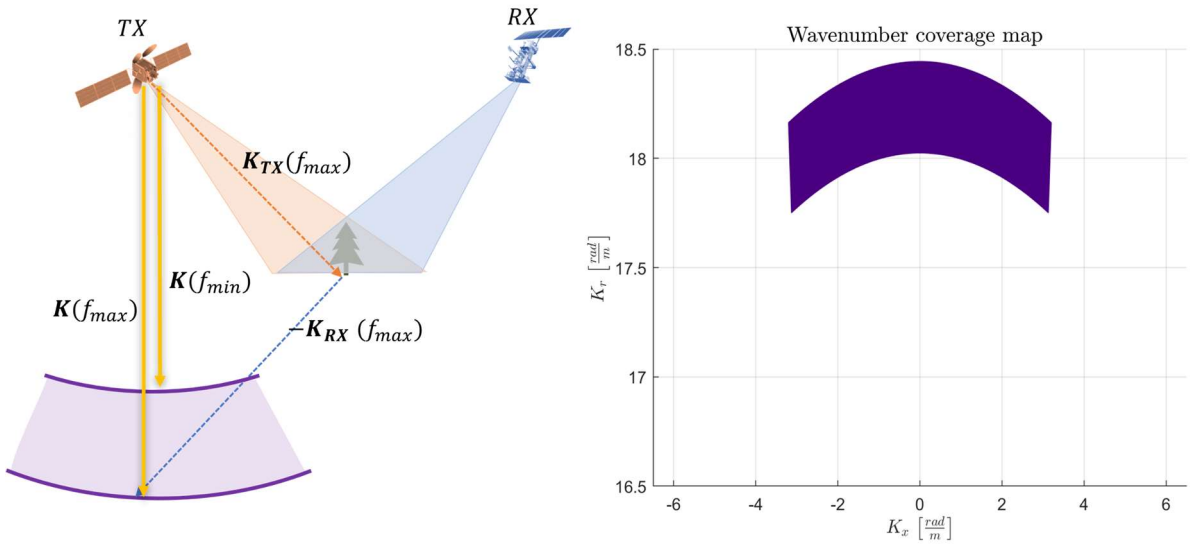

Figure 3.5: Wavenumber coverage map with one bistatic couple with bandwidth

In this last figure, to simplify the writing in the sketch, f_{max} and f_{min} have been used, having defined $f_{max} = f_0 + \frac{B}{2}$ while $f_{min} = f_0 - \frac{B}{2}$. The fundamental novelty of the plot, shown on the right side of Figure 3.5, is the fact that the line presented in Figure 3.4 has now become a "tile", thanks to the addition of the bandwidth term $\left(\pm\frac{B}{2}\right)$. Indeed, once the Equations (3.21) and (3.22) are evaluated for both signs, they give rise to the two lines presented on the left sketch of Figure 3.5: one that is the upper and one that is the lower boundary of the tile in right plot of this last figure. These two lines are the boundaries of the illuminated wavenumber region, which has been coloured also inside the edges just for graphical purposes.

By inspecting Figure 3.5, it is evident that this bandwidth addition does not change anything regarding the azimuth position of the illuminated wavenumber components, but it causes an increment in the range wavenumber coverage.

This makes it clear that the width of the tile in the K_r direction is determined by the bandwidth amplitude (see Equations (3.21) and (3.22)), thus it is also true that by finding a way to obtain the greatest wavenumber coverage in the range direction it is possible to virtually enlarge the system bandwidth. This equivalent larger bandwidth, that appears to be extremely interesting in the case of a P-Band SAR fleet, can be obtained by exploiting the Multi-static Wavenumber Tessellation principle [23].

Indeed, the latter is aimed to extend the range wavenumber coverage either by means of multiple bistatic couples or by utilizing a monostatic system together with different bistatic couples. In both these configurations each acquisition gives rise to a different tile (like the one presented in Figure 3.5) and it is possible to regulate the tiles' positioning in the coverage map by properly setting the relative distances between the satellites, thus the ψ angles under which the SAR systems see the target. If these separations are properly chosen, the tiles appear to be

perfectly adjacent one to the other in the wavenumber coverage map, as it is shown in Figure 3.6.

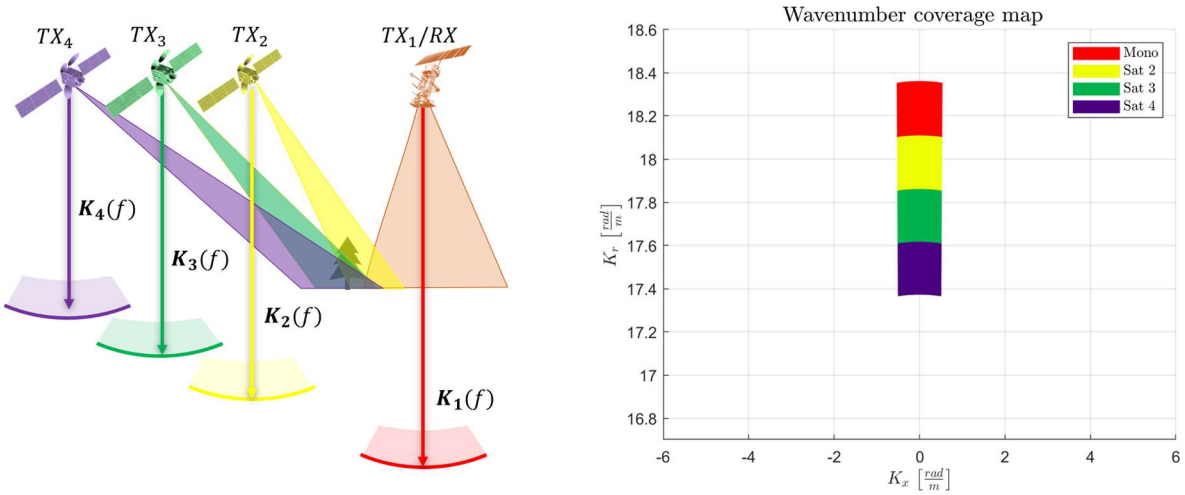

Figure 3.6: Wavenumber coverage map with 4 satellites

In this last figure, the first satellite works firstly as a monostatic and then as a receiver for the other three transmitters. The condition of having all the tiles one on the other, therefore creating a "tessellation", is what gives the name Multi-static Wavenumber Tessellation to this principle.

The fundamental result of a properly performed "tessellation", like the one illustrated in Figure 3.6, is that this extended range wavenumber coverage results in a phenomenon that can be defined as equivalent bandwidth extension. Indeed, even if the real system bandwidth obviously does not change, the SAR performance in terms of range resolution appears to be remarkable enhanced, as if the system had a much wider available bandwidth.

The latter can be the solution to the main problem of the P-Band scenario. Indeed, despite the advantage of allowing a great penetrability, the missions intended to operate at P-Band are strongly limited by the poor range resolution due to the imposed $6\,MHz$ bandwidth (see Subsection 1.1.2). Nevertheless, by exploiting the virtual bandwidth extension via MWT is possible to achieve a significant range resolution enhancement, despite that small real bandwidth. Of course, there is also a downside, indeed the limits of this theory dwell in the approximations done to obtain it, in fact the non-trivial assumption of weak scattering has been made and this may not hold for every scenario. Nevertheless, concerning the usage of SAR for biomass investigation, also the results observed in bistatic SAR surveying of forested areas in Northern Europe are promising, as illustrated in [24] and [25]: for instance, the strong double bounce scattering mechanism, caused by tree stems in monostatic SAR, results to be strongly mitigated, as the scattered signal is collected at a different angle with respect to the transmitted one.

3.3 Simulations and results

At this point, to fully comprehend the potential of the analysis of the wavenumber vectors in estimating the imaging capabilities of a system and to appreciate the improvement given by the exploitation of the MWT concept, some examples are presented. The latter have been evaluated by means of a proper *MATLAB* code, a simulator specifically written with the aim of carrying on Multi-static Wavenumber Tessellation experiments and analysing the obtained improvements in terms of range resolution by evaluating the system IRF via TDBP (see Subsection 2.2.2).

Since this thesis is centred on the exploitation of the P-Band features, all the run simulations consider P-Band systems with some fixed characteristics that are illustrated in Table 3.1.

f_0	$435\ MHz$	Center frequency
λ	$0.689\ m$	Wavelength
H	$10\ km$	Orbital height
θ_0	$30°$	Pointing angle in elevation

Table 3.1: Simulations' fixed parameters

As it can be noticed, the orbital altitude employed in these simulations is far different from the one of any possible real SAR formations. Indeed, it has been considerably lowered, namely from around $600\ km$ or more to just $10\ km$, in order to keep the dimensions of the vector and matrices to a reasonable size, since H directly impacts on the ranges and thus on the synthetic aperture. Such a variation greatly reduces computing times but does not affect the validity of the principles upon which the whole work is based. The only sizable impact would be seen on a model accounting for curved Earth instead of the "classic" flat Earth model, that is used in this thesis.

Moreover, it has to be remarked that the simulated orbit has been simplified as a straight line and in particular, to simulate the trajectory for each satellite few operations have been performed. Firstly, a total length $L_{tot} = 2A_s$ has been generated, in order to be able to exploit all the synthetic aperture also retaining some margin, to consider the presence of possible sidelobes in the antenna pattern. Then the position of the point target, that is common to all the simulations whose results are presented in this section, has been defined as:

$$x_0 = 0 \quad \text{and} \quad y_0 = H\ \tan\theta_0$$

In this way the target is in the origin of the satellites' trajectory, which has been created with a sampling along the azimuth direction of $\Delta x = \frac{\rho_x}{2}$, in order to be sure not to miss SAR data as well as to get rid of all the ambiguities in the along-track direction (see Section 2.1). Then the azimuthal path of the first satellite of the fleet x_{track_1}, has been calculated as a vector as follows:

$$x_{track_1} = \left(x_0 - \frac{L_{tot}}{2} - \frac{L}{2}\right) : \Delta x : \left(x_0 + \frac{L_{tot}}{2} - \frac{L}{2}\right) \tag{3.23}$$

while the trajectories of all the other satellites are just displaced versions of x_{track_1}, evaluated as:

$$x_{track_2} = \left(x_0 - \frac{L_{tot}}{2} + \frac{L}{2}\right) : \Delta x : \left(x_0 + \frac{L_{tot}}{2} + \frac{L}{2}\right) \tag{3.24}$$

where L is the separation among transmitter and receiver, obviously different for each bistatic couple, because, as explained in Section 2.3, a multi-static SAR configuration can be read as multiple bistatic couples.

In particular, in these simulations, as presented in Figure 3.6, the first satellite has been set to work at first as monostatic (thus $L = 0\ km$) and then as a receiver for the others, while the following satellites sliding along $x_{tra\ \ _2}$ are set to be the transmitters. On the other hand, the arrays carrying information about the y and z coordinates of the just described trajectories are quite simple, since the path is a straight line with $y = 0$. Indeed, the elevation and the ground range coordinates for each satellite position along the orbit (thus for each τ) inside the vectors x_{track_1} or x_{track_2} are:

$$y = 0 \quad \text{and} \quad z = H \quad \forall \tau$$

By looking at Equations (3.23) and (3.24) it can be noticed that the satellites paths, simulated in this way, have always the target between themselves, as it is visible from the plot presented in Figure 3.7.

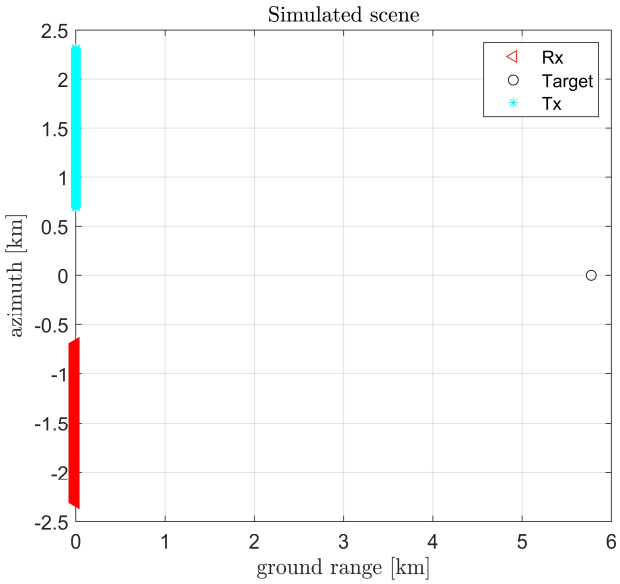

Figure 3.7: Example of simulated scene

In this last figure, an arbitrary L has been set just with the aim of showing an example of transmitter and receiver trajectories, in fact all the τ simulated for the satellites are shown. $x_{tra\ \ 1}$ and $x_{trac\ 2}$ have been constructed in this way without any loss of generality, since the satellites flying along the orbit sooner or later will be for sure in the positions presented in Figure 3.7, therefore, for graphical purposes related to the MWT, it has been decided to simulate the trajectories in this way. Indeed, if the plots of the wavenumber coverage map are referred to SAR couples for which the ψ_{tx} and ψ_{rx} are symmetric (thus $\psi_{tx} = -\psi_{rx}$), then the tiles are always centred in the 0 of the K_x axis, only displaced along the K_r direction. This leads to very easy to read plots, like the one presented in Figure 3.6.

To conclude this introduction, it is worth mentioning that this simulator is a quite powerful and versatile tool, in fact it can work with all the center frequencies and frequency bands, all the possible fleet configurations and antenna features and also with as many as point targets it is desired. Of course, the only limit to consider in these choices is represented by the consequent computational burden.

Now that the main details about the simulator have been explained, the first example of this section can be presented. It consists in a monochromatic and monostatic scattering experiment with an azimuthal beamwidth $\Delta\psi = 10°$ and the other parameters as stated in Table 3.1. This implies that only the first satellite of the fleet has been activated and furthermore, being a monochromatic experiment means that $B = 0\ Hz$, thus just one frequency has been used, which in this case is f_0.

The evaluated wavenumber coverage diagram for the illuminated range and azimuth components is depicted in the plot in Figure 3.8.

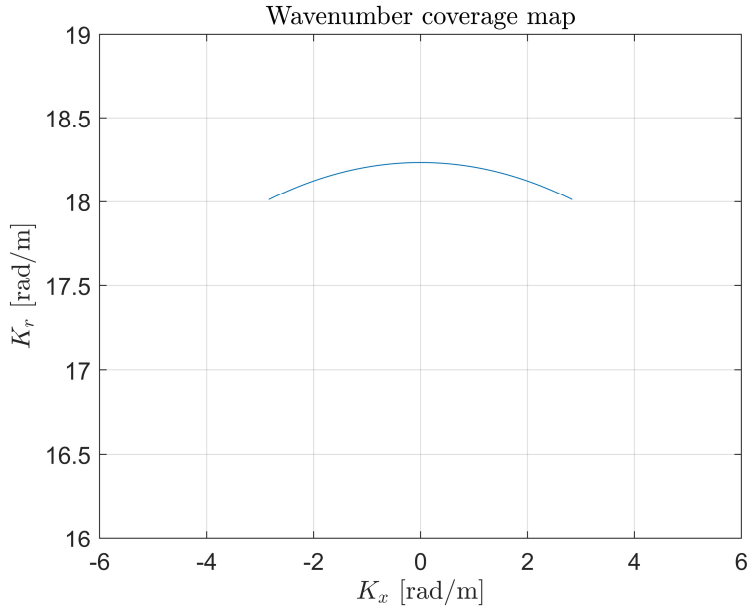

Figure 3.8: Wavenumber coverage map with $\Delta\psi = 10°$

The same experiment, with a doubled azimuthal beamwidth of $\Delta\psi = 20°$ (so a halved antenna length in the azimuth direction), produces the wavenumber coverage map shown in Figure 3.9.

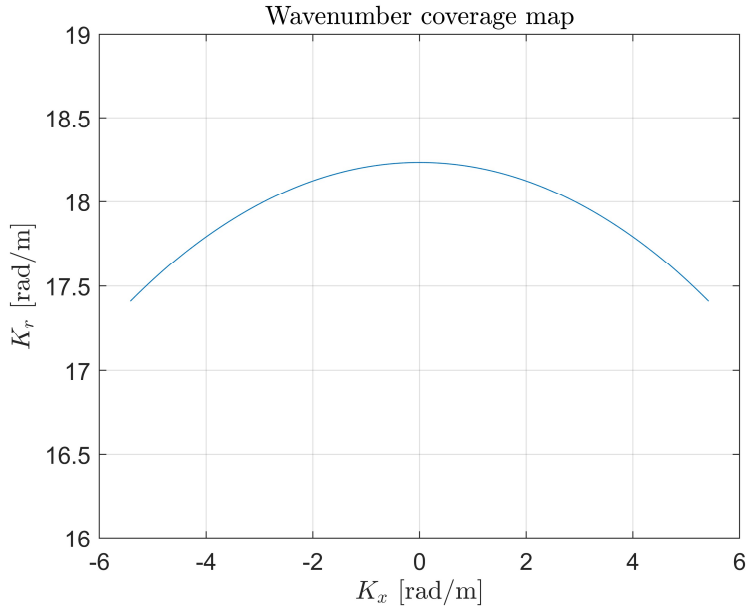

Figure 3.9: Wavenumber coverage map with $\Delta\psi = 20°$

This new monostatic system can observe a wider array of wavenumbers along the x direction with respect to the one with $\Delta\psi = 10°$, resulting in a finer azimuthal resolution.

To provide some range resolution, the same experiment is repeated by adding the P-Band bandwidth of 6 MHz and using again $\Delta\psi = 10°$, then the eyeglass diagram results to be the one shown in Figure 3.10.

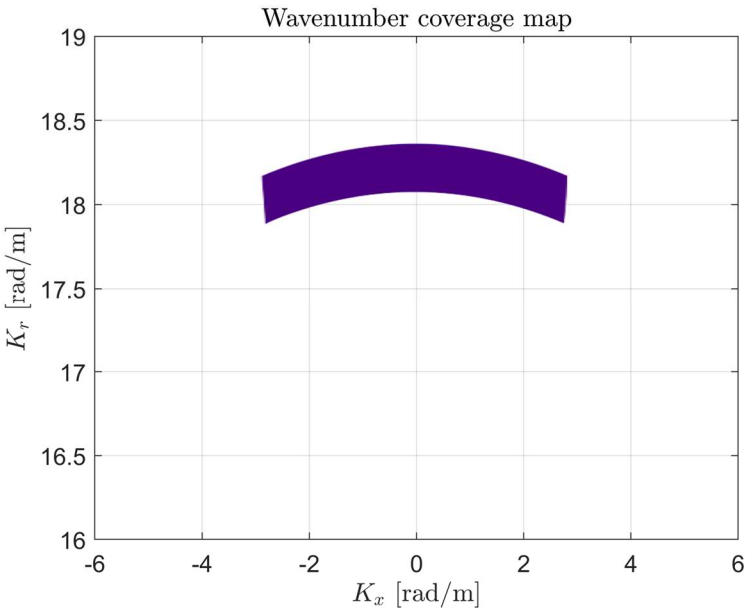

Figure 3.10: Wavenumber coverage map with $B = 6\ MHz$ and $\Delta\psi = 10°$

Nevertheless, it is worth mentioning that there is still a theoretical approach that allows to achieve some range resolution without bandwidth.

Indeed, this fourth experiment considers the addition of a transmitter, separated from the monostatic/receiver SAR system that produced Figure 3.8 by a distance $L = 3.9\ km$. This leads to obtain both a monostatic and a bi-static SAR acquisition and the same would apply also if the first satellite was a monostatic/transmitter SAR and the second system was just a receiver. In both cases, this configuration leads to the spectral coverage in the usual range-azimuth decomposition shown in Figure 3.11.

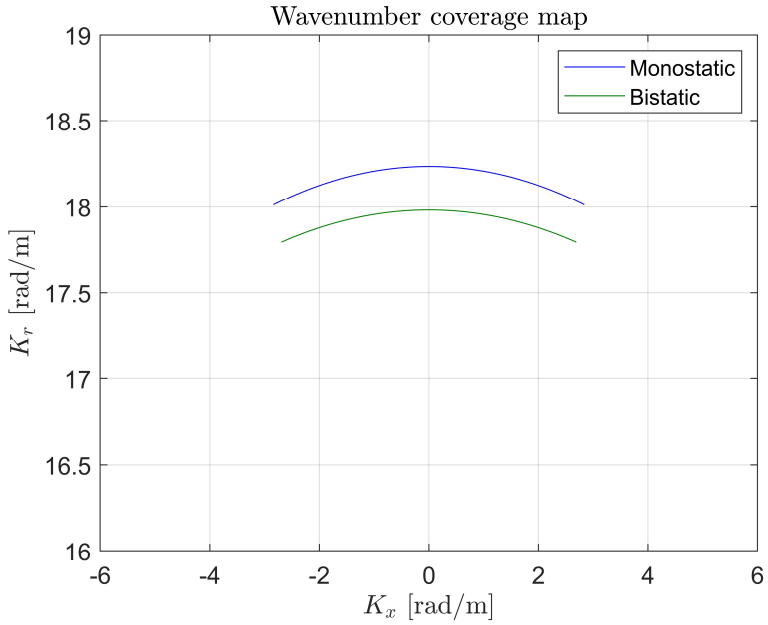

Figure 3.11: Wavenumber coverage map of 2 satellites with $B = 0\ MHz$ and $L = 3.9\ km$

Here the first line is always resulting from the monostatic acquisition carried out by the first SAR, while the second one is originated by employing the first satellite as a receiver and the second one as a transmitter.

In the limit case, an infinite number of bistatic couples would produce a continuous tile of spectral coverage similar to the one obtained in the case of a monostatic observation with bandwidth (see Figure 3.10).

At this point it is interesting to inspect the resulting wavenumber diagram of the 2-satellites system just introduced, always considering $\Delta\psi = 10°$, but this time also accounting for the $6\ MHz$ bandwidth. This result is presented in Figure 3.12.

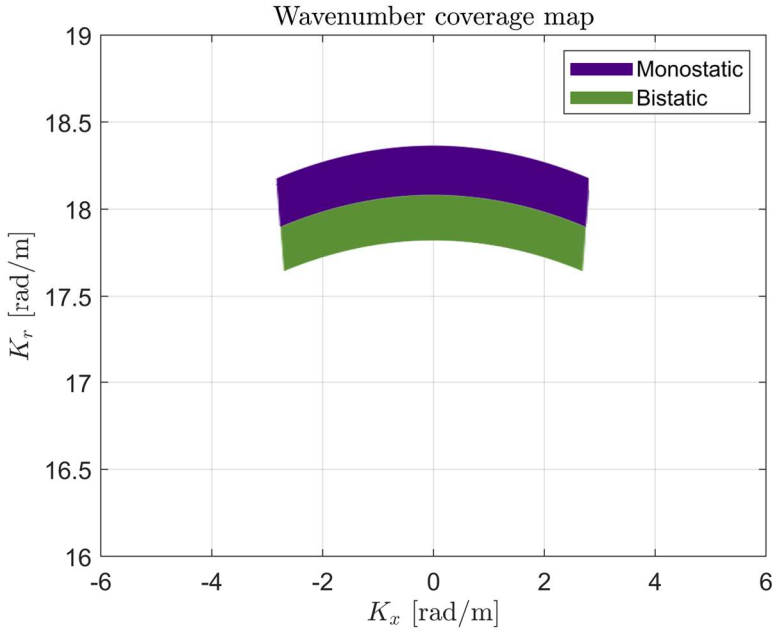

Figure 3.12: Wavenumber coverage map of 2 satellites with $B = 6\ MHz$ and $L = 3.9\ km$

As it is visible from this last figure, a proper choice of the separation among the satellites gives rise to a unique big tile, made up by the tiles obtained both from the monostatic system, which is always the blue one, and the new bistatic couple (the green tile).

Indeed, an appropriate choice of L, thus of the ψ angles, ensures that no discontinuities are present between subsequent tiles so that all of them tessellate into a single larger tile resulting in an increment of the range wavenumber coverage proportional to the number of bistatic couples employed. In fact, in Figure 3.12 it is clear that the wavenumber coverage in the range direction is doubled with respect to the simple monostatic case presented in Figure 3.10. This wavenumber exploitation, as explained in Section 3.2, is the core of the Multi-static Wavenumber Tessellation.

To fully comprehend the resolution enhancement provided by the multi-static solution with respect to its monostatic counterpart, in the following, the results of the focusing procedure via TDBP are shown. As mentioned in Section 2.2, the focused image produced by a single point target is the Impulse Response Function of the considered RADAR system. The latter is fundamental to evaluate the imaging performance of the considered system, that is the final aim of these simulations; for this reason, in these experiments, one point target has been used.

At this point it is worth highlighting that, to limit the computational burden arising from the use of the TDBP algorithm, without any loss of information, the focusing procedure has been carried out not on the whole simulated scene, but only on a small x, r window around the target position. Indeed, two new vectors have been created for this purpose, namely:

$$x_{foc} = x_0 + (-n{:}\,1{:}\,n)\ \mathrm{dx_{foc}} \tag{3.25}$$

$$r_{foc} = r_0 + (-n{:}\,1{:}\,n)\ \mathrm{dr_{foc}} \tag{3.26}$$

where r_0 is the range position of the point target computed as $r_0 = \sqrt{{y_0}^2 + H^2}$, n are values chosen arbitrarily according to the desired window dimensions while $\mathrm{dx_{foc}}$ and $\mathrm{dr_{foc}}$ are the sampling steps in azimuth and range direction, respectively. The latter have been chosen to respect the Nyquist Sampling Theorem and then they have been further refined in order to produce nice-looking images with smaller pixels.

The IRF corresponding to the RADAR systems of Figure 3.10 and 3.12, are presented in the two plots shown in Figure 3.13.

(a)

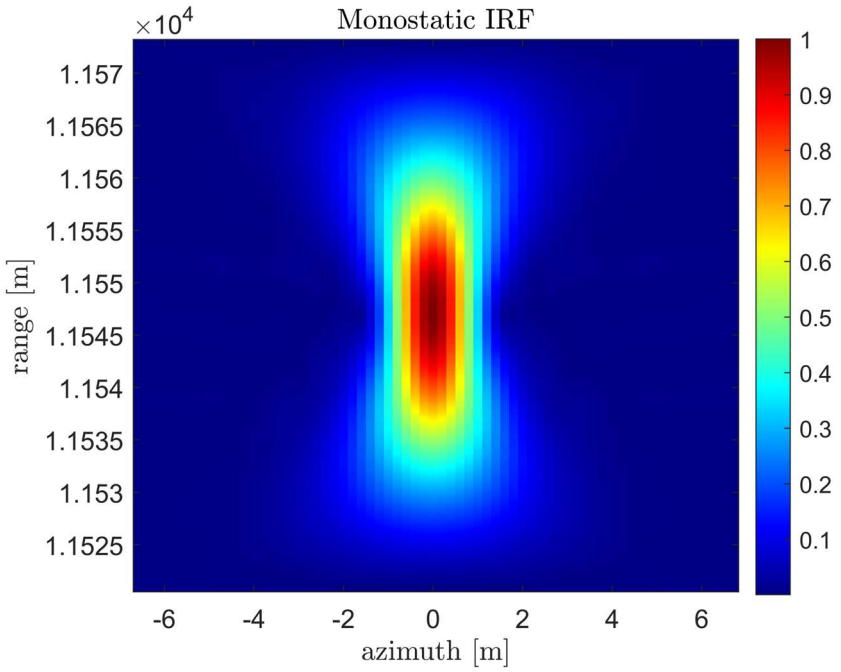

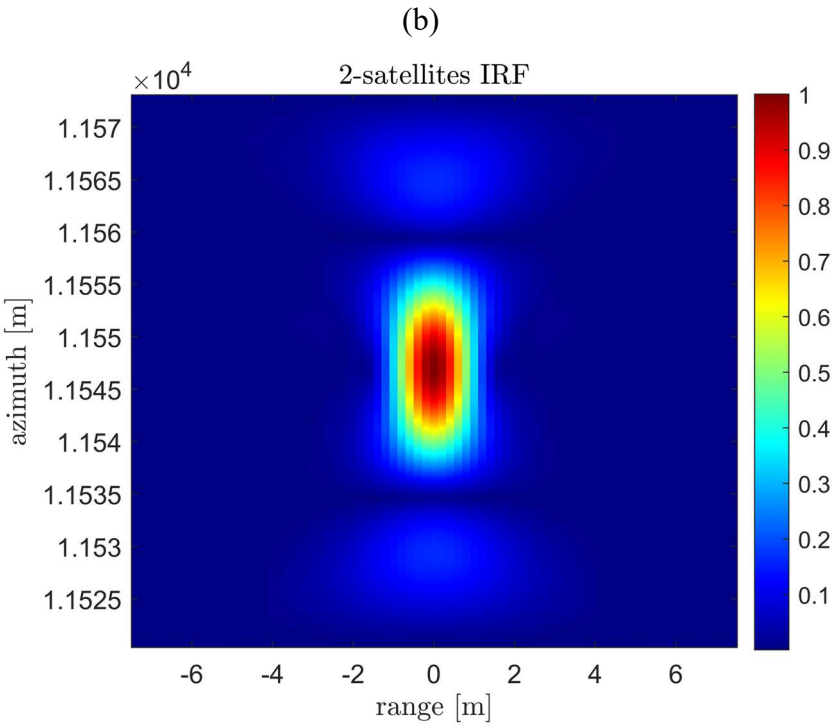

Figure 3.13: Monostatic IRF and 2-satellites configuration IRF

By looking at these two Impulse Response Functions it is evident the range resolution gain provided by the additional illuminator, while, as expected, the azimuth resolution remains the same in both cases. Indeed, it is better to highlight that the SAR resolutions, defined in Subsection 2.1 through their analytical formulations, are clearly visible in Figure 3.13 (a) and (b). In fact, the range resolution of the SAR system can be understood by inspecting the height of the high intensity part (main lobe) of the IRF, while the azimuth resolution can be understood from its width.

In the plot (b) the range resolution appears to be improved by a factor two, meaning that from $\rho_r \cong 25\ m$, peculiar of monostatic P-Band systems (as it is visible in the plot (a)), the range resolution for the 2-satellites system presented results to be $\rho_r \cong 12.5\ m$. This has been obtained thanks to the exploitation of the Multi-static Wavenumber Tessellation which results in the fact that the real system bandwidth of 6 MHz has been virtually doubled. At this point it can be understood that theoretically there is no limit to the resolution improvement that the exploitation of the MWT principle can provide, but of course a trade-off must be made between resolution gain and formation complexity.

Moreover, another important aspect is that this improvement in terms of range resolution, is predictable and easily quantifiable, since it is proportional to the number of adjacent tiles in the wavenumber coverage map, thus it is proportional to the number of satellites employed in the fleet (see Figure 3.13 (b)). This fact implies that there is no need to focus the image to verify the ρ_r enhancement, in fact it is only necessary to check the tessellation on the eyeglass diagram, which is far less computationally heavy to be obtained. Indeed, it requires only the

computation of range and azimuth wavenumbers, therefore, as shown in Equations (3.21) and (3.22), the wavenumber coverage map only requires the knowledge of the target position with respect to the SAR system to be evaluated.

This is a great result since focusing the image is a quite long and computational expensive procedure (as explained in Section 2.2) and in this case, once the azimuth angles are computed, hence the wavenumbers are available, it is possible to predict how the IRF will be. The latter is a massive advantage, that has been exploited also during the presented study to develop the fleet designs without the need of computing the IRF, which would have been computationally impossible to be performed with a common laptop, since for the SAR formation designs the real orbital height has been obviously employed.

Chapter 4
SAR Fleets design

The concept of adding illuminators to increase the system range resolution via Multi-static Wavenumber Tessellation, described in Chapter 3, is the core principle of the multi-static SAR fleet designs proposed in this chapter since it can represent a breakthrough for systems constrained by ITU regulations to work with very limited bandwidths, such as Biomass and all the systems intended to work in the P-Band scenario.

In this thesis the preliminary design of two multi-static SAR constellations has been developed, by employing the maximum allowable number of transmitters, in order to enhance the range resolution as much as possible to achieve the performance of high frequency systems, still retaining the priceless penetrability skill of the P-band. The limit in the number of illuminators that can be used exists since this work leverages the principle of Time Division Multiple Access (TDMA) whose characteristics and constraints are meticulously analysed in Subsection 4.1.1. At this point, it has to be underlined that a P-Band multi-static SAR formation would not have been even conceivable until few years ago, but at the present time, as discussed also in Subsection 1.1.4, there is a growing market interest in P-Band spaceborne SAR applications. Indeed, in this field the NASA JPL project proposed in [10] and the studies illustrated in [23] and [26] show interesting and feasible simulation results demonstrating that, in the next future, a scenario like the ones illustrated in this thesis can become reality.

In this context, the time seems just ripe to introduce the P-Band multi-static spaceborne SAR constellations proposed in this thesis, also designated as MultiSAR formations in the remainder of this dissertation, for the sake of brevity. Thus, in this chapter the preliminary design of the transmitting and receiving SAR systems, forming the aforementioned fleets, is presented along with the relative simulations' results and the analytical performance evaluation. Indeed, the two feasible constellation configurations proposed are compared with each other by analytically assessing the main performance parameters and, in the end of the chapter, the achieved resolution enhancement is evaluated by comparing the fleets' IRF with the one of Biomass.

To design these fleets specific computer tools have been created with the aim to adapt the existing analytical tools for the monostatic SAR system performance analysis to the presented multi-static SAR scenario. In fact, it is important to remark that the main goal of this thesis is to provide conceptual and informatic tools to deal with the MWT and with the multi-static SAR fleet design at P-Band. Indeed, the two fleets proposed in Subsection 4.2 are just two feasible and promising designs among infinite possibilities since, due to the presence of a huge quantity of design variables, according to different requirements it is possible to obtain totally different solutions by means of the same computer tools.

4.1 MultiSAR fundamentals

With the term MultiSAR it is designated a multi-static spaceborne SAR constellation, sharing some of the requirements and the operational specifications of Biomass and relying on the processing of multiple bistatic acquisitions to improve the range resolution with respect to the one provided by a traditional monostatic SAR. Employing the Biomass specifications, MultiSAR operates with a 6 MHz signal bandwidth centered around a carrier frequency $f_0 = 435\,MHz$, resulting in a very poor range resolution. Hence, the need to introduce a multi-satellite configuration, which allows to achieve a resolution improvement proportional to the number of satellites employed (see Chapter 3).

As mentioned in the foreword of this chapter, two MultiSAR configurations are proposed in Section 4.2 consisting of three identical satellites carrying a transmitting SAR system and only one spacecraft equipped with a receiver. The SAR systems in transmission employ a parabolic antenna to mimic as much as possible the Large Deployable Reflector (LDR) of the Biomass mission, which on the 21st of October 2021 has passed a key milestone with its successful deployment [27]. On the other hand, the receiving satellite, in both the proposed configurations, has been designed to use an antenna-array composed by different panels which in turn are made of different patch antennas as it is done in [10].

The reason behind the choice of using an array in reception is that being only one SAR receiver for all the transmitters, it must be capable of orient its antenna pattern (see Subsection 2.1.2) towards the desired transmitting satellite at each time, allowing in this way as many pointing directions as are the illuminators. This beam redirection, that in the antenna theory is called “beam steering”, can be performed or by rotating mechanically the antenna or by means of a phased array. The latter is a computer-controlled array of antennas which creates a beam of radio waves that can be electronically steered to point in different directions, without physically moving the antennas. Nowadays this technology is commonly used for airborne and spaceborne applications as shown in [28] and [29].

Moreover, the satellites of the presented fleets are designed to be flown along the same Low Earth Orbit (LEO) at an altitude of 600 km but each with a different true anomaly, so that the spacing between all of them is kept constant during the whole mission. In addition, in the framework of this dissertation, the receiving satellite is always set to be the head of these fleets as it can be noticed in the fleet formation sketch presented in Figure 4.1.

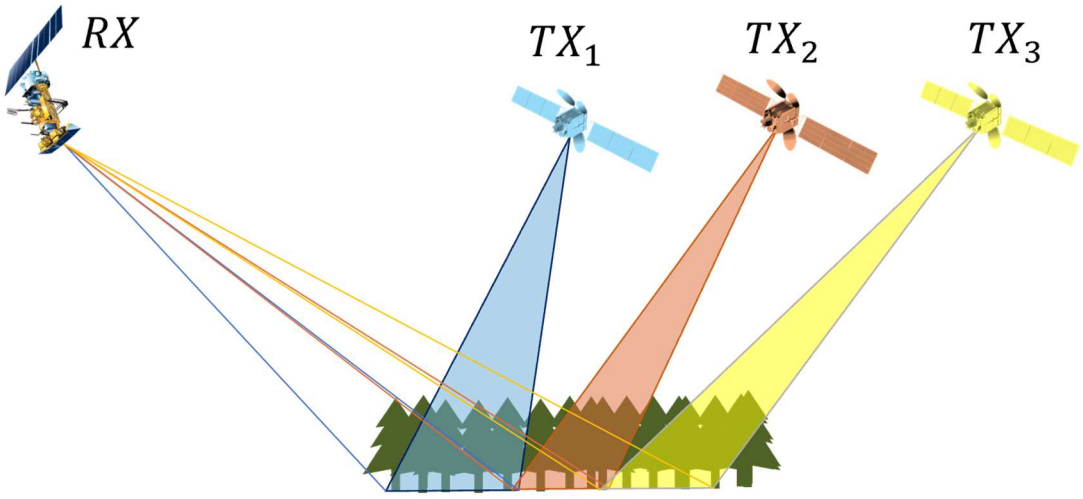

Figure 4.1: Constellation sketch

Of course, this illustration in Figure 4.1 is just aimed to give an immediate understanding of the MultiSAR concept, because the separation between the transmitters and their pointing angles are not the real ones. In this sketch the coloured triangles represent the illuminators' radiation beams, while the empty triangles, coming from the receiving array, are aimed to show its capability of steering its radiation pattern towards the transmitting satellites, to correctly receive all the backscattered signals. The overlap between the beams is intentionally sketched as very small, for reasons that are clarified in the following subsection.

The selected orbit for the MultiSAR fleets is almost like the one chosen for the Biomass mission, that is a LEO of 660 km of altitude but also a Sun-synchronous near circular dawn-dusk orbit, which is a special case of the polar orbit. Indeed, in a dawn-to-dusk orbit, the satellite is supposed to trail the Earth's shadow, thus when the sun shines on one side of the Earth, it casts a shadow on the opposite side[9] of the Blue Planet. Because the satellite never moves into this dark zone, the Sun's light is always on it (sort of like perpetual daytime), allowing the spacecraft to always have its solar panels in the sun, which is one of the main reasons to choose an orbit of this type. Furthermore, the Sun-synchronous orbits are often exploited by satellites carrying optical instruments, due to the fact that they keep the angle of sunlight on the surface of the Earth as consistent as possible, meaning that the satellites pass on a specific spot always at the same local solar time on the ground, though the angle will change from season to season. This consistency means that scientists can compare images from the same season over several years without worrying too much about extreme changes in shadows and lighting, which can create illusions of change [30]. Nevertheless, as it is explained in Section 2.1 the RADAR instrument is completely independent from lighting or weather conditions, therefore in this case the orbit selection has been driven by the fact that a SAR system needs a lot of electricity (since

[9] Since the satellite is close to the shadow, the part of the Earth the satellite is directly above is always at sunset or sunrise, leading to the name "dawn-dusk" orbit.

it is an active sensor) and the just described orbit is capable of keeping the instrument's solar panels always illuminated, allowing plenty of electricity for the instrument [29]. Moreover, for remote sensing it is always better to select a near polar orbit for coverage reasons and an almost circular one to maintain as much as possible the same distance on ground. Of course, the reasons behind the orbit selection for the Biomass mission are not only the just explained ones, indeed the LEO choice has been carried out also considering all the specific mission requirements.

Finally, to conclude this MultiSAR introduction, it is very important to highlight that both the fleets have been designed taking into account one of the main requirements coming from the Biomass mission, namely the necessity to guarantee a NESZ of at least $-27\ dB$ within all the ground swath [7]. Moreover, to be consistent, also the ground swath of the presented MultiSAR constellations has been designed to be almost equal to the one of Biomass. This constraint on the NESZ obviously affects the power request (see Equation (2.33)), in fact the transmitted power has been regulated differently in the two configurations to ensure in any case the fulfilment of this requirement.

4.1.1 Time Division Multiple Access

At this point it is necessary to explain the principle of Time Division Multiple Access (TDMA), which has been exploited in the fleet designs presented in this chapter.

When a constellation of multiple transmitters coupled with only one receiver is designed (like in these cases), a careful transmission planning is required. Indeed, the first thing to decide is how to differentiate the received signals according to which transmitter has sent them. In fact, the understanding of the signal origin is fundamental to perform a correct imaging, but it is also one of the main complexities of SAR constellations. Indeed, if the illuminators are set to transmit the signals simultaneously, then an interference between signals at the receiver is very likely to arise, becoming a remarkable challenge. Nevertheless, there are different available techniques to face this difficulty. A possible implementable technique to confront these interferences could be based on Orthogonal Frequency Division Multiple Access (OFDMA) or some Code Division Multiple Access (CDMA), popular among telecommunication systems. Both these access schemes are based on the orthogonality of the transmitted waveforms to achieve signal differentiation at the receiver side. However, in a SAR system surveying a distributed target (e.g., forests or near-subsurface regions, see Section 1.1), the energy of signals, orthogonal to the considered channel, would still be present after matched filtering. This is because usually the orthogonality is not guaranteed if one or more of waveforms present a time shift, which can be produced by the multitude of infinitesimal point-like targets distributed in the observed scene. The residual energy of all the orthogonal waveforms would cause a considerable noise level in the final image, especially if there are numerous transmitters (an exhaustive dissertation about these techniques be found at [31]).

In alternative to these methods a different approach is presented in [32], in which the enforcement of simultaneous reception of all the transmitted signals has been obtained through the differentiation of the received echoes by means of a proper processing algorithm.

On the other hand, to avoid interferences between the received signals it can be implemented also a Time Division Multiple Access (TDMA) scheme, which is the one employed in this thesis. The latter requires that different signals reach the receiver separated in time one from the other, to make it able of correctly forming the image. This temporal division between the backscattered echoes is a non-trivial challenge to be faced because it requires a careful design of the receiving array, as it is shown in Section 4.2. It is better to underline that, of course, also the transmitting antennas contribute in the same way, but, in these designs, they are fixed to mimic the Biomass LDR.

In any case, it has to be pointed out that a situation of complete non-overlap between the received echoes is unfeasible, for reasons that will be clear by looking at the plots in Section 4.2, in which all the simulations' results are shown.

At this point, it worth recalling that the proposed fleets design has been carried out with the aim of exploiting the higher possible number of bistatic couples (i.e., the highest possible number of transmitters, since the receiver has been set to be only one) in order to reach the best possible range resolution enhancement via MWT. Nevertheless, the number of satellites in transmission is heavily constrained not just by the formation cost and complexity, but also by the fact that the presented constellation designs leverage the aforementioned TDMA principle.

To implement the latter, it is necessary to ensure that all the signals arrive correctly separated at the receiver as well as that they all fit into the length of one PRI, determined by the transmitting satellites (which in this preliminary design have been set to be all equal). Indeed, since the PRI is the interval between one transmitted pulse and another, the fact that the received signals, emitted by the different illuminators, are constrained to fit in this time duration ensures that, if properly spaced in time, the transmissions of all the satellites do not interfere in a destructive way one with the other. To be clearer the concept is the following: if all the received signals stay within one transmitters' PRI interval, even accepting some small overlap (which is treated as shown in Subsection 4.2), this means that by the time the first transmitter send the second pulse, the receiving SAR system will have correctly received the first pulses from all the illuminators. In this way the risk of receiving the second pulse from the first transmitter before the reception of the first one from the last transmitter, thus the risk of having range ambiguities, is for sure avoided. Having said that, it is necessary to clarify that when discussing about a first transmitter it is meant the one closer to the receiving satellite, as shown in Figure 4.1. To sum up, due to the just mentioned reasons, the TDMA transmission scheme has been implemented by enforcing a proper synchronization plan among the transmitters, whose results are shown in the next section.

In any case, to make this transmission scheme easy to be understood, in Figure 4.2 a sketch representing the just described TDMA scheme, for a the three-transmitters configuration (like the two fleets designed), is shown.

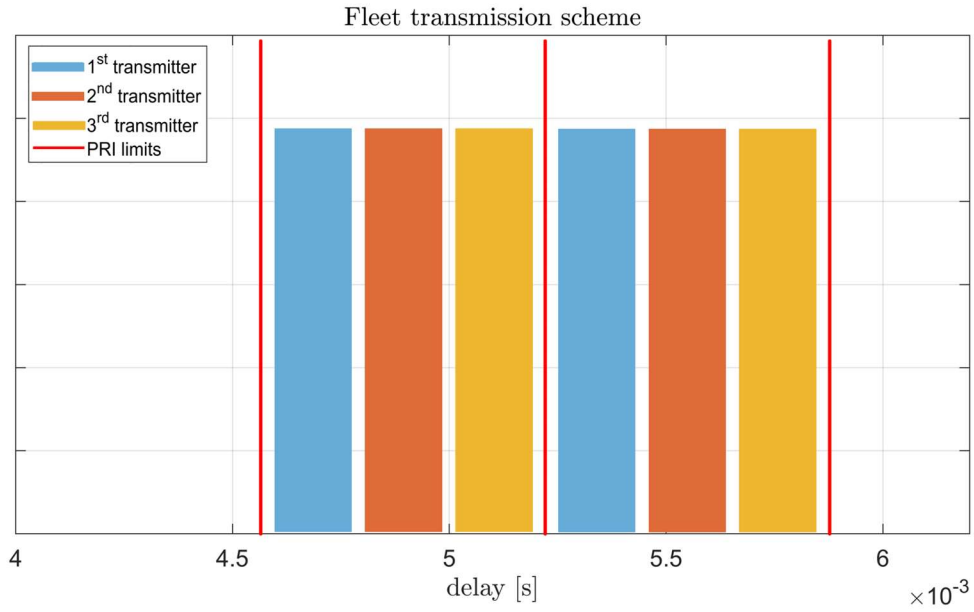

Figure 4.2: Fleet transmission scheme

In this last image the coloured rectangles (the same colours of Figure 4.1 have been used for the sake of clarity) represent the received signals sent by the different illuminators, while the red lines indicate the limits of the real transmitters' PRI duration. Anyway, the scheme presented in Figure 4.2 is just aimed to make clearer the previous concepts, in fact the real received signals have another shape as well as they are not equally spaced like these, as it is shown in Section 4.2. Nevertheless, the PRI length is the real one of the presented constellation designs (it does not vary among the two fleets), indeed, to obtain the plot in Figure 4.2, the real transmitters' parameters have been simulated (see Table 4.2).

Furthermore, the choice of showing only two PRIs in this last image is due to the fact that they are enough to make clearer how this situation in reception is repeated in the same way within each PRI, avoiding any ambiguity thanks to this TDMA technique. Moreover, the first PRI considered has the illustrated position on the delay axis because those milliseconds (thus a certain number of PRIs) are the ones really needed to receive the signal back, due to the long distances involved when a SAR operates from space.

At this point, it is better to specify that the same temporal separations between the received signals, needed to implement the TDMA scheme, can be achieved in two ways: or by letting the illuminators transmit their signal with a certain delay one with respect to the other (thus enforcing a proper synchronization scheme among the transmitters) or by letting the illuminators transmit their signals simultaneously but fixing the relative positions of transmitters and receiver along the orbit.

Since the main goal of the designed fleets is to enhance the overall system spatial resolution, the former solution must be considered, because the actual distances between the receiver and each transmitter have to be set in order to guarantee the best Multi-static Wavenumber Tessellation possible, as explained in Section 3.2.

For this reason, the optimal delays for the TDMA, that are the ones with which each signal must reach the receiving SAR to allow the less possible overlap between the received pulses, have been found for the two proposed fleets. In particular, these delays that have to be considered to enforce the synchronization scheme among the transmitters (see Table 4.9), have been found by simulating different distances L between the receiver and the transmitters and checking the consequent received signals separations on the fast time axis. Of course, it is worth highlighting that everything has been done always considering that all the backscattered echoes must fit in one PRI length, for the reason mentioned before.

In any case, since the two ways to achieve the received pulses separation for the TDMA lead to the same results, for the sake of simplicity, the SAR systems composing the two fleets have been designed, with the aforementioned computer tools, by considering the case of simultaneous transmissions. Therefore, the simulated spacings between the satellites are the ones allowing the less possible received signals overlap (see Table 4.4 and 4.6), thus the ones resulting in the just mentioned optimal delays. Indeed, once the systems design has been carried out, featuring the parameters and the performance shown in Section 4.2, the satellites positioning along the orbit has been properly changed according to the MWT necessities. In the end, since this variation has been coupled with the enforcement of a proper synchronization plan among the transmitters (based on the aforementioned optimal delays), the designed systems are capable both to perfectly distinguish the received signals as well as to achieve the remarkable range resolution enhancement via MWT shown, through the IRF evaluation, in Section 4.3. In fact, it is important to underline that the MultiSAR fleets presented in this thesis are designed to operate respecting the synchronization plan between the transmitters needed for the TDMA implementation and with separations among the satellites dictated by the MWT principle.

At this point, it is better to notice that the L values needed to obtain the best possible tessellation in the wavenumber coverage map, which are equal for both the fleets (see Section 4.3), have been assessed by employing the *MATLAB* simulator presented in Section 3.3.

4.2 Simulations and results

In this section all the results coming from simulating the two designed fleet configurations are shown and discussed. All the simulations presented in this section have been carried out by means of a proper *MATLAB* code, specifically written for this thesis, which adapts the tools for the monostatic SAR analysis to the multi-static case to deal with the multi-static SAR fleet designs at P-Band and its performance evaluation.

The basic fixed design parameters, which are in common to both the configurations and to transmitters and receiver, are shown in Table 4.1.

f_0	$435\ MHz$	Center frequency
B	$6\ MHz$	Bandwidth
λ	$0.689\ m$	Wavelength
H	$600\ km$	Orbital height
ρ_r	$24.98\ m$	Slant range resolution
θ_0	$30°$	Elevation pointing angle
ρ_y	$49.97\ m$	Ground range resolution
η	0.7	Antenna efficiency
σ_0	$-8.22\ dB$	Backscatter coefficient
T_{scene}	$290\ K$	Brightness temperature of external thermal sources
$T_{0,ant}$	$270\ K$	Physical temperature of the antenna
$T_{0,ref}$	$290\ K$	Reference temperature for the noise figure
F	$6\ dB$	Noise figure

Table 4.1: Simulations' fixed parameters

As mentioned in Section 4.1 the orbital altitude has been selected to be almost equal to the one chosen for the Biomass mission, also because it is always convenient to set an orbital height above $550\ km$ to strongly reduce the need for orbit maintenance manoeuvres [7].

The range resolution indicated in Table 4.1 has been simply computed by means of Equation (2.13), indeed is the typical value for P-Band systems, but in Section 4.3 it is shown how the equivalent bandwidth extension achieved via MWT allows to reach a far better range resolution.

Furthermore, the angle θ_0 was selected to be $30°$ since it is very close to the one of Biomass (which is $25°$ [6]) and it has also a direct match to the σ_0. Indeed, the values of the backscatter coefficient come from the analysis of specific SAR acquisitions and are tabulated for employed frequency band and incidence angle. By looking at the tables provided in [33] in the P-Band section, the lowest pointing angle present is $\theta_0 \cong 30°$, that in fact corresponds to forest observation. For this reason, to be consistent with the value of the backscatter coefficient and at the same time as close as possible to the pointing angle of Biomass, it has been chosen to set $\theta_0 = 30°$ leading to the value of σ_0 reported in Table 4.1.

Moreover, also the values of antenna efficiency, noise figure and brightness temperature of external thermal sources have been chosen to mimic the Biomass ones, while $T_{0,ant}$ could have been considered $290\ K$ too but, just to take into account the fact that the antenna is exposed to the cold space environment, it has been lowered a bit. On the other hand, as it is explained in Subsection 2.1.4, the value of $T_{0,ref}$ has been selected as it is customary for active systems to be equal to $290\ K$ and all the other temperatures have been computed according to Equations (2.31) and (2.32).

At this point, having presented the fixed simulation parameters, it has to be clarified how the orbital path has been simulated. In accordance with the usual SAR reference frame illustrated in Figure 2.13, the simulated trajectory has been simplified as a straight line in the along-track direction x and in particular, it has been set that:

$$x_{rx} = 0 \quad \text{and} \quad x_{tx} = x_{rx} + L \tag{4.1}$$

where x_{rx} and x_{tx} are the positions along the x axis of receiver and transmitters, respectively while L is the array containing the distances between the receiver and each transmitter. After this, the x axis vector has been created simply by using as first element x_{rx} and as last one the further transmitter position, both considered with some margin. It has to be remarked that it was possible to build the azimuthal axis in such a simple way and without any constraints, because the *MATLAB* code use to perform the simulations presented in this section is not meant to perform any focusing procedure. Indeed, when the TDPB algorithm has to be implemented (e.g., to evaluate the system IRF), the construction of x is totally different and it has to be performed carefully considering some constraints, as it is explained in Section 3.3.

On the other hand, the y axis, for the simulations presented in this section, has been built around y_0 which is:

$$y_0 = H \cdot tan\,\theta_0 \tag{4.2}$$

where, θ_0 is the central angle within the elevation beamwidth (see Figure 2.3), therefore y_0 is the ground range distance corresponding to the ground swath center. Thus, the vector for the y axis has been created centred on the middle of the ground swath and its length has been selected as a multiple of the real system ground swath (see following subsection). Finally, the z coordinate does not vary during the simulation, staying constantly equal to the orbital height.

4.2.1 Transmitting SAR systems

At this point, the features of the transmitting SAR systems, supposed to be all alike among them and in both the configurations, need to be explored. Indeed, what changes among the two fleets is the structure of the array and the transmitted power, that for this reason is not present in the following table.

The features of the designed illuminators are presented in Table 4.2.

W	$55\ km$	Ground swath
$\Delta\theta$	3.94°	Elevation beamwidth
$\Delta\psi$	3.94°	Azimuthal beamwidth
D	$12.23\ m$	Parabolic antenna diameter
A_s	$48.60\ km$	Maximum synthetic aperture
ρ_x	$5.01\ m$	Azimuthal resolution
Δx	$2.5\ m$	Spatial sampling of the synthetic aperture
PRI	$6.56 \times 10^{-4}\ s$	Pulse repetition interval
PRF	$1.52 \times 10^{3}\ Hz$	Pulse repetition frequency
G	$32.70\ dB$	Antenna gain
A_e	$70.34\ m^2$	Antenna effective area
δ	15%	Duty cycle
T	$9.84 \times 10^{-5}\ s$	Transmitted pulse duration

Table 4.2: Transmitters' parameters

At this point it is worth highlighting that all the parameters just shown in this table can be changed to simulate also a completely different fleets still using the same computer tool.

The starting point for the design of the SAR system in transmission has been the choice of the ground swath. In fact, as it is understandable from Section 2.1, once W is set, then the slant ranges and the $\Delta\theta$ come as a consequence leading to a unique value of the antenna diameter. The swath has been chosen to be $55\ km$ because it is very close to the Biomass one, indeed also the resulting antenna dimension is practically equal to the size of the Biomass LDR (i.e., $12\ m$) [7]. Furthermore, it has to be noticed that the ground swath cannot be too narrow because otherwise the antenna starts becoming huge till reaching unfeasible dimensions and moreover, having a very small W implies that the coverage of the interest areas needs a very long period of time to be achieved (see Subsection 4.2.5). On the other hand, having a huge swath reduces considerably the PRI length (see Section 2.1) leading to a

remarkable increase of the PRF and to a reduction of the number of transmitters that can be employed in the fleet if the TDMA scheme is used.

At this purpose, is worth mentioning that the selection of the PRI represents a critical issue in the real SAR systems design, leading to the necessity to perform a detailed analysis using numerical optimization for the choice of the most appropriate PRF for each SAR. Of course, in these preliminary fleet designs the computation of the PRI duration has been simplified but the main PRI constraints have been carefully taken into account. Indeed, to be sure that the selected PRI falls into the boundaries defined by the SAR trade-off (see Equations (2.11) and (2.12)) it has been computed as:

$$PRI = k\frac{\Delta x}{v} \tag{4.3}$$

where k is a positive constant with value between 0 and 2 while the along-track sampling Δx has been set to be equal to half of the azimuth resolution. It represents the distance travelled by the satellite between two subsequent transmissions and it is equivalent to the physical distance between two antennas in an array.

The choice of the along-track sampling is arbitrary but in order to get rid of ambiguities this spacing has to be lower than maximum along-track resolution allowed by the antenna beamwidth (the ρ_x value presented in Table 4.2). On the other hand, the coefficient has been set as $k = 1.98$, which leads the PRI to be very close to the upper limit stated in Equation (2.12). The reason behind this choice lies in the fact that exploiting the TDMA, as it shown in the previous section, the transmitter's PRI duration constraints the number of illuminators that can be used, thus the range resolution improvement which can be reached via MWT, so it has been decided to enlarge as much as possible PRI length, still staying within the SAR trade-off boundaries.

In addition, the duty cycle has been selected as 15% to be sure that the transmitted signals duration T (computed as stated in Equation 2.20) is short enough to allow a correct implementation of the TDMA technique.

Moreover, since it is common to all the transmitters, it has to be detailed the form of the transmitters' antenna pattern. Like it was mentioned in Subsection 2.1.2, the function which better resembles a real antenna radiation pattern is the cardinal sine, so the latter has been used in all the fleets' simulations for all the SAR systems. Nevertheless, the formula of the simulated radiation patter is not the same for the transmitters and the receiver, because for the latter it is necessary to take into account also the radiation pattern of the smaller antennas composing the array (see the following subsection). For the transmitters of both the MultiSAR configurations f_{tx} has been simulated as follows:

$$f_{tx} = \left(sinc\left(\frac{\theta_{tx} - \theta_0}{\Delta\theta_{tx}}\right) \times sinc\left(\frac{\psi_{tx} + \psi_s}{\Delta\psi_{tx}}\right)\right)^2 \tag{4.4}$$

where ψ_s and θ_0 are the pointing angles in azimuth and elevation respectively (as deeply explained in Chapter 2). In particular, it is interesting to notice that while the first one changes according to the bistatic SAR couple considered (see Equation (2.43)), θ_0 stays always constantly equal to 30°, as indicated in Table 4.1. On the other hand, θ_{tx} and ψ_{tx} are all the considered angles within the two beamwidths $\Delta\theta_{tx}$ and $\Delta\psi_{tx}$ listed in Table 4.2.

4.2.2 Receiving array outline

In this subsection some array features are presented. Since the major variation between one fleet configuration and the other lies in the design of the receiving array, it does not exist a unique subsection showing the receiving array parameters (like it is done in Subsection 4.2.1 for the transmitters' antenna), whose design does not change in the two fleet designs. Indeed, the only array characteristic common to both the proposed constellations is the fact that it is always designed as formed by different panels, that in turn are made by small patch antennas, as it is done in the NASA SESAR project, in which every panel has the form presented in Figure 4.3.

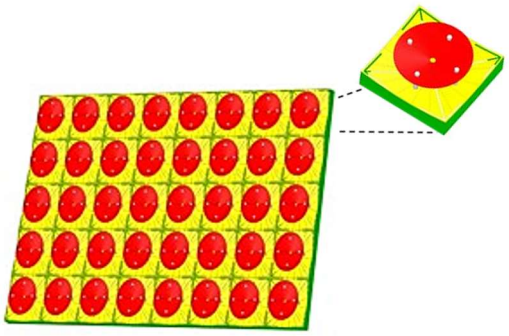

Figure 4.3: Array panel and patch antenna magnification *@NASA Goddard Flight Center*

The panel shown in this last figure is exactly the one used in [10], composed by 8x5 patch antennas, whose magnification is also illustrated in Figure 4.3. In the array configurations employed in this thesis what changes with respect to this last image is just the number of patch antennas for each panel, since also the patch dimension is almost equal to the one of SESAR, namely $0.35 \times 0.35\ m$ [10]. In fact, in the two designed MultiSAR configurations these small antennas have dimensions along azimuth and elevation of $0.30 \times 0.30\ m$ while the number of patch antennas for each panel has been set to be 8x8. On the other hand, the number of panels employed in the array is different among the two fleet designs, thus it is specified for each configuration (see Table 4.3 and 4.5).

At this point it is important to notice that a huge variety of array configurations can be simulated thanks to the degrees of freedom that have been introduced in the *MATLAB* code, namely: the patch dimensions and number for each panel and the panels number and

positioning. In the following subsections only two feasible array designs are presented, but they have been chosen among the others because, with far smaller dimensions with respect to the transmitters' antennas and a relatively low power transmitted, are still capable to guarantee good MultiSAR formations performance.

Moreover, since the array is formed by combining multiple patch antennas, its radiation pattern is influenced by the individual radiation patterns of all these small antennas. For this reason, it is important to always consider, together with the overall array pattern (the pattern of the array as seen like a conventional antenna), also the radiation patterns of the patch antennas composing the array. Indeed, during the development of this thesis, the array radiation pattern has been always simulated as:

$$f_{rx} = \left(sinc\left(\frac{\theta_{rx} - \theta_0}{\Delta\theta_{rx}}\right) \times sinc\left(\frac{\psi_{rx} - \psi_s}{\Delta\psi_{rx}}\right)\right)^2 \times \ldots \\ \times \left(sinc\left(\frac{\theta_{rx} - \theta_{0_{pat}}}{\Delta\theta_{patch}}\right) \times sinc\left(\frac{\psi_{rx} - \psi_{s_{patch}}}{\Delta\psi_{patch}}\right)\right)^2 \tag{4.5}$$

where θ_{rx} and ψ_{rx} are all the considered angles within the two beamwidths $\Delta\theta_{rx}$ and $\Delta\psi_{rx}$. On the other hand, $\theta_{0_{pat}}$ and $\psi_{s_{patch}}$, which have been assumed to be constant, are the equivalent of θ_0 and ψ_s for the single patch antenna. They have been set to have the following values in all the simulations:

$$\theta_{0_{patch}} = 30° \quad \text{and} \quad \psi_{s_{patch}} = 20° \tag{4.6}$$

where $\theta_{0_{patch}}$ has been selected to be equal to the pointing of the transmitters and the receiver, while $\psi_{s_{patch}}$ has been chosen as an intermediate value between the squint angles obtained by simulating the bistatic SAR couples.

This further accuracy in the computations plays a significant role in the final results, bringing the designs closer to the real scenario, besides the fact that it also represents an additional degree of freedom for the designs.

4.2.3 First fleet configuration results

In this subsection and in the following one, the two proposed fleet designs are presented, each one having its peculiar array configuration, but sharing the same kind and number of transmitting satellites. In Table 4.3 the features of the array designed for this first fleet configuration are listed.

Lx_{patch}	$0.3\ m$	Azimuthal length of the patch antenna
Lz_{patch}	$0.3\ m$	Elevation length of the patch antenna
N_{patch_x}	8	Number of patch antennas along x
N_{patch_z}	8	Number of patch antennas along z
Lx_{panel}	$2.4\ m$	Azimuthal length of the single panel
Lz_{panel}	$2.4\ m$	Elevation length of the single panel
N_{panel_x}	4	Number of panels along x
N_{panel_z}	2	Number of panels along z
Lx_{array}	$9.6\ m$	Azimuthal length of the array
Lz_{array}	$4.8\ m$	Elevation length of the array
$\Delta\theta_{patch}$	$131.62°$	Patch antenna elevation beamwidth
$\Delta\theta_{array}$	$8.22°$	Array elevation beamwidth
$\Delta\psi_{patch}$	$131.62°$	Patch antenna azimuthal beamwidth
$\Delta\psi_{array}$	$4.11°$	Array azimuthal beamwidth
ρ_x	$4.8\ m$	Array azimuthal resolution
G	$29.31\ dB$	Array gain
A_e	$32.26\ m^2$	Antenna effective area

Table 4.3: Array parameters – 1st fleet configuration

The number of patch antennas and the number of panels along the two directions have been selected after multiple trials to reduce as much as possible the overlap between the received signals as well as to have the smallest array possible to save space, weight and cost. Indeed, as it will be clearer in few pages, the antenna dimensions deeply influence the superpositions between two consequent signals at the receiver, because they impact the shape of the received signal. Indeed, according to the antenna dimensions the shape of its radiation pattern changes, becoming larger or narrower, with high sidelobes or low sidelobes.

Nevertheless, since very big antennas have been used for the transmitters, for the receiver it has been tried to reduce as much as possible the array size, to take into account the limited space availability in the fairing, thus avoiding unfeasible fleet designs.

At this point, it has to be pointed out that all the following results have been obtained by setting a separation L between the receiver and each transmitter (see Figure 2.13) as reported in Table 4.4.

1st bistatic couple	TX_1	RX	$L = 250\ km$
2nd bistatic couple	TX_2	RX	$L = 530\ km$
3rd bistatic couple	TX_3	RX	$L = 692\ km$

Table 4.4: Distances between each transmitter and the receiver - 1st fleet configuration

The power transmitted in this configuration has been set as $P_{tx} = 100\ W$ and, since the latter is supposed to be the same for all the illuminators, it has been selected by checking the NESZ (whose plots are shown at the end of this subsection) obtained by the bistatic couple formed with the last transmitter. Indeed, being the farther, the last illuminator is the one whose signal arrives the most attenuated at the receiver, therefore it is the one giving the worst NESZ inside the swath.

Now that all the assumed parameters have been declared, the time is ripe to introduce the simulation results. In Figure 4.4 the plots of the antenna radiation patterns of the transmitting and receiving SAR systems (computed as stated in Equations (4.4) and (4.5)) are shown together with their combined radiation pattern.

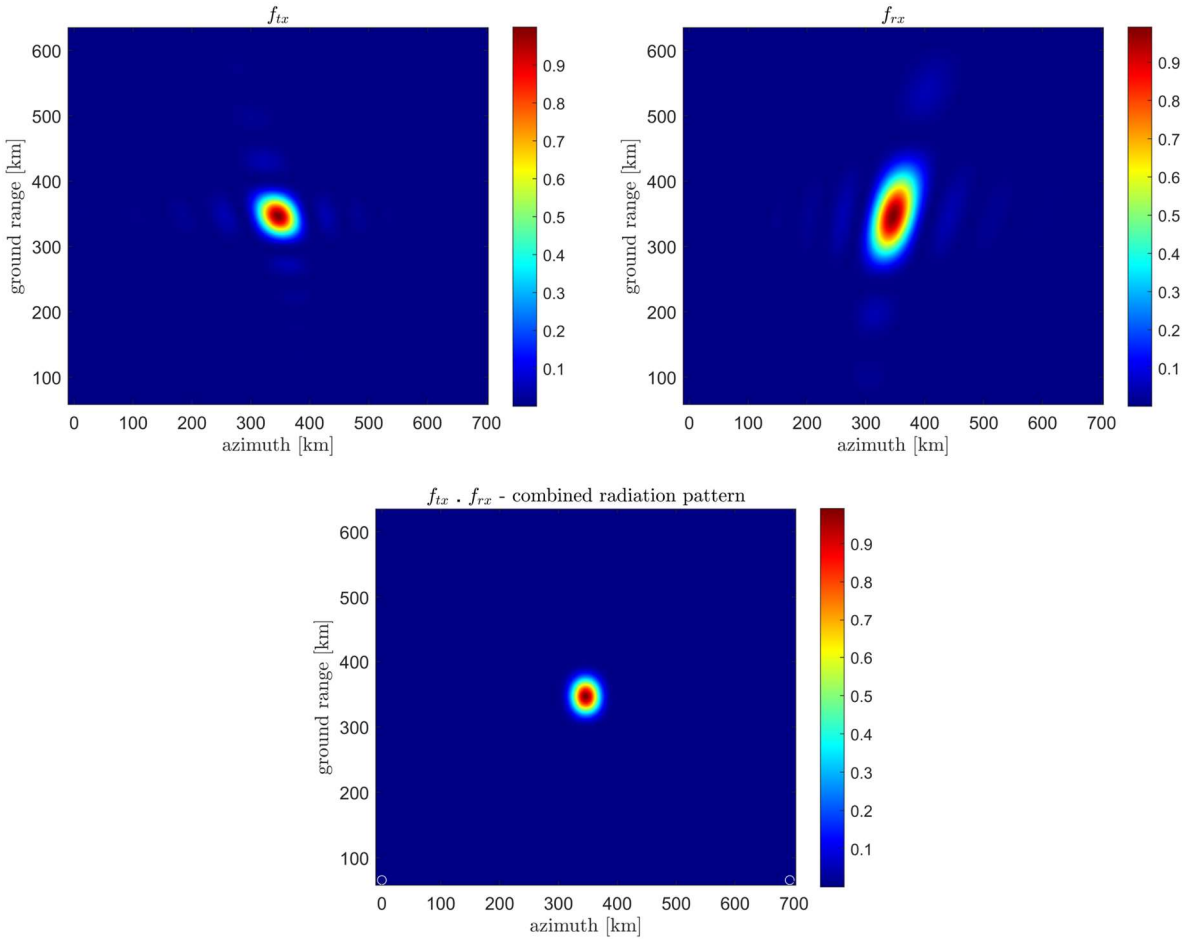

Figure 4.4: Radiation patterns – 1st fleet configuration

The presented patterns are shown in an azimuth-ground range reference frame because, in this way, by looking at the plots, it is possible clearly visualize the beam footprint on ground, thus the area illuminated by the SAR systems.

Furthermore, it has to be noticed that the presented antenna patterns are the ones of the third bistatic couple (i.e., RX and TX_3), as it can be understood from the position of the main lobes (see Subsection 2.1.2) on the azimuth axis. In particular, in the plot of the combined radiation pattern, the two white circles represent the simulated position of transmitter and receiver and it can be noticed that the main lobe of the radiation pattern falls exactly in the middle of their azimuthal separation (as it is expected by looking at Equation 2.26). The choice of a different bistatic couple would only have led to a main lobe translation to the left, according to the illuminator position, in all the three plots, with no shape variation of the pattern.

By looking at Figure 4.4 the features described in Table 4.2 and 4.3 can be recovered: for instance, the width of the main lobe in range and in azimuth depends on the antenna $\Delta\theta$ and $\Delta\psi$ respectively (according to Equations (4.4) and (4.5)) and it is also evident that the more the antenna is directive the smaller the main lobe of its radiation pattern is (see Subsection 2.1.2). For instance, f_{rx} is far wider than f_{tx} in the ground range direction, because the $\Delta\theta$ of the array

is twice the one of the illuminators' antennas. This in turn happens because the array dimension in the z direction is much smaller than diameter of the parabolic antennas (according to Equations (2.8) and (2.9)). On the other hand, the beamwidths in the azimuth direction are almost equal as it can be appreciated by looking at Table 4.2 and 4.3, but also inspecting Figure 4.4, resulting in a smaller difference of the pattern in the azimuth direction.

Thus, the narrower beamwidths of the transmitting SAR systems are due to the fact that the simulated parabolic antenna is much more directive than the array (as can be see looking at the values of the G in the Table 4.2 and 4.3) and this high directivity of the illuminators has allowed to design a relatively small array, since in any case the combined patter dimensions are significantly reduced by f_{tx}. In fact, by looking at the third plot in Figure 4.4, it is clear that the product $f_{tx} \cdot f_{rx}$ give rise to a very directive combined antenna pattern, in which also the side lobes (coloured in light blue) have lost almost all their amplitude, becoming invisible.

Having such a directive combined antenna pattern, with negligible sidelobes, is an extremely good result, since it means that no signal energy is lost in unwanted directions, thus less power can be transmitted because it is very well addressed (indeed only $100\ W$ are needed in this configuration).

Of course, the combined antenna pattern depicted in Figure 4.4 is what gives the shape to the received signal, in fact the received power is computed by means of the RADAR equation shown in Equation (2.26), in which the product between the receiver and the transmitter antenna patterns is used.

The power received for each bistatic acquisition is shown in Figure 4.5 always as an image function of azimuth and ground range.

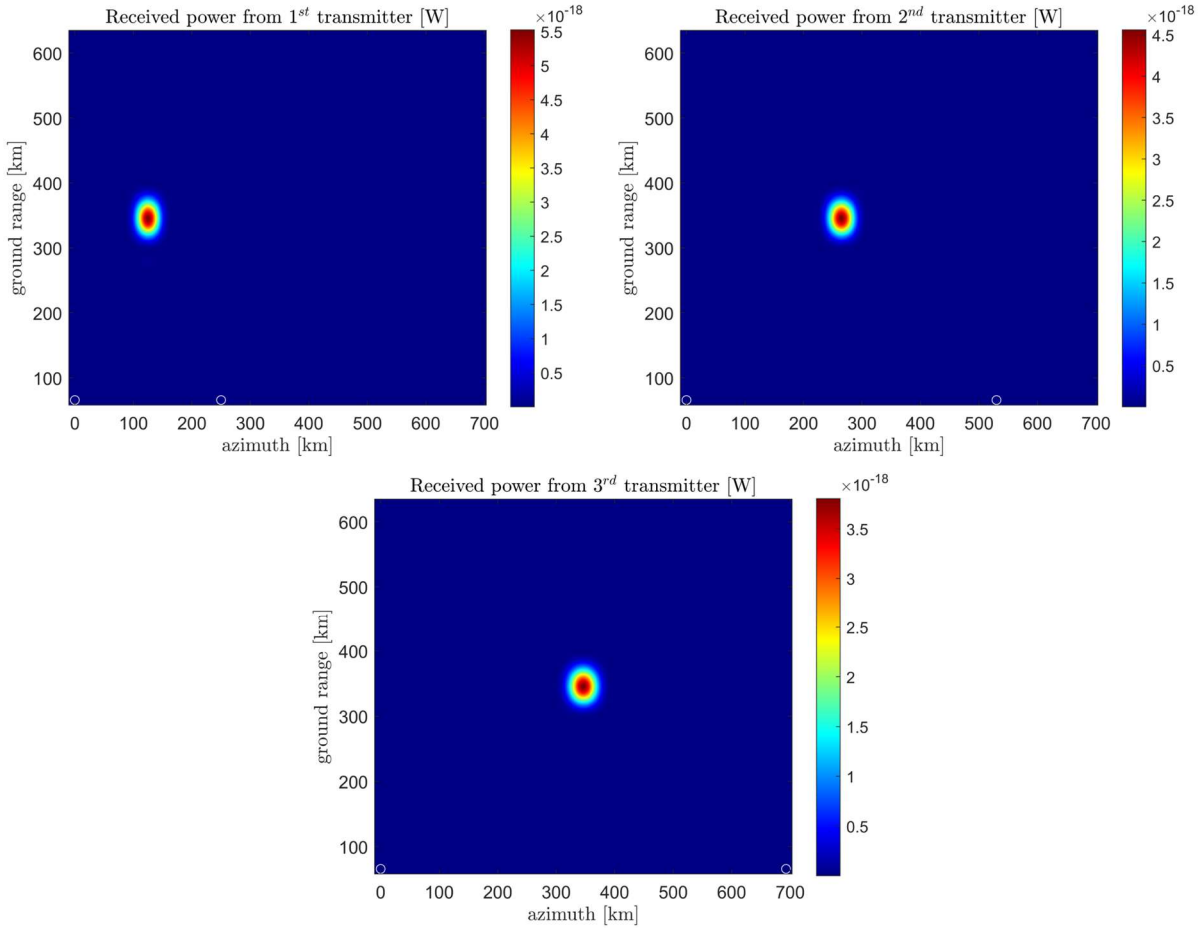

Figure 4.5: Received power – 1st fleet configuration

It can be noticed that also in these last plots, the two white circles represent the simulated position of transmitter and receiver.

To evaluate the separation and the overlap between the received signals it has been used the 1D version of the just presented power, expressed in $[dB]$ and plotted against the time delay. Indeed, these images have been converted to 1D plots by summing up all the power in the image pixels corresponding to the points on the imaged surface whose echoes reach the receiver simultaneously. In other words, each point in the 1D plot is given by the sum of the power contained in the pixels within a certain isochronous line, which corresponds to a surface portion located at an azimuth-ground range positions such as the echoes from this area reach the array in the same moment. To make it clearer, in Figure 4.6 the received power from the 3rd transmitter is plotted together with one isochronous line (indicated in light blue).

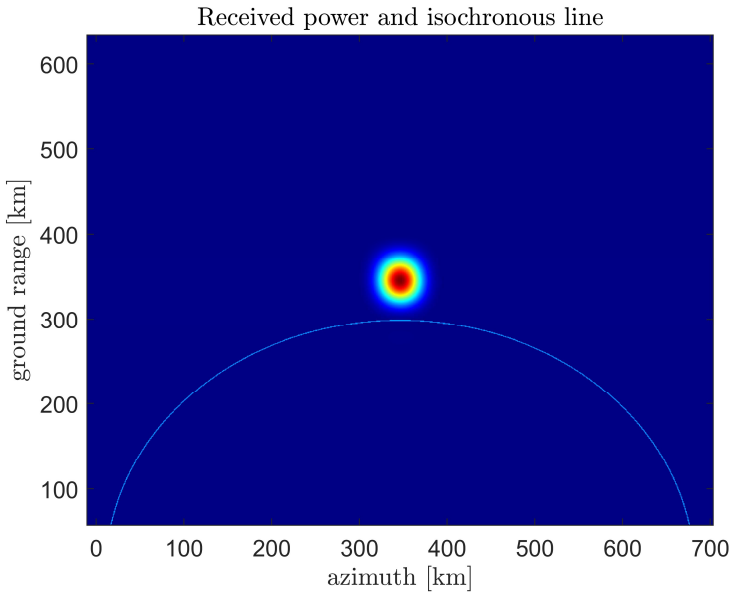

Figure 4.6: Received power and isochronous line

By summing the power present in all the pixels included in the light blue line, one point in the received power 1D plot is obtained, thus the whole graph is given by the evaluation of multiple isochronous lines.

This brief explanation is required to introduce the next image. Indeed, in Figure 4.7 the power received by orienting the array each time towards one different illuminator is presented as plotted against the time delay and with the same colours used in Figure 4.1 and 4.2.

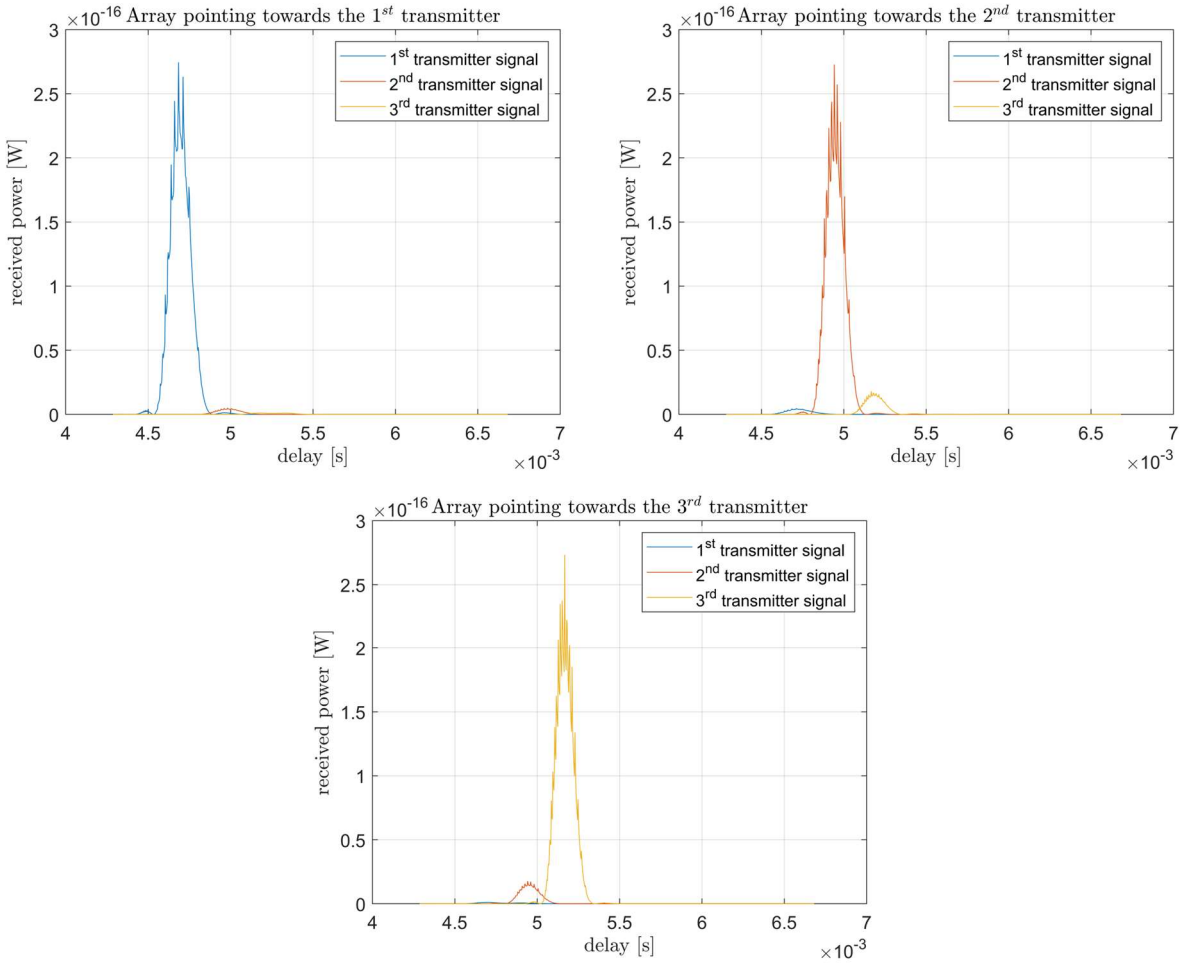

Figure 4.7: Received power Vs time delay – 1st fleet configuration

As mentioned before, in this last figure the plots of the received power are reported as a function of the time delay with which the signals are received by the array. It is worth mentioning that, as expected, due to the aforementioned technique with whom these plots have been built, the received power in Figure 4.7 appears to be higher with respect to the one presented in Figure 4.5.

From Figure 4.7, it can be appreciated also the result of the beam steering that the array is supposed to perform. Indeed, it is interesting to notice that the presented redirectioning of the array has been simulated through a proper combination of the antenna patterns, computed as stated in Equation (4.4) and (4.5). Indeed, in the time of one transmitters' PRI the receiver has to steer its radiation pattern towards all the three illuminators, obtaining the just presented results for the three pointing directions. In fact, in Figure 4.7 the three different array pointings (one for each transmitter) are shown and it is clear that even if the receiver is steered towards one illuminator at a time, also the signals from the other illuminators are received, although with a far lower intensity.

Furthermore, the intensity with which the signals coming from the transmitters towards which the array is not oriented (i.e., the small picks) reaches the receiver depends on two main

factors: the L values (or equivalently the delays between the transmissions from the different illuminators) and the receiver azimuthal beamwidth. Indeed, the finer is the latter the more the array is capable of cutting off the undesired signals from the other transmitters for each pointing, which in this context are read as interference. On the other hand, as introduced in Subsection 4.1.1, the distances L between the transmitters and the receiver (presented in Table 4.4), have been set to optimize the TDMA implementation, thus, to avoid an excessive overlap between subsequent signals, as it can be appreciated in Figure 4.7.

Nevertheless, since a situation of null temporal overlap is impossible (even more if the received echoes are constrained to fit in one transmitters' PRI), at a certain point, the received signals have been cut to avoid destructive interference. Therefore, the question that now arises is how to decide when the receiver has to stop "listening" to one specific illuminator and moving to the following one, thus when it has to change pointing direction, cutting the received echoes.

The adopted principle behind the signal cut is the following: the main signal is cut 20 dB above the interference from the other beams. This means that, as soon as the difference between the main signal power and the power of the unwanted echoes reaches 20 dB, the signal has been cut. The main signal, for each one of the three array pointing directions, is the one emitted by the illuminator towards which the array is oriented, while the other two signals, emitted by the other two transmitters, are read by the array as an interference, therefore as noise. The latter is for sure a strict requirement, since it implies that from the moment the main signal intensity becomes less than 100 times greater than the intensity of the interfering signals, the main signal is cut, nevertheless this criterion guarantees high performance in terms of interference rejection.

The plots of the received signals' power in $[dB]$, with the cutting points highlighted, are shown in Figure 4.8.

(a)

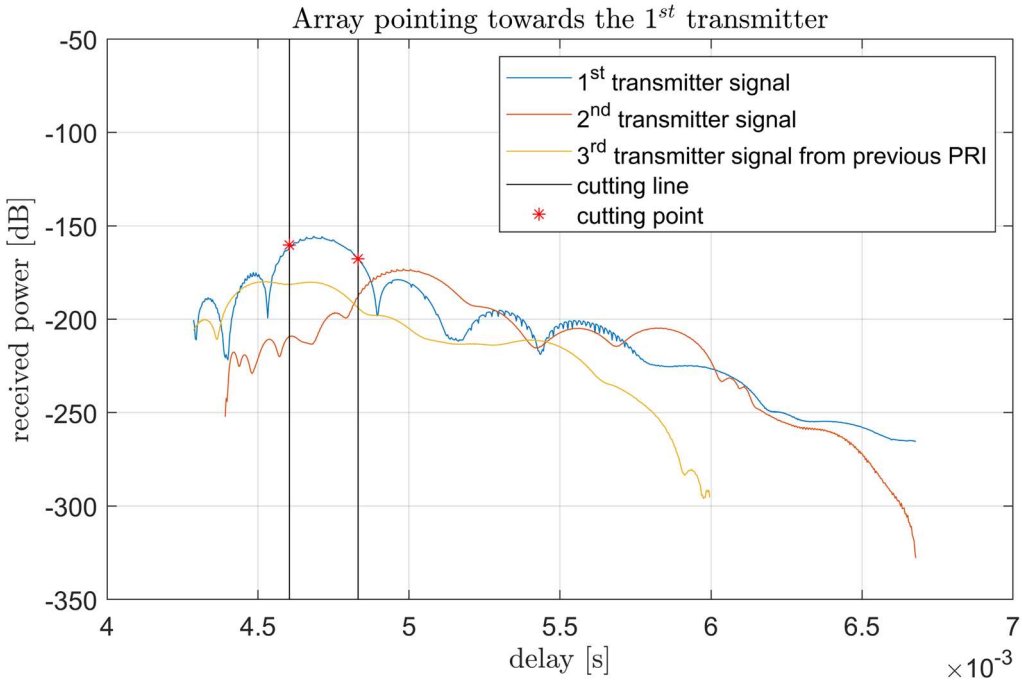

(b)

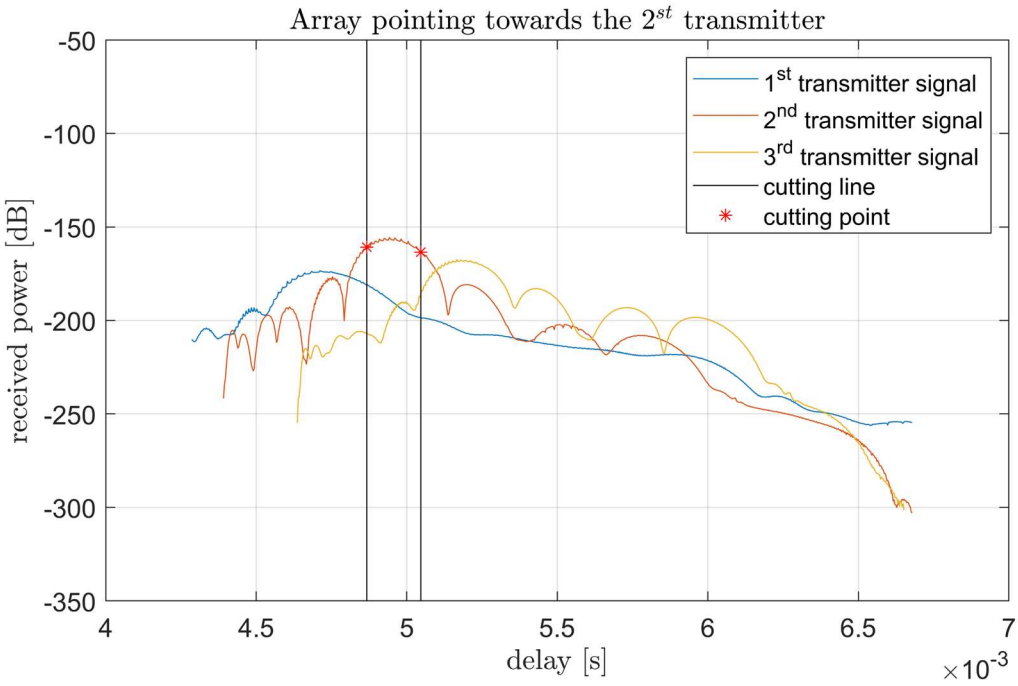

(c)

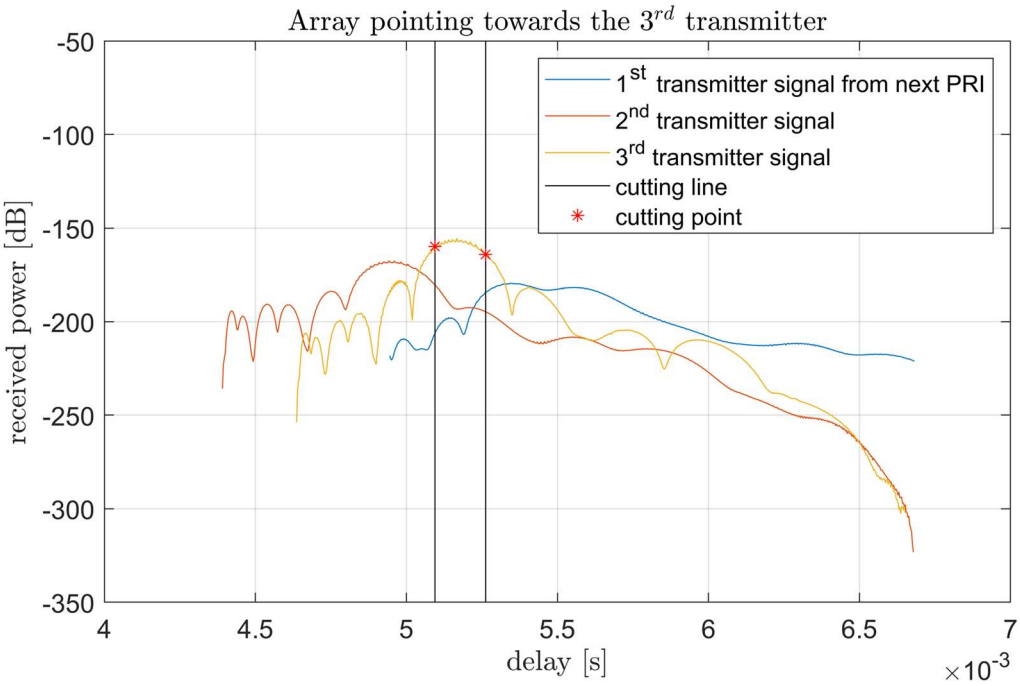

Figure 4.8: Signals' cutting – 1st fleet configuration

In these last plots each signal is presented its with interfering signals, namely the other two undesired signals with which the overlap occurs. For instance, in Figure 4.8 (a) the array is pointed towards the first transmitter, thus the desired signal is the one from the first illuminator

and the other two signals are read as interference. In particular, it can be noticed that also the signal from the third transmitter, belonging to the previous PRI, has been taken into account to consider the fact that all the signals have to fit in one PRI duration to apply the TDMA technique. The same reasoning has been done for the third plot (Figure 4.8 (c)), indeed it has been considered also the cutting point between the signal from the third transmitter (main signal) and the one from the first illuminator, coming from the next PRI, which in this case is read by the array as interference. On the other hand, in Figure 4.8 (b) the array is steered towards the second transmitter, so the signals from the first and the third illuminator represent the interference or equivalently, the noise.

Moving forward, once the signals have been cut in the cutting points just presented in Figure 4.8, the result of this procedure has been validated in terms of swath loss. Furthermore, it has to be stressed that the expression received signal or received power here are used as synonyms, in fact in the following image it is possible to visualize the same plots as in Figure 4.5 but cut according to the cutting points shown in Figure 4.8. Indeed, to be able to evaluate the effect of removing the portions of the signals falling outside the black vertical lines in the plots in Figure 4.8, the received power plots after the cut are depicted in Figure 4.9.

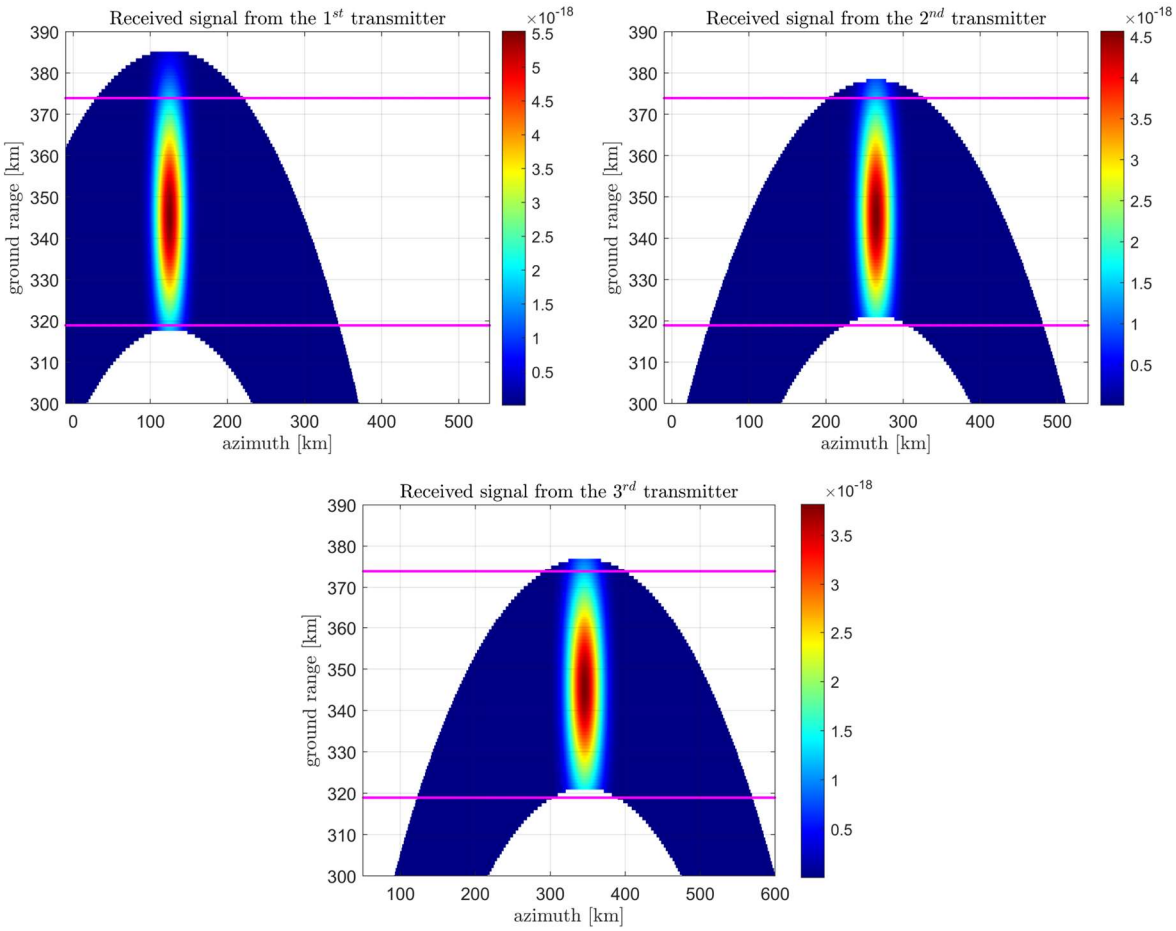

Figure 4.9: Cut received signals magnification – 1st fleet configuration

In these last plots the magenta lines represent the 55 km swath width, coming from the transmitters' parameters (see Table 4.2). These lines have been represented along all the length of the plot just for clarity, but of course in the azimuth direction the swath is limited by $\Delta\psi$. Moreover, these plots are magnified in order to better check if a swath loss has been caused by the cuts and its magnitude.

Indeed, it can be noticed that obviously the ground range coverage results to be reduced after the cutting procedure, and in particular by looking at the signals received from the second and third transmitters it is clear that the system is not capable of illuminating all the 55 km ground swath. Nevertheless, the design has been optimized in terms of signals' overlap, in fact the swath loss is of just 2 km in the two cases, while the signal from the first transmitter is not affected at all by this issue. Thus, by looking at Figure 4.9, it is possible to establish that the presented MultiSAR fleet is capable of imaging a ground swath of 53 km. Concluding this discussion about the ground range coverage, it has to be underlined that this swath loss can be avoided by setting a less strict requirement for the cutting procedure. Indeed, if the main signal is cut 17 dB above the interference from the other beams, instead of 20 dB, the fleet results to be capable of imaging the ground swath of 55 km, as it is clear by inspecting Figure 4.10.

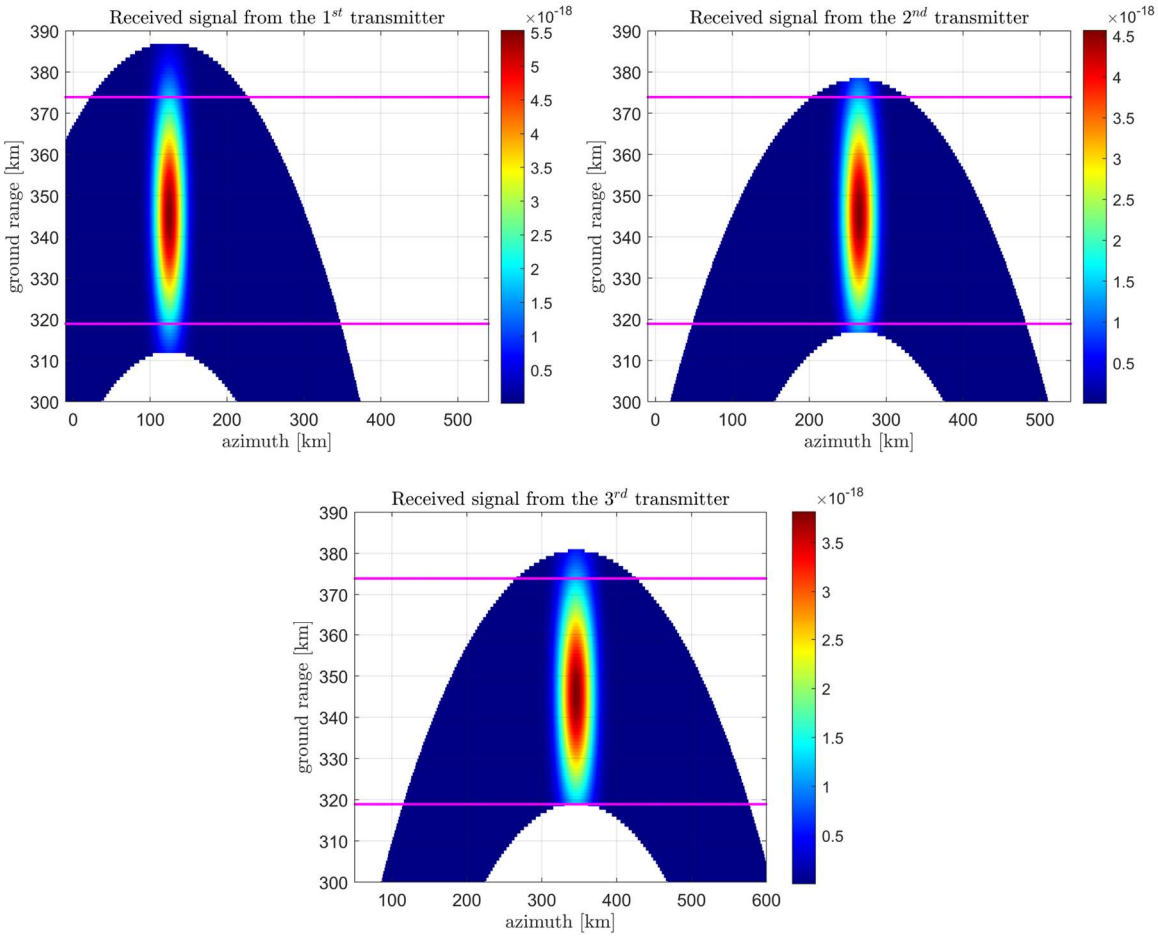

Figure 4.10: Received signals cut at 17 dB

In any case, also with this less strict constraint, it is clear that in this fleet configuration the addition of another illuminator, still using the TDMA scheme, would have been impossible without an unacceptable reduction in the ground swath coverage.

Moreover, the results of the Noise Equivalent Sigma Zero evaluation for each bistatic couple of the presented fleet design, are presented in Figure 4.11.

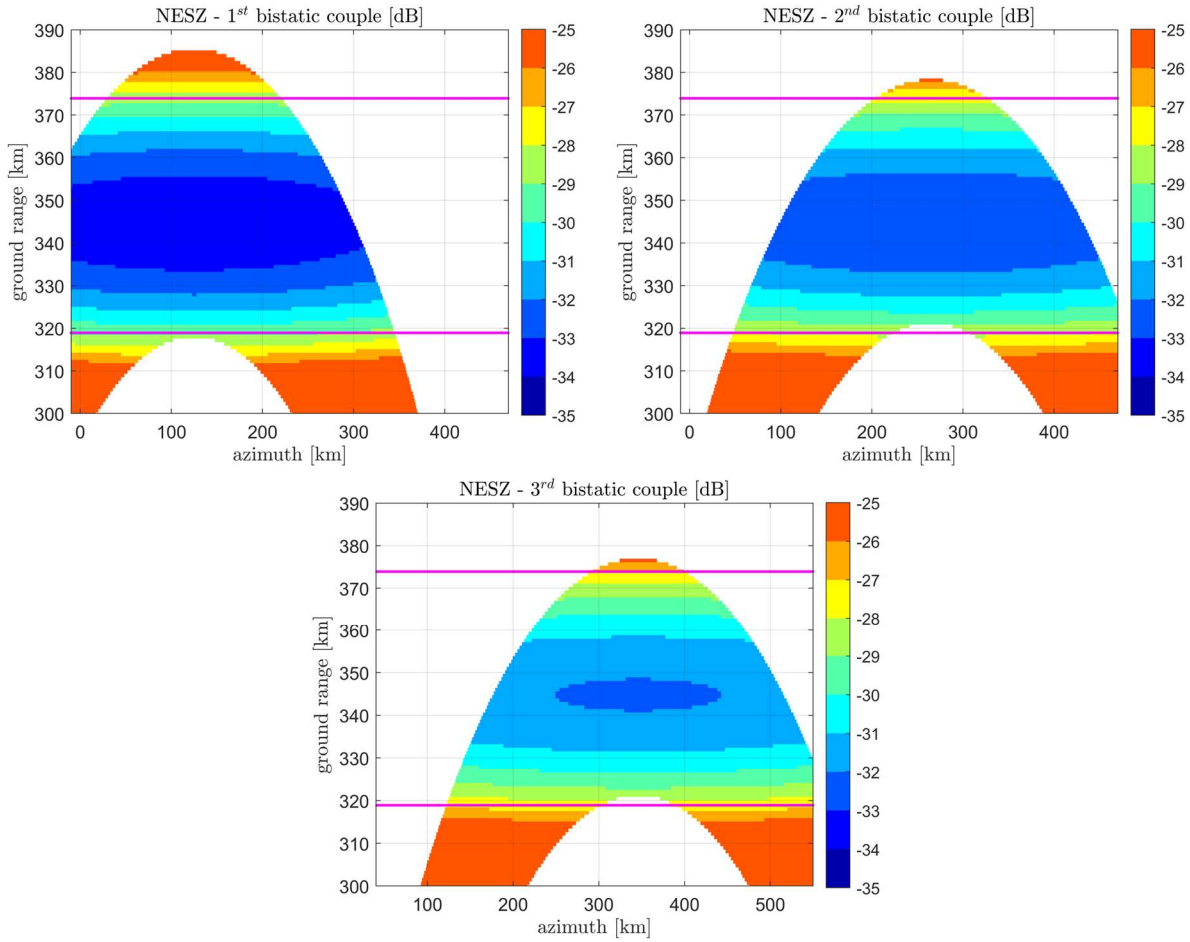

Figure 4.11: NESZ – 1st fleet configuration

In this last figure a zoom on the swath width in the ground range direction has been performed, to stretch the plots and make it easier to verify whether the NESZ constraint has been respected or not. Furthermore, for the same reason, an appropriate colour scale has been selected to make sharper the changes in between the NESZ values. As it is evident the Biomass mission threshold of $-27\ dB$ is not only perfectly respected but it is also surpassed since in almost all the swath the NESZ has a value of around $-30\ dB$ or even better. At this point is worth mentioning that the NESZ computation has been carried out by means of Equation (2.33) applied to the bistatic case, which becomes:

$$\sigma^{NESZ} = \frac{\sin(\theta_{tx}) \cdot N_0 \cdot (4 \cdot \pi \cdot R_{tx} \cdot R_{tx})^2}{\rho_{x_{tx}} \cdot \rho_r \cdot N_\tau \cdot T_g \cdot P_{tx} \cdot G_{tx} \cdot Ae_{rx} \cdot f_{tx_\theta} \cdot f_{rx_\theta}} \tag{4.7}$$

where in the case of the NESZ evaluation, the antenna patterns have been computed only as a function of the elevation θ (therefore they have been marked with the subscript θ), not also of ψ. This means that Equation (4.4) and (4.5) have still been used, but without the terms involving the azimuthal angle. Such simplification can be done since the NESZ is a quantity evaluated within the ground swath, thus it varies with θ only. In Figure 4.12 the plots of f_{tx_θ}, f_{rx_θ} and $f_{tx_\theta} \cdot f_{rx_\theta}$ are shown.

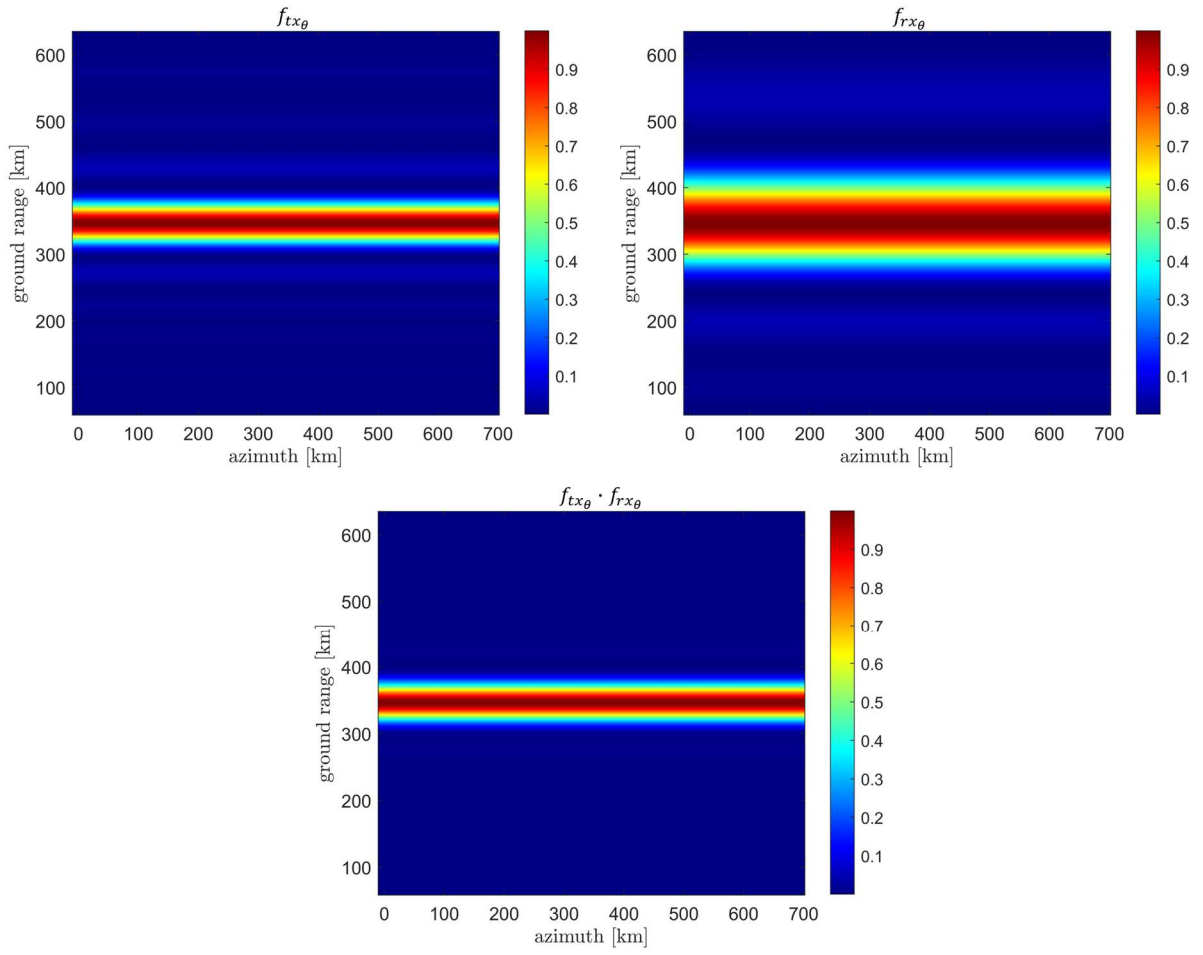

Figure 4.12: Radiation patterns as a function only of θ – 1st fleet configuration

As expected, the plots presented in this last figure show a straight pattern, with no bounds in the azimuth direction. Furthermore, having removed the dependence from ψ, the radiation patterns for all the transmitters results to be exactly the same. Moreover, it can be notice that the pattern of the array is wider than the one of the transmitters, but this was predictable since the beamwidth in elevation of the latter is less than half the one of the receiver.

4.2.4 Second fleet configuration results

In this subsection the second proposed fleet design is presented. With respect to the previous one, this configuration has a smaller array in the elevation direction while the three transmitting satellites have exactly the same features as before, except for the power transmitted.

In Table 4.5 the features of the array designed for this second case are listed.

Lx_{patch}	0.3 m	Azimuthal length of the patch antenna
Lz_{patch}	0.3 m	Elevation length of the patch antenna
N_{patch_x}	8	Number of patch antennas along x
N_{patch_z}	8	Number of patch antennas along z
Lx_{panel}	2.4 m	Azimuthal length of the single panel
Lz_{panel}	2.4 m	Elevation length of the single panel
N_{panel_x}	4	Number of panels along x
N_{panel_z}	1	Number of panels along z
Lx_{array}	9.6 m	Azimuthal length of the array
Lz_{array}	2.4 m	Elevation length of the array
$\Delta\theta_{patch}$	131.62°	Patch antenna elevation beamwidth
$\Delta\theta_{array}$	16.45°	Array elevation beamwidth
$\Delta\psi_{patch}$	131.62°	Patch antenna azimuthal beamwidth
$\Delta\psi_{array}$	4.11°	Array azimuthal beamwidth
ρ_x	4.8 m	Array azimuthal resolution
G	26.30 dB	Array gain
A_e	16.13 m^2	Antenna effective area

Table 4.5: Array parameters – 2nd fleet configuration

Since Lz_{array} is halved with respect to the previous design, the array beamwidth in elevation results to be doubled and, obviously, since the antenna is less directive, the antenna gain and effective area appear to be reduced.

The following results have been obtained by simulating a separation between the receiver and each transmitter as reported in Table 4.6.

1st bistatic couple	TX_1	RX	$L = 250\ km$
2nd bistatic couple	TX_2	RX	$L = 525\ km$
3rd bistatic couple	TX_3	RX	$L = 687\ km$

Table 4.6: Distances between each transmitter and the receiver – 2nd fleet configuration

Moreover, in this case, the needed power in transmission to fulfil the NESZ requirement is $180\ W$ thus, it is higher with respect to the P_{tx} employed in design proposed in the previous subsection. Nevertheless, this was predictable, since in this array configuration the value of the effective area, which is at the denominator of Equation (4.7), is smaller.

Now that all the simulation parameters have been declared, the time is ripe to introduce the simulation results. In Figure 4.13 the plots of the antenna radiation patterns of the transmitting and receiving SAR systems (always computed as stated in Equations (4.4) and (4.5)) are shown together with their combined radiation pattern.

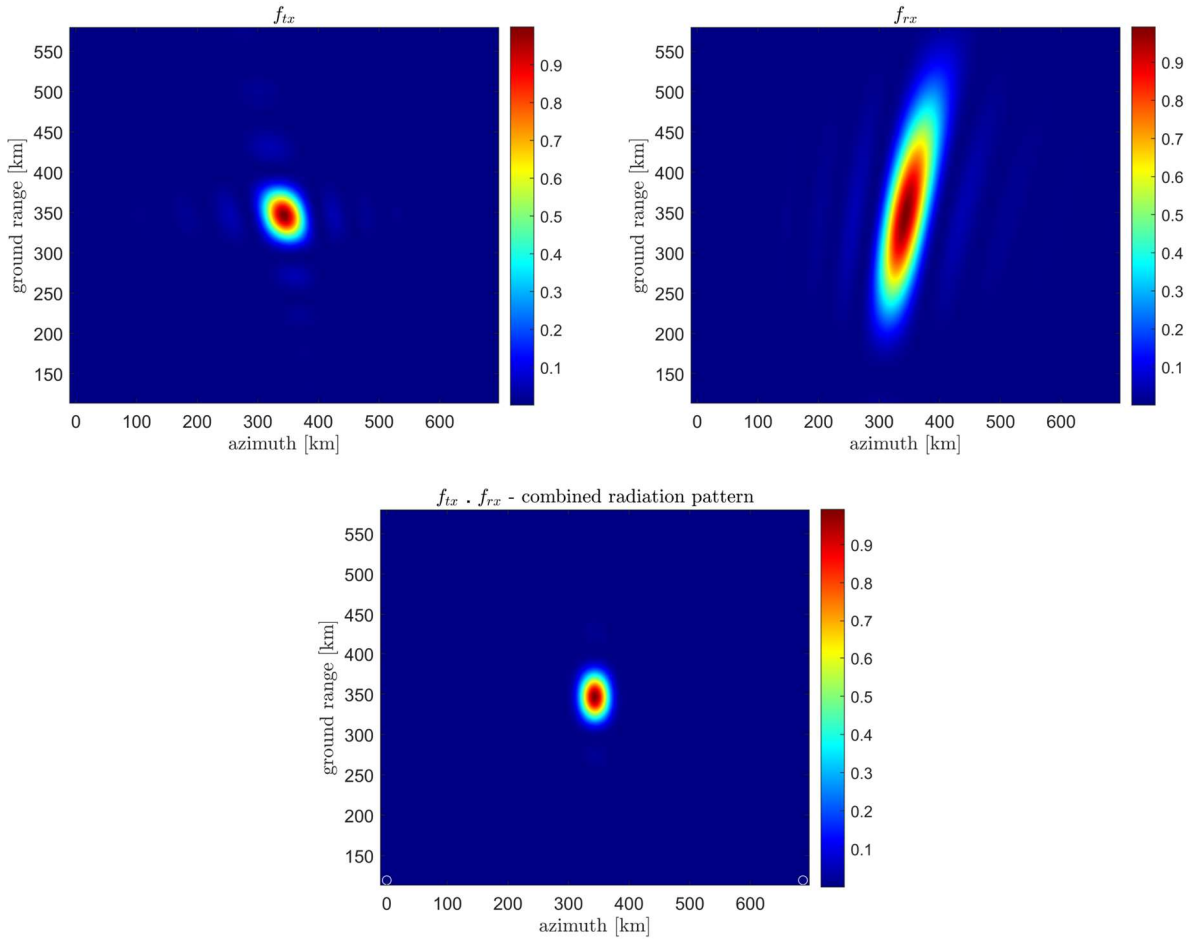

Figure 4.13: Radiation patterns – 2nd fleet configuration

As expected, the receiver pattern is much more stretched in the ground range direction and it can be also noticed that now two sidelobes are visible in the combined radiation pattern.

The power received for each bistatic acquisition is shown in Figure 4.14, always as an image function of azimuth and ground range.

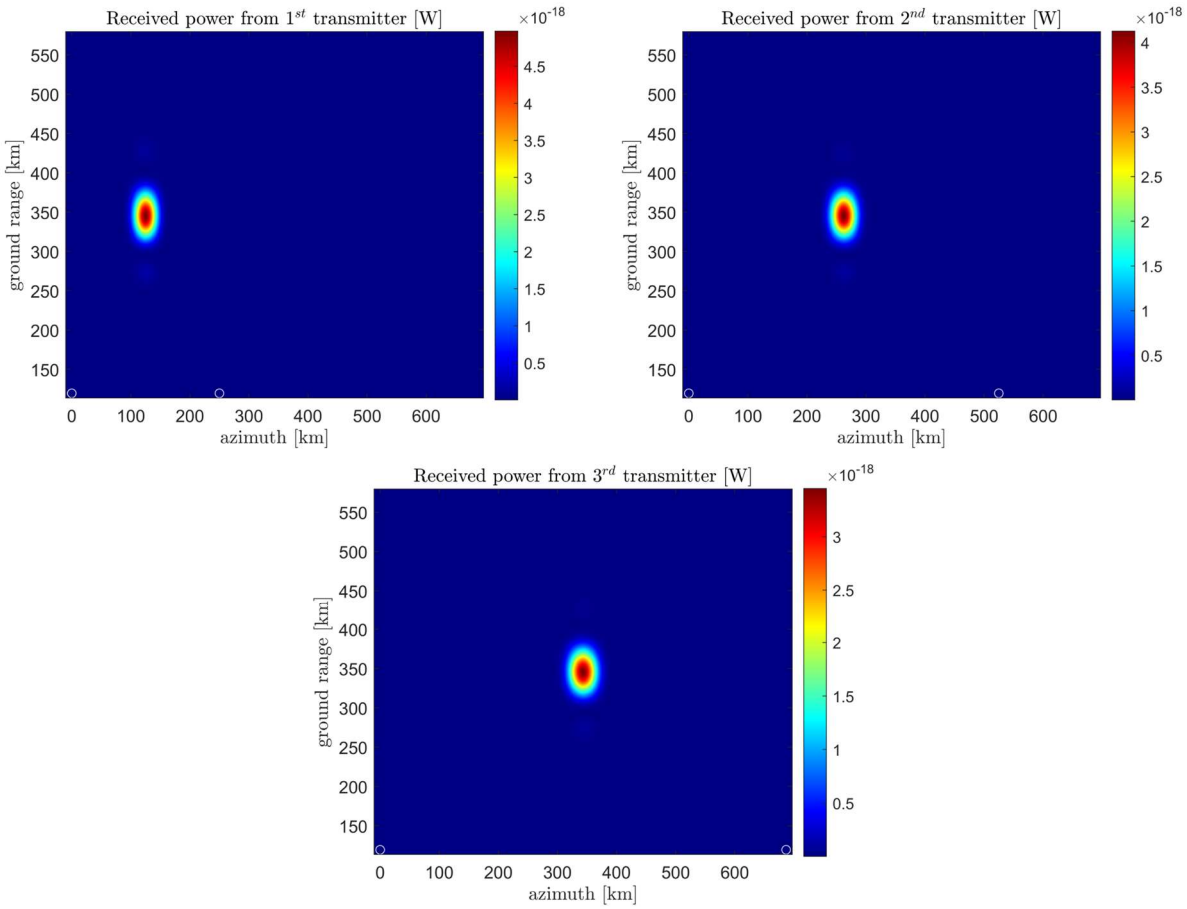

Figure 4.14: Received power – 2nd fleet configuration

At this point, the received power has been plot against the time delay as before, to see the result of the beam steering procedure. In Figure 4.15 the three plots for the three array pointings are shown, as in Subsection 4.2.3.

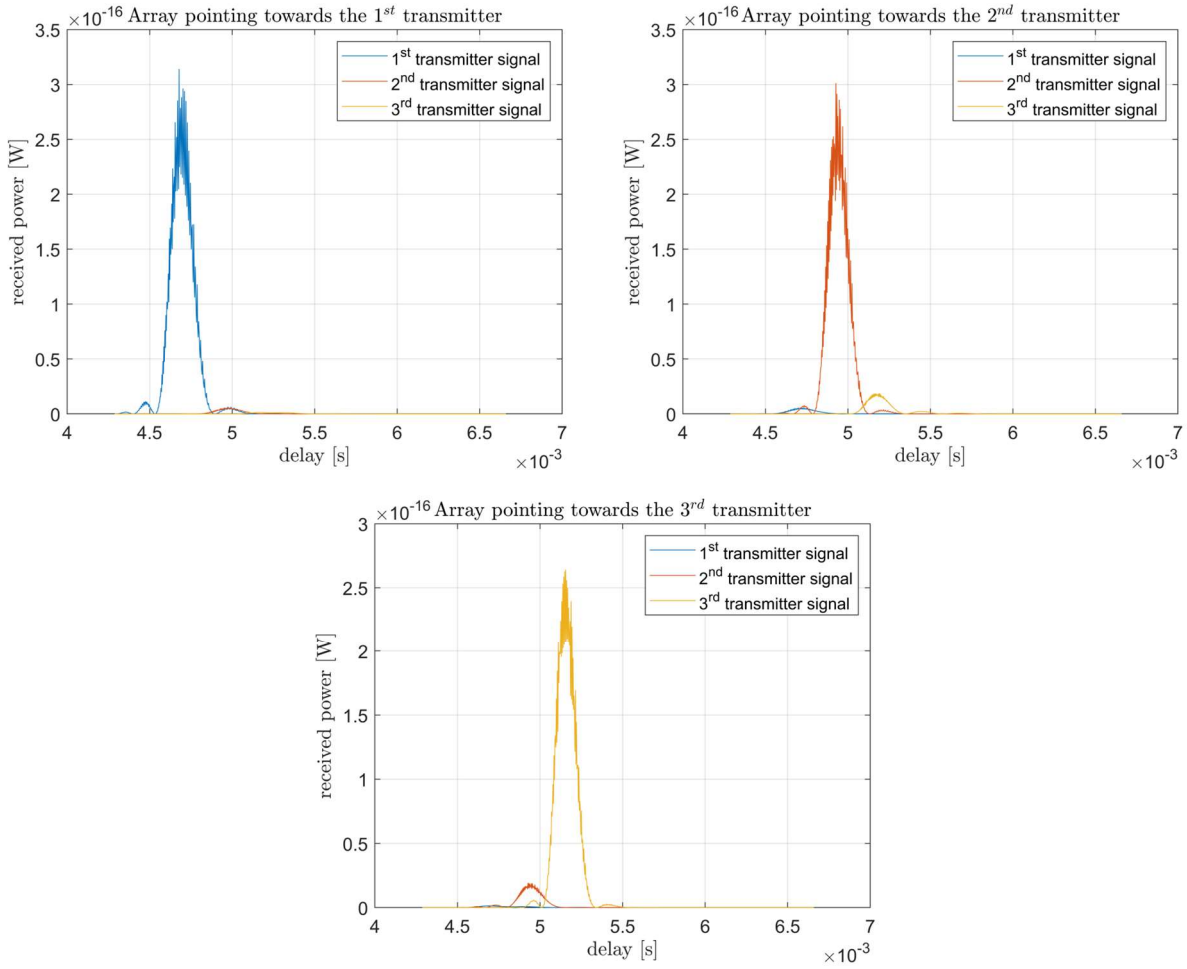

Figure 4.15: Received power Vs time delay – 2nd fleet configuration

Also by looking at the 1D plots of the power, presented in this last figure, it is clear that the presence of the sidelobes in this design is much more evident than before.

Then, the same procedure shown for the previous design has been implemented to find the cutting points, which are shown, together with the received signals power expressed in $[dB]$, in Figure 4.16.

(a)

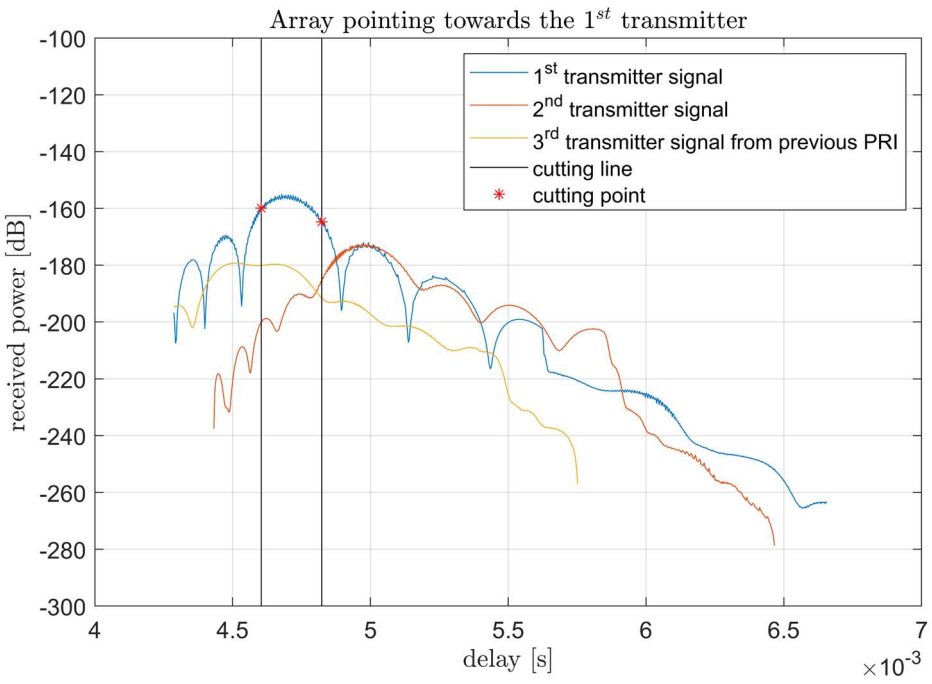
Array pointing towards the 1st transmitter
1st transmitter signal
2nd transmitter signal
3rd transmitter signal from previous PRI
cutting line
cutting point
received power [dB]
delay [s]
×10-3

(b)

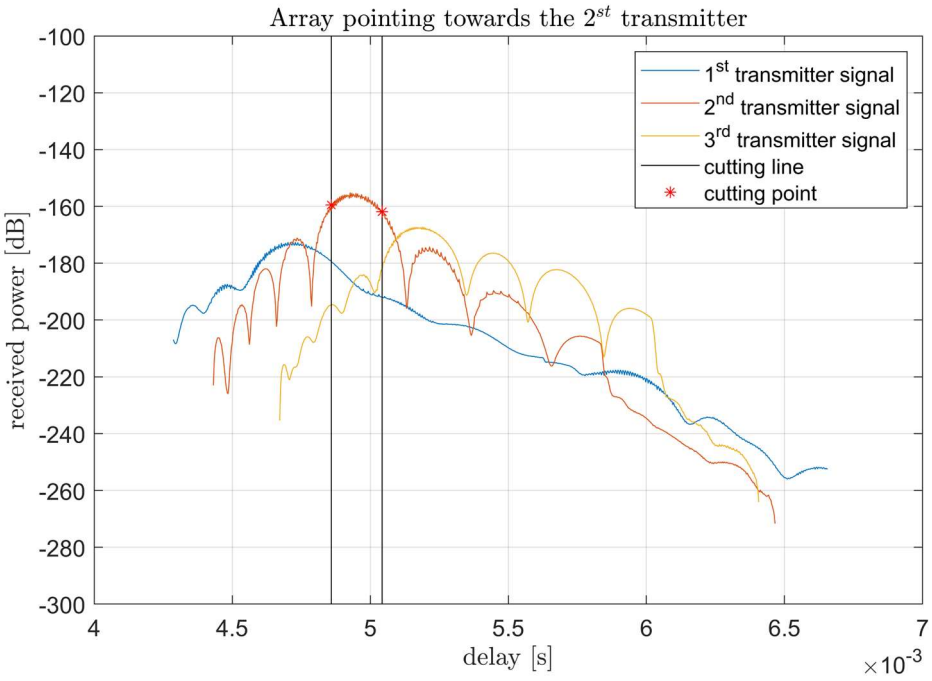
Array pointing towards the 2st transmitter
1st transmitter signal
2nd transmitter signal
3rd transmitter signal
cutting line
cutting point
received power [dB]
delay [s]
×10-3

(c)

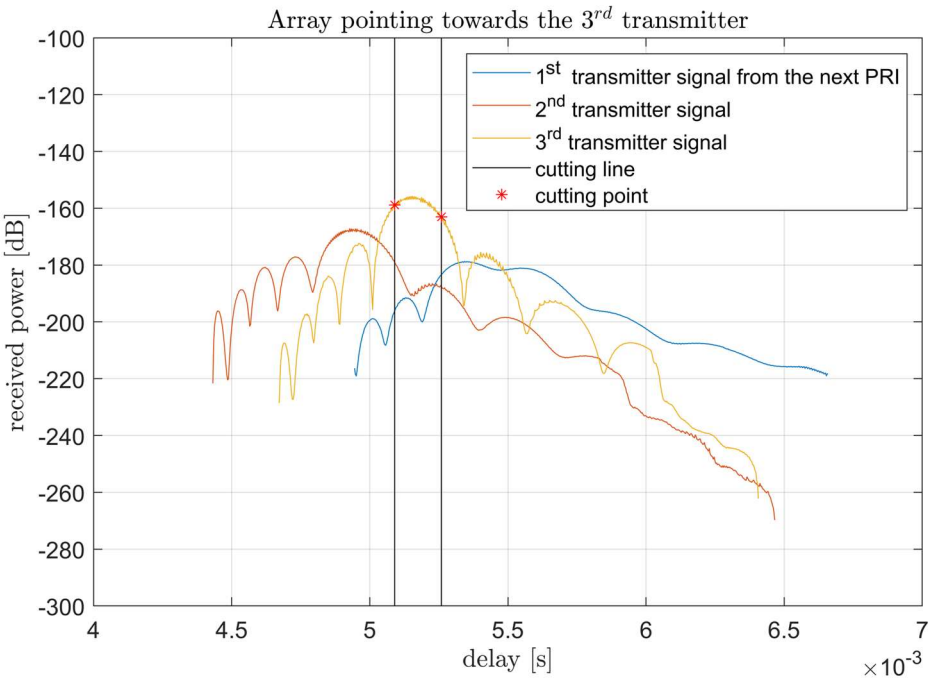

Figure 4.16: Signals' cutting – 2nd fleet configuration

Also in this case the cutting points have been chosen as the points in which the difference between the signal and the interference from the other beams becomes equal to $20\,dB$. Moreover, as for the previous configuration, the interference (or noise) for each array pointing is represented by the signal coming from the illuminators towards which the array is not steered in that moment.

Then, to be able to evaluate the effect of this cutting procedure on the ground swath, the received power plots after the cut are shown in Figure 4.17.

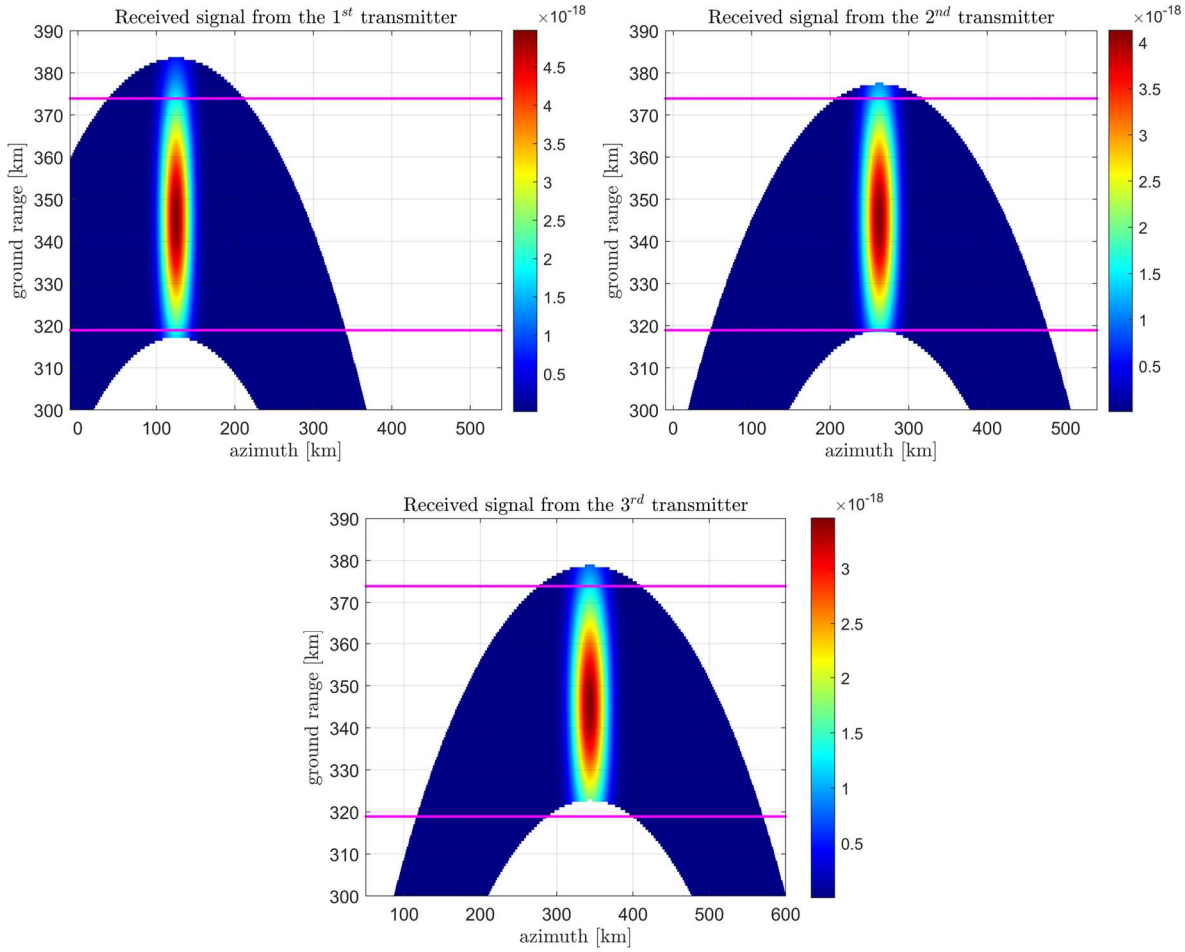

Figure 4.17: Cut received signals magnification – 2nd fleet configuration

The plots presented in Figure 4.17 are again magnified and limited by the usual magenta lines representing the boundaries of the 55 km transmitters' ground swath (see Table 4.2). It can be noticed that also in this case the ground swath of the illuminators results to be not fully covered after the cutting procedure, in particular by looking at the signal received from the third transmitter it is clear that the system is not capable of illuminating all the 55 km ground swath. Nevertheless, also this fleet design has been optimized in terms of signals' overlap, in fact the swath loss is of just 4 km, thus it is possible to establish that the presented MultiSAR configuration is capable of imaging a ground swath of 51 km.

Furthermore, the results of the Noise Equivalent Sigma Zero evaluation for each bistatic couple of the presented fleet design, are presented in Figure 4.18.

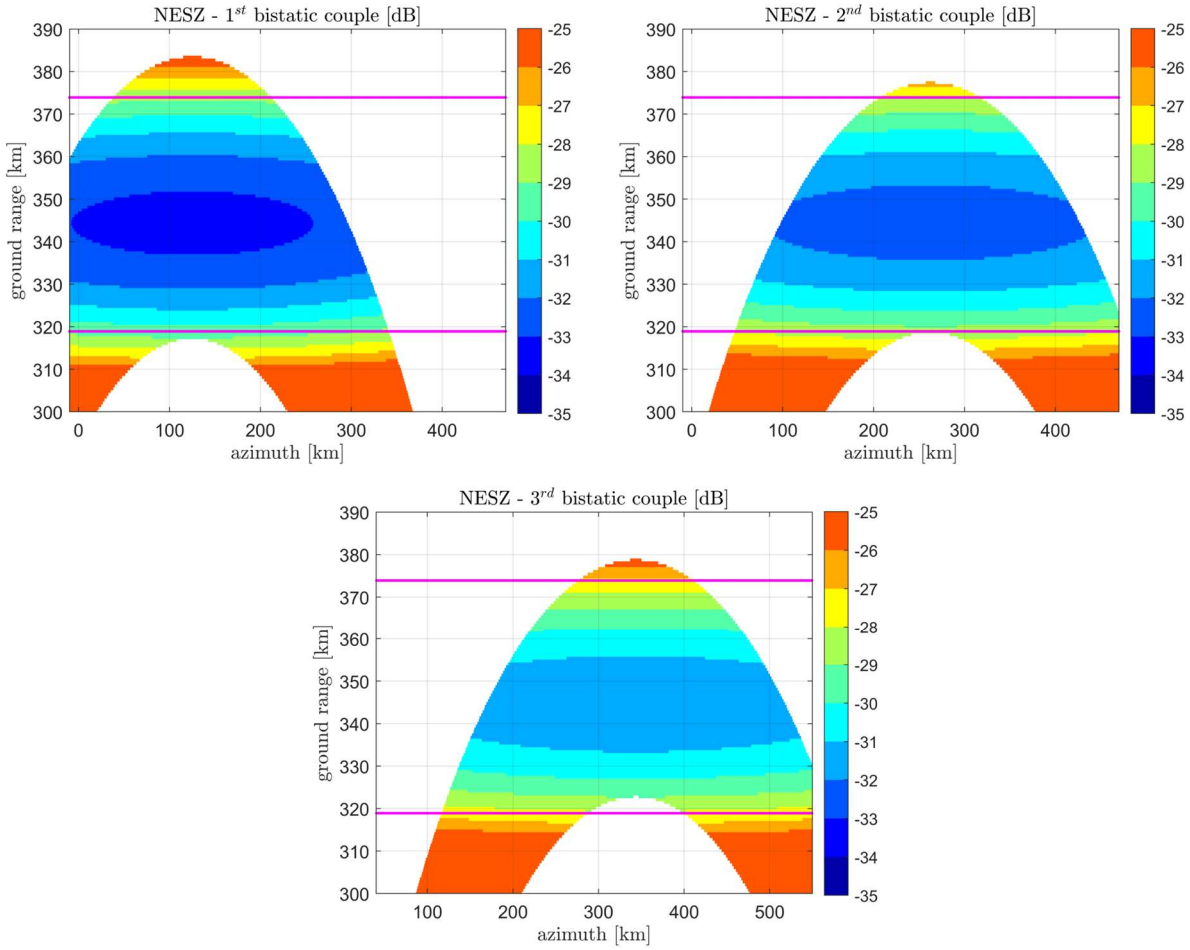

Figure 4.18: NESZ – 2nd fleet configuration

In this last figure, as in the previous subsection, a zoom on the swath width in the ground range direction has been performed, to stretch the plots and make it easier to verify whether the NESZ constraint has been respected or not. Furthermore, the NESZ computation has been carried always out by means of Equation (4.7) and always evaluating the antenna pattern only as a function of the elevation angle. Also in this case it is evident that the NESZ is always better or at least equal to the threshold value of $-27\ dB$, indeed in the vast majority of the ground swath its value is around $-30\ dB$. It has to be remarked that, as expected, due to the smaller G and A_e, the NESZ appears to be lower than in the previous case, even if a higher transmitted power has been employed.

In Figure 4.19 the plots of the radiation patterns employed for the NESZ evaluation are shown.

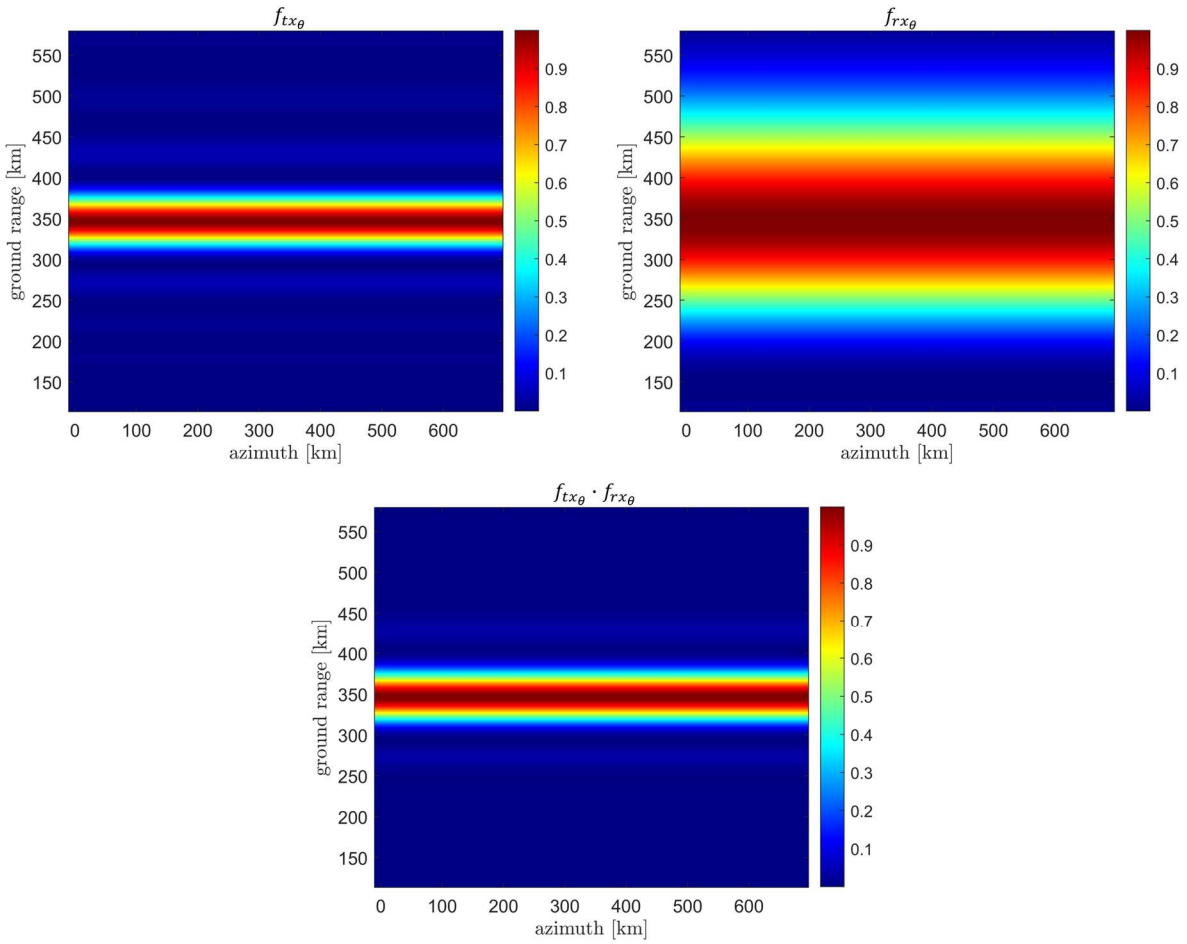

Figure 4.19: Radiation patterns as a function only of θ – 2nd fleet configuration

From these last plots, it can be notice that the radiation pattern of the array is remarkably wider with respect to the one of the transmitters, but this was predictable since the receiver beamwidth in elevation is now almost four time larger than the one of the transmitting parabolic antennas.

In conclusion, this array configuration is for sure lighter and smaller than the one presented in Subsection 4.2.3, because the array dimension has been halved in the elevation direction, but this MultiSAR design requires almost twice the power in transmission and it also presents worst results in terms of swath coverage and NESZ (still fulfilling the Biomass requirement). Nevertheless, the loss in terms of ground swath coverage is only of two kilometres greater than in the previous configuration, so it seems to be not so relevant. In any case, in the following subsection, an evaluation of the MultiSAR fleets Earth coverage performance is presented, and it is also shown how this swath loss impacts on the time required to achieve the coverage of some interesting Earth areas.

4.2.5 Earth coverage

Having seen the performance of the two proposed MultiSAR fleet designs in terms of ground swath coverage, it is interesting to compute how long the SAR constellations take to image a certain Earth area. As deeply explained in Chapter 1, a P-Band SAR mission like the ones proposed in this thesis, can be exploited to give essential information about the carbon cycle by analysing the forests, thanks to the P-Band penetration capability.

For this reason, it can be worthwhile to roughly evaluate the time needed to image the Amazon Forest, which is both the "green lung of the Earth" and a huge carbon sink. To do so, it is necessary to introduce the simulation parameters which have been used for this computation. The latter are presented in Table 4.7.

H	$600\ km$	Orbital height
$\mu_{\oplus}$	$3.986 \times 10^5\ km^3/s^2$	Earth's gravitational parameter
$R_{\oplus}$	$6371\ km$	Earth's equatorial radius
$L_{x,forest}$	$2500\ km$	Approximated Amazon Forest extension in the latitude direction
$L_{y,forest}$	$4000\ km$	Approximated longitudinal Amazon Forest extension
T_{active}	$12\ min$	Fully operational mode duration for each orbit

Table 4.7: Simulation's parameters for Earth coverage computation

Since the orbit has been assumed to be circular (as explained in Section 4.1), the orbital radius has been simply evaluated as $r_{orb} = R_{\oplus} + H$ and the constant orbital speed, according to [34], has been computed as:

$$v = \sqrt{\frac{\mu_{\oplus}}{r_{orb}}} = 7.56\ km/s \tag{4.8}$$

where the value of $\mu_{\oplus}$ is the one presented in Table 4.7, and it has been taken from [35]. Then the orbital period T_{orb}, has been calculated, always following [34], as:

$$T_{orb} = 2\pi \sqrt{\frac{r_{orb}^3}{\mu_\oplus}} = 5.7923 \times 10^3 s \cong 1h\ 37min \tag{4.9}$$

Moreover, since the designed SAR fleets are supposed to be in fully operational mode for 12 minutes (typical value, also used in [36]), meaning that the systems are acquiring data only for around the 12 % of the orbital period, it is necessary to evaluate how many kilometres are covered during this time interval, along the orbital path. This computation has been carried out, by using T_{active} in $[s]$, as:

$$x_{active} = v\, T_{active} = 5444.4\ km \tag{4.10}$$

where this parameter has been indicated as x_{active} in order to emphasize that it is a measure taken along the SAR azimuthal direction. Thus, since the approximated Amazon Forest extension in the latitude direction is $2500\ km$ and the selected orbit is near polar (for the reasons explained in Section 4.1), it is possible to state that in 12 minutes the designed SAR constellations are fully capable of imaging all the forest length, if they are activated when passing on the Amazon Forest latitudes.

On the other hand, to roughly evaluate how many days the SAR fleets require to image all the Amazon Forest width in the longitudinal direction, it has been computed the drift suffered by the fleets after each orbital period, due to the Earth rotation. Indeed, neglecting all the orbital perturbations, after one orbital period the satellites will be at the same latitude but translated in the longitudinal direction of a certain quantity y_{drift} (measured in $[km]$), due to the Earth rotation around its own axis. This parameter has been computed as:

$$y_{drift} = y_{rotation}\, T_{orb} = 2683.7\ km \tag{4.11}$$

where T_{orb} is used in $[s]$ and the just calculated value has been indicated as y_{drift} in order to highlight the fact that it is a measure in the ground range direction, since the considered orbit is almost polar. The same reasoning has been applied to $y_{rotation}$, which instead indicates of how many kilometres the Earth rotates per second. Indeed, approximating the Earth rotation around its axis as exactly $360\,°/day$, $y_{rotation}$ has been estimated as the Earth circumference divided by the seconds which form a day, namely:

$$y_{rotation} = \frac{2\,\pi\, R_\oplus}{24 \times 3600} = 0.4633\,\frac{km}{s} \tag{4.12}$$

where $R_\oplus$ is the one presented in Table 4.7, and it has been taken from [37].

At this point, to compute how long the fleets take to cover $L_{y,forest}$, the parameter p_f has been computed as:

$$p_f = 1 + \frac{L_{y,forest}}{y_{drift}} \tag{4.13}$$

where p_f indicates how many times, due to the Earth rotation, the considered fleet passes on the Amazon Forest each day and the term $(1+)$ has been used since the constellations are supposed to start their acquisition at the beginning of the Amazon Forest longitudinal width. It must be remarked that, obviously, p_f has to be rounded to the smallest close integer number.

Then y_{day}, which represents the kilometres of Amazon Forest imaged each day, has been computed by means of:

$$y_{day} = p_f \, W \tag{4.14}$$

where W is the ground swath covered by the considered SAR fleet. Finally, it is possible to compute how many days the MultiSAR formation needs to image the Amazon Forest, as:

$$coverage_{AMAZON} = \frac{L_{y,forest}}{y_{day}} \tag{4.15}$$

where, of course, this result has to be rounded to the higher close integer number.

The exact same reasoning can be applied to compute in how many days the SAR constellations are able to cover all the equatorial belt. The only change with respect to the previous computations is that now, in the p evaluation, $L_{y,forest}$ must be replaced with the Earth equatorial circumference, namely $2\,\pi\,R_{\oplus}$, leading to:

$$p_e = 1 + \frac{2\,\pi\,R_{\oplus}}{y_{drift}} \qquad\qquad y_{day_2} = p_e \, W \tag{4.16}$$

where, it can be noticed that $\frac{2\,\pi\,R_{\oplus}}{y_{drift}}$, represents the number of orbits completed by the fleet each day. Having defined the p_e and y_{day_2}, the days needed to cover the equatorial area are computed as:

$$coverage_{EQUATOR} = \frac{2\,\pi\,R_{\oplus}}{y_{day_2}} \tag{4.17}$$

where, being also this result given in days, it has to be rounded as for Equation (4.15). Of course, the width of the covered equatorial belt in the latitude direction is equal to x_{active}.
The results of the last operations have not been given numerically in the just presented equations, since they are listed, for the 3 different W values encountered in the previous subsection, in Table 4.8.

W	$coverage_{AMAZON}$	$coverage_{EQUATOR}$
55 km	37 days	49 days
53 km	38 $days$	51 days
51 km	40 days	53 days

Table 4.8: Earth coverage simulations' results

4.3 Range resolution enhancement via MWT

As explained in Subsection 4.1.1, the results shown in Section 4.2 have been obtained by selecting the separations between the receiver and the transmitters which allows the best possible performance in terms of TDMA, namely the minimum possible overlap between the signals in reception. Nevertheless, as it was predictable, these L (shown in Table 4.4 and 4.6) are not the ones which guarantee the optimal tessellation, that is necessary to achieve the desired range resolution enhancement via MWT. In any case, as mentioned in Subsection 4.1.1, this problem can be easily solved by letting the illuminators transmit their signals with some delay one with respect to the other.

Indeed, having evaluated the delay with which each signal must reach the receiving array to optimize the TDMA implementation, the transmission scheme can be regulated according to these delays, which are shown in Table 4.9.

Transmitter	2	3
Delay w.r.t. the previous received signal for the 1st fleet configuration	$2.78 \times 10^{-4} s$	$1.82 \times 10^{-4} s$
Delay w.r.t. the previous received signal for the 2nd fleet configuration	$2.49 \times 10^{-4} s$	$2.28 \times 10^{-4} s$

Table 4.9: Delays needed to implement the TDMA scheme

In this last table, the delays for the two designed fleet configurations are listed. For instance, in the fleet design presented in Subsection 4.2.3, the signal emitted by the second transmitter must reach the receiver after $2.78 \times 10^{-4} s$ from the reception of the first one, while the signal from the third illuminator has to reach the array after $1.82 \times 10^{-4} s$ from the

reception of the signal coming from the second transmitter. Of course, the same reasoning can be applied to the second row of Table 4.9, in which the resulting delays for the second MultiSAR configuration, presented in Subsection 4.2.4, are reported.

By enforcing a proper synchronization plan among the transmitters based on the presented delays, the performance of the designed fleets remains exactly the one presented in Subsection 4.2.3 and 4.2.4, even if the distances L change. Thus, once the transmission scheme is regulated according to these delays, the backscattered signals reach the receiver as shown in the previous section, therefore with the same small overlap, even if the separations among the satellites are different. This allows to set the orbital distances between the SAR systems taking into account only the MTW. Exploiting the simulator presented in Section 3.3, the distances between the array and each illuminator, which allow a perfect tessellation, have been found to be the ones presented in Table 4.10, for both the fleet configurations.

1st bistatic couple	TX_1	RX	$L = 250\ km$
2nd bistatic couple	TX_2	RX	$L = 360\ km$
3rd bistatic couple	TX_3	RX	$L = 450\ km$

Table 4.10: Distances needed to perform the MWT

Employing these separations, the resulting wavenumber coverage map for the MultiSAR fleets, always evaluated by means of the simulator, is shown in Figure 4.20.

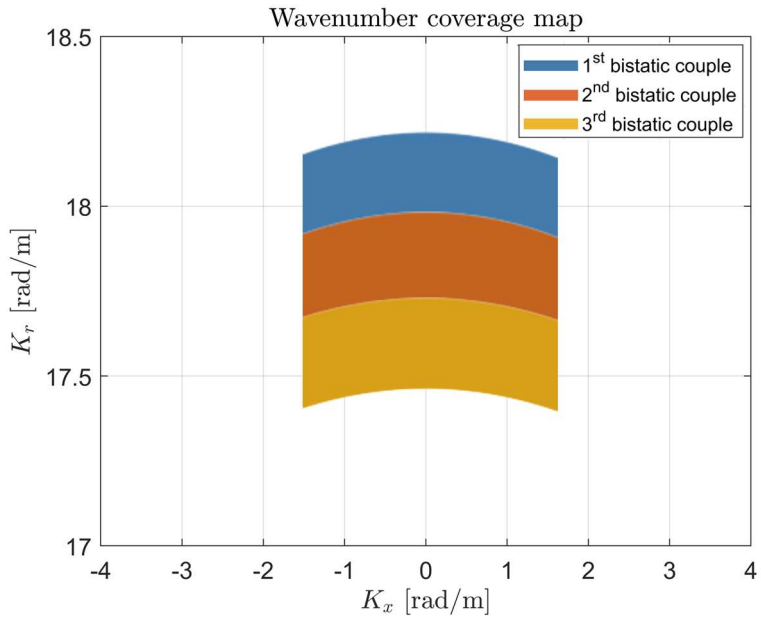

Figure 4.20: Wavenumber coverage map for the designed fleets

From this last figure the virtual bandwidth extension obtained via MWT is really evident, indeed the range wavenumber coverage results to be tripled with respect to the monostatic P-Band SAR case (see Figure 3.10). As discussed in Chapter 3, a tessellation like the one presented in Figure 4.20 allows to achieve a remarkable spatial resolution enhancement, despite the imposed real bandwidth of just $6\ MHz$.

Moreover, it has to be highlighted that the eyeglass diagram, shown in Figure 4.20, has been obtained by simulating the real fleets' orbital height of $600\ km$. Indeed, as explained in Chapter 3, the evaluation of the wavenumber coverage maps is far less computationally heavy to be obtained with respect to the calculation of the system IRF. The latter is a massive advantage, that has allowed to develop the presented fleet designs without the need of computing the real IRF, which would have been computationally impossible to perform with a common laptop at those frequencies and at the real orbital altitude. Indeed, by looking at Figure 4.20, the obtained range resolution enhancement is already quantifiable, since it is proportional to the number of employed bistatic couples if a proper tessellation, as the presented one, is performed.

In any case, the IRF of the MultiSAR fleets has been computed through the developed *MATLAB* simulator, but of course relying on the usual fictitious orbital height of $10\ km$, as in Chapter 3. Nevertheless, this variation greatly reduces the computing times but does not affect the validity of the principles upon which the whole work is based.

Thus, the obtained range resolution improvement can be appreciated by looking at Figure 4.21, in which the approximated Impulse Response Function of the Biomass mission is compared with the IRF resulting from the tessellation presented in Figure 4.20.

(a)

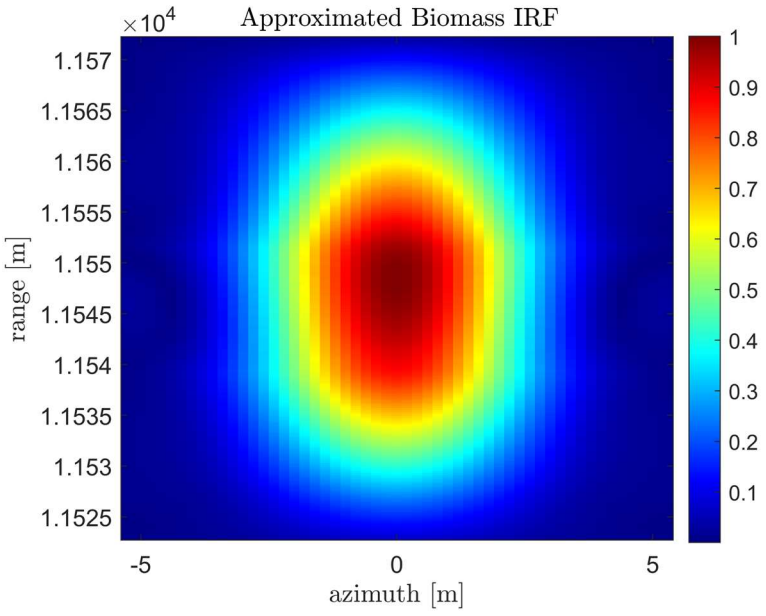

(b)

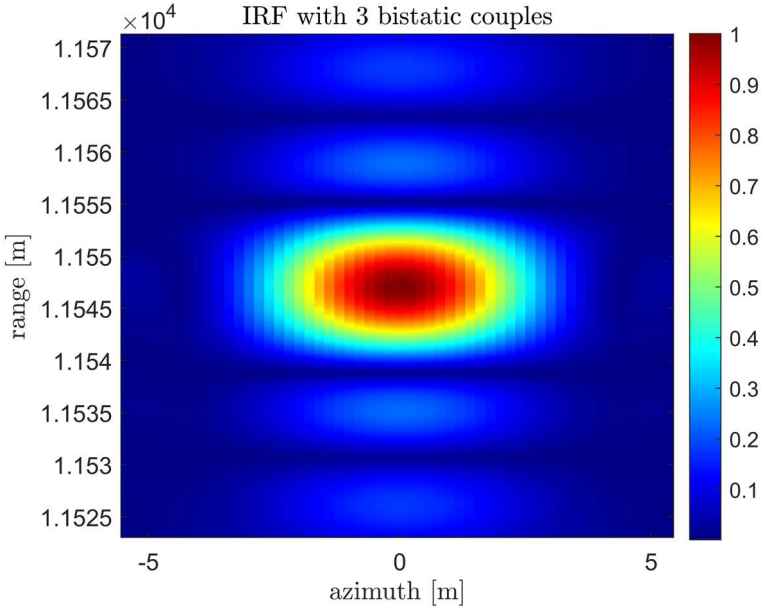

Figure 4.21: Approximated Biomass IRF and IRF of the designed fleets

As it can be noticed, by employing 3 bistatic couples the obtained effect is equivalent to have a three times larger available bandwidth. Indeed, the same result as the one presented in Figure 4.21 (b) can be retrieved by simulating a system with the same specifications of Biomass except for a larger bandwidth of 18 MHz. Furthermore, it is better to point out that the plots in Figure 4.21 have been magnified, in order to make it possible to read clearly the achieved resolution improvement.

These IRF have been evaluated with the simulator presented in Section 3.3, so of course the IRF of the ESA Biomass mission is just an approximation. Nevertheless, the real IRF of Biomass can be visualized in Figure 4.22.

(a)

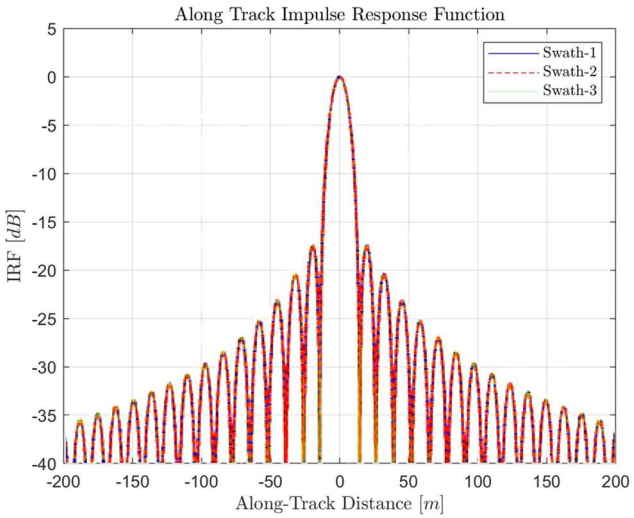

(b)

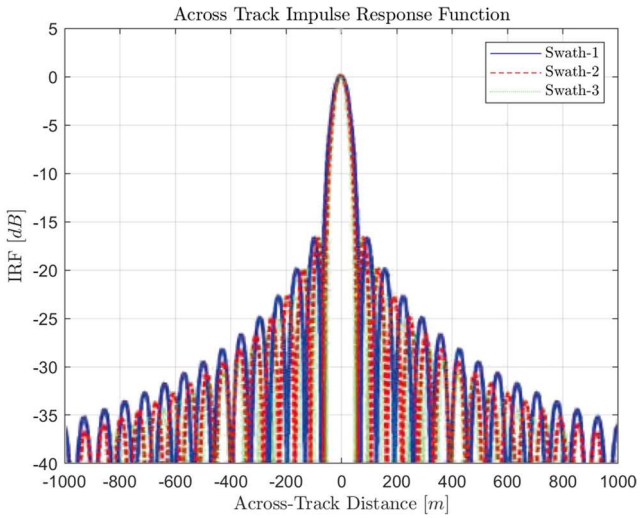

Figure 4.22: Real Biomass IRF @ESA

In these last plots the real Biomass Impulse Response Function in the along-track and across-track dimensions are presented. It can be noticed that in the legend three different swaths are mentioned, this is due to the fact that three different illuminating beams have been devised for Biomass, featuring increasingly gentler pointing angles θ_0. This different pointing results in differently illuminated swaths and it also translates the range resolution $\rho_r = 24.98\,m$ into progressively larger ρ_y resolutions (see Equation (2.16)).

Chapter 5
Discussion and conclusions

In this thesis, it is proposed a multi-static solution to remarkably enhance the SAR systems imaging capabilities without increasing the transmitted bandwidth, which is constrained by the ITU regulations. Indeed, in this dissertation a strategy to obtain a finer range resolution by exploiting multiple bistatic acquisitions is illustrated and its effectiveness is confirmed by the results coming from the two promising and feasible multi-static SAR fleet designs which have been developed.

As examined in Chapter 1, the enhancement of the spatial resolution results to be particularly attractive for the P-Band missions which are strongly limited by the $6\,MHz$ bandwidth availability, that leads to the very coarse range resolution of $24.98\,m$. Nevertheless, exploiting the P-Band penetration capability it is possible to give a significant contribution to the fight against climate change, in particular by improving the understanding of the global carbon cycle and also reducing the uncertainties in the calculations of carbon stocks and fluxes associated with the terrestrial biosphere. Indeed, the atmosphere-terrestrial biosphere carbon flux is not explicitly measured at present, but it is obtained indirectly by subtracting from the atmospheric carbon increase the contributions of fossil fuel combustion and those of the ocean, leading to an extremely high uncertainty level. Moreover, the long P-Band wavelength is also a precious resource to study the near-subsurface region not only of the Earth, but also of planetary bodies including the Moon, Mars, Mercury, Venus, comets, icy moons and asteroids, which is an investigation that, nowadays, is of high interest for future human or robotic explorers. Nonetheless, even if at present the P-Band SAR missions could represent the solution to many scientific problems, they are not exploited yet, due to their great drawback, namely the aforementioned poor range resolution.

Therefore, in light of the ESA Biomass mission and of the NASA JPL SESAR project (both described in Chapter 1), the ultimate goal of this thesis is to propose a novel multiple bistatic technique to overcome the resolution shortcomings due to ITU bandwidth regulations.

Indeed, this dissertation leverages the Multi-static Wavenumber Tessellation principle proposed in [23] and derived from the Fundamental Equation of Diffraction Tomography, as deeply detailed in Chapter 3. The MWT is based on the virtual extension of the real SAR bandwidth, by enriching the observed wavenumbers though a proper combination of the acquisitions coming from different bistatic couples, thus from different squint angles.

In particular, the intent of this thesis, is to develop the theoretical and computer tools aimed to deal with the multi-static SAR fleet design and the exploitation of the just mentioned MWT concept. By means of these instruments, two relevant SAR constellations have been designed, featuring one receiver and three transmitters, whose relative simulations' results and performance evaluation are shown in Chapter 4.

To perform the design of these SAR formations, one very challenging aspect was the implementation of a suitable transmission scheme. In the presented configurations, the transmitters have been assumed to operate under the principle of Time Division Multiple Access (detailed in Chapter 4), thus the transmission scheme has been implemented by enforcing a proper synchronization plan among the transmitters.

As it is evident by looking at the results presented in Chapter 4, the developed tools have allowed to design two really interesting P-Band multi-static SAR fleets, characterized by a relevant range resolution enhancement, high performance in terms of NESZ and good results also with respect to the ground swath coverage. Indeed, the designed MultiSAR formations, while operating with the usual $6\,MHz$ bandwidth, exhibit the range resolution typical of systems with a three times larger bandwidth, which is a quite satisfying result. Furthermore, another strength of the presented fleet designs is that, while still providing a remarkable NESZ of around $-30\,dB$ in all the imaged swath of more than $50\,km$, they require very low power in transmission (namely $100\,W$ and $180\,W$), even employing a quite small receiving array in reception.

The number of satellites in transmission has been decided by taking into account the formation complexity and cost, and the desired performance. Indeed, the addition of another illuminator would have led to a great loss in terms of ground swath, since by using the TDMA scheme all the received echoes have to fit in the length of the transmitters' PRI in order to avoid range ambiguities.

Moreover, in these two designs the TDMA has been applied by considering a very strict requirement: the received signals have been cut $20\,dB$ above the interference from the other beams, thereby ensuring an exceptional signals separation and interference rejection.

In any case, the two configurations, proposed in Chapter 4, for the MultiSAR constellation, are just two feasible and particularly promising designs among infinite possibilities. Indeed, due to the presence of a huge quantity of design variables, according to the different requirements that one may have, it is possible to obtain totally different design solutions by means of the same proposed theoretical and computer tools. In fact, it is worth highlighting that the *MATLAB* tools presented in this thesis can be adapted to test a huge variety of fleet designs, with different number of transmitters, bandwidth, center frequency, swath, etc… in other words all the parameters shown in Table 3.1, 4.1, 4.2, 4.3 and 4.5 can be changed to evaluate the performance and the tessellation results of completely different fleets, still using the same codes.

Moreover, another important advantage of the presented strategy is that the range resolution improvement obtained via MWT, does not require to focus the acquired image to be verified or quantified. Indeed, being due to the virtual bandwidth extension, it can be easily checked by inspecting the tessellation on the wavenumber coverage map, which is far less computationally heavy to be obtained, because it only needs the targets positions with respect to the SAR system to be evaluated. The latter is a great advantage, that has allowed to develop the presented fleet designs without the need of computing the real IRF, which would have been computationally impossible to perform with a common laptop at those frequencies and at the real orbital height.

The concepts introduced by this thesis represent for sure an ambitious novelty, indeed employing a P-Band multi-static SAR formation would not have been even conceivable until few years ago, but at the present time there has been a growing market interest in P-Band spaceborne SAR applications. Indeed, in this field the NASA JPL project proposed in [10] and the studies illustrated in [23], [32] and [26] show encouraging results, demonstrating that, in the next future, a scenario like the one illustrated in this thesis can become reality.

Moreover, moving from theory to practice, the very first question to be discussed is the validity of the weak reflectivity hypothesis for scenarios of interest at P-Band, namely forests, ice, desert sands [7]. Indeed, the foundation of the Multi-static Wavenumber Tessellation principle is the Born weak scattering approximation, which needs to be tested through specific studies, concerning both forward modeling and propaedeutic SAR campaign data analysis. Nonetheless, it is better to underline that several P-Band SAR campaigns have already been carried out, specifically in the field of bistatic SAR, for instance encouraging findings have been reported, in [25]. Furthermore, even if it is undeniable that the Born approximation does not hold for every scenario, concerning the usage of SAR for biomass investigation, also the results observed in bistatic SAR surveying of forested areas in Northern Europe are promising, as illustrated in [24] and [25].

In addition, further iterations of the proposed designs should definitely look into the effects produced both by Earth's rotation and curvature. Indeed, given the distances employed between transmitters and receiver, the curvature of the path would produce remarkable distortions with respect to the assumed straight trajectory, thus the satellites' separation would have to be carefully tracked to properly implement the MWT and the TDMA, as well as to perform a correct image focusing. Luckily, substantial literature already exists on the subject, in fact a relevant example of assessment and compensation of the effects of Earth's curvature and rotation can be found in [38]. Moreover, also the orbital perturbations should be considered in further developments, in order to evaluate exactly the satellites ground tracks and their time evolution. In this way it would be possible to deliver a much more precise estimation of the time required by the fleet to cover the Amazon Forest or any other area of interest on the Earth surface, or also on any other celestial body.

Furthermore, it may be worth to perform a quantitative comparison, in terms of NESZ, between the results obtained in this thesis and the ones achievable by employing the approach based on the simultaneous transmission of all the satellites, proposed in [32].

To conclude, the just described enhanced definition of the imaging products, could also be applied in the SAR tomography field, by adding other receivers on different orbits. This technique, paired with the superior penetration capabilities of the P-Band, could bring novel insight on biomass estimation.

Bibliography and Sitography

[1] International Telecommunication Union, “ITU Radio Regulations,” vol. 1, 2016.

[2] International Telecommunication Union, “Feasibility of sharing between active spaceborne sensors and other services in the range 420-470 MHz,” in *RECOMMENDATION ITU-R SA.1260-1*, 2003.

[3] K. Hibbard, W. Steffen, S. Benedict, T. Busalachi, P. Canadell, R. Dickinson and M. Raupach, *International Geosphere Biosphere Programme: "The Carbon Challenge",* Stockholm, 2001.

[4] International Union for Conservation of Nature, *Forests and climate change,* Gland, 2021.

[5] A. Dean, *Deforestation and climate change,* Climate Council of Australia, 2019.

[6] ESA Earth Observation Portal, “Biomass (Biomass monitoring mission for Carbon Assessment),” [Online]. Available: https://directory.eoportal.org/web/eoportal/satellite-missions/b/biomass. [Accessed 2021 October 9].

[7] European Space Agency, “Report for Mission Selection: Biomass (SP-1324/1),” 2012.

[8] R. F. Rincon, T. Fatoyinbo, B. Osmanoglu, S. Lee, K. J. Ranson, G. Sun, M. Perrine and C. Du Toit , *ECOSAR: P-Band Digital Beamforming Polarimetric and Single Pass Interferometric SAR,* Greenbelt: NASA/Goddard Space Flight Center, 2014.

[9] R. Rincon, L. Carter and D. Lu, *Next Generation P-Band Planetary Synthetic Aperture RADAR,* University of Arizona: NASA Goddard Flight Center, 2021.

[10] NASA Goddard Flight Center and University of Arizona, “Space Exploration Synthetic Aperture RADAR (SESAR),” in *52nd Lunar and Planetary Science Conference (LPI Contrib. No. 2548)*, 2021.

[11] ICEYE, “ICEYE SAR Constellation Capabilities,” [Online]. Available: https://www.iceye.com/sar-data/constellation-capabilities. [Accessed 12 October 2021].

[12] ESA Earth Observation Portal, “ICEYE Constellation of SAR X-band microsatellites,” [Online]. Available: https://directory.eoportal.org/web/eoportal/satellite-missions/i/iceye-constellation. [Accessed 12 October 2021].

[13] PredaSAR, “PredaSAR a Terran Orbital Corporation,” [Online]. Available: predasar.com. [Accessed 13 October 2021].

[14] Everything RF, “World’s Largest Constellation of 48 SAR Satellites for Government and Commercial Applications,” 23 June 2020. [Online]. Available:

https://www.everythingrf.com/News/details/10396-World-s-Largest-Constellation-of-48-SAR-Satellites-for-Government-and-Commercial-Applications. [Accessed 13 October 2021].

[15] BBC News, "Elon Musk sets out Starlink goals," June 29 2021. [Online]. Available: https://www.bbc.com/news/technology-57641676. [Accessed October 14 2021].

[16] NASA EarthData, "What is Synthetic Aperture Radar?," 10 March 2021. [Online]. Available: https://earthdata.nasa.gov/learn/backgrounders/what-is-sar. [Accessed 16 October 2021].

[17] B. Zhou, X. Qi and H. Zhang, *An Accurate GEO SAR Range Model for Ultralong Integration Time Based on mth-Order Taylor Expansion,* Basel: MDPI, 2021.

[18] T. Ager, The Essentials of SAR, 2021.

[19] M. Villano, G. Krieger and A. Moreira, *Waveform-Encoded SAR: A Novel Concept for Nadir Echo and Range Ambiguity Suppression,* German Aerospace Center (DLR), 2017.

[20] K.-S. Chen, Principles of Synthetic Aperture Radar Imaging, CRC Press, 2015.

[21] J. M. Blackledge, Digital Image Processing: Mathematical and Computational Methods, Woodhead Publishing, 2006.

[22] Ru-Shan Wu and M. Nafi Töksoz, "Diffraction tomography and multisource holography applied to seismic imaging," *Geophysicists,* vol. 52, no. 1, pp. 11-25, January 1987.

[23] S. Tebaldini and F. Rocca, "Multistatic Wavenumber Tessellation: ideas for high resolution P-Band SAR missions," in *IEEE International Geoscience and Remote Sensing Symposium (IGARSS)*, 2017.

[24] L.M.H. Ulander, A. Barmettler, B. Flood, P.-O. Frölind, A. Gustavsson, T. Jonsson, E. Meier, J. Rasmusson, G. Stenström, "Signal-to-clutter ratio enhancement in bistatic very high frequency (VHF)-band SAR images of truck vehicles in forested and urban terrain," *IET Radar, Sonar & Navigation,* vol. 4, no. 3, p. 438– 448, June 2010.

[25] L. M. H. Ulander, P. Frölind, A. Gustavsson and G. Stenström, "Bistatic P-band SAR signatures of forests and vehicles," in *2012 IEEE International Geoscience and Remote Sensing Symposium*, 2012.

[26] R. Shah, X. Xu, B. Stiles, X. Xavier Bosch-Lluis and S. Yueh, "A Satellite Synthetic Aperture Radar Concept Using P-Band Signals of Opportunity," *IEEE JOURNAL OF SELECTED TOPICS IN APPLIED EARTH OBSERVATIONS AND REMOTE SENSING,* vol. 14, 2021.

[27] A. D. a. Space, "Successful deployment of giant reflector for forest monitoring satellite Biomass," 21 October 2021. [Online]. Available: https://www.airbus.com/newsroom/press-releases/en/2021/10/successful-

deployment-of-giant-reflector-for-forest-monitoring-satellite-biomass.html. [Accessed 30 October 2021].

[28] R. F. Rincon, T. Fatoyinbo, B. Osmanoglu, S. Lee, C. F. du Toit, M.Perrine, K. J. Ranson, G. Sun, M. Deshpande and J.Beck, D. Lu, and T.Bollian, "Digital Beamforming Synthetic Aperture Radar Developments at NASA/Goddard Space Flight Center," in *IEEE International Symposium on Phased Array Systems and Technology*, Waltham, 2016.

[29] C. F. du Toit, M. Deshpande, and R.F. Rincon, "Advanced Antenna Design For Nasa's EcoSAR Instrument," in *IEEE International Symposium on Phased Array Systems and Technology*, Waltham, 2016.

[30] H. Riebeek, "NASA Earth Observatory: Catalog of Earth Satellite Orbits," 4 September 2009. [Online]. Available: https://earthobservatory.nasa.gov/features/OrbitsCatalog. [Accessed 30 October 2021].

[31] G. Krieger, "MIMO-SAR: Opportunities and Pitfalls," *IEEE Transactions on Geoscience and Remote Sensing,,* vol. 52, no. 5, p. 2628–2645, 2013.

[32] L. Flora, *MSc thesis: A Multi-Static Spaceborne SAR Formation for High-Resolution Imaging at Longer Wavelengths,* Milano, 2020.

[33] A. Freeman and S. L. Durden, "A three component scattering model for polarimetric SAR data," *IEEE Transactions on Geoscience and Remote Sensing,* vol. 36, no. 3, pp. 963-973, May 1998.

[34] H. D. Curtis, Orbital Mechanics for Engineering Students, Florida: Butterworth-Heinemann, 2020.

[35] Jet Propulsion Laboratory, "Astrodynamic Parameters," 2021. [Online]. Available: https://ssd.jpl.nasa.gov/astro_par.html. [Accessed 1 November 2021].

[36] European Space Agency, "SAR (ERS) Overview," 2021. [Online]. Available: https://earth.esa.int/eogateway/instruments/sar-ers/description. [Accessed 1 November 2021].

[37] NASA, "Solar System Exploration," [Online]. Available: https://solarsystem.nasa.gov/planets/earth/by-the-numbers/. [Accessed 1 November 2021].

[38] J. Mohr and S. Madsen, "The impact of curved satellite tracks on SAR focusing," *IGARSS 2000. IEEE 2000 International Geoscience and Remote Sensing Symposium. Taking the Pulse of the Planet: The Role of Remote Sensing in Managing the Environment. Proceedings (Cat. No.00CH37120),* vol. 1, pp. 87-79, 2000.